Abstract

This study focuses on investigating oxyfuel combustion with the addition of water using reactor models and the impact of vapor addition on diffusion flames and to simulate entropy generation in the combustion process. The reactor models are capable of representing premixed counterflow as well as free flame configurations in the study.

The governing equations used in the simulations include mass, momentum, species transport, and energy conservation equations. Additionally, custom governing equations are employed to account for water injection into the system by adding a source term for the vaporization of water. The concentration of water in the diffusion model of the oxidizer is varied in steps of 0.025 molar fraction to observe its influence on the combustion process.

Diffusion flames are studied to analyze the combustion characteristics under different water addition scenarios. The simulations provide insights into the flame structure, temperature profiles, species concentrations, and overall combustion performance. The effects of water addition on entropy generation are also investigated, allowing for a comprehensive analysis of the thermodynamic behavior of the system.

The results contribute to a better understanding of oxyfuel combustion with water addition and its impact on diffusion flames. The findings provide valuable insights into the role of water in influencing combustion characteristics, such as flame structure and temperature distribution. The assessment of entropy generation offers important information on the overall efficiency and performance of the combustion process.

This study provides a comprehensive analysis of oxyfuel combustion by combining reactor models, custom governing equations, and stepwise addition of water to the oxidizer. The results can guide the development of advanced combustion systems with improved efficiency and reduced environmental impact by optimizing water use as an additive.

Sammendrag

Denne studien fokuserer på undersøkelse av oksyfuelforbrenning med tilsetning av vann ved bruk av reaktormodeller og påvirkningen av damptilsetning på diffusjonsflammer og for å simulere generering av entropi i forbrenningsprosessen. Reaktormodellene er i stand til å representere forhåndsblandet motstrøm samt fri flammekonfigurasjoner i studien.

De styrende ligningene som brukes i simuleringene inkluderer ligninger for masse, momentum, artstransport og energisparing. I tillegg brukes tilpassede styrende ligninger for å redegjøre for injeksjon av vann i systemet ved å legge til en kildeterm for fordamping av vann. Konsentrasjonen av vann i diffusjonsmodellen til oksidasjonsmidlet varieres i trinn på 0,025 molar fraksjon for å observere dens innflytelse på forbrenningsprosessen.

Diffusjonsflammer studeres for å analysere forbrenningsegenskapene under forskjellige vanntilsetningsscenarier. Simuleringene gir innsikt i flammestrukturen, temperaturprofiler, artskonsentrasjoner og generell forbrenningsytelse. Effektene av vanntilsetning på generering av entropi blir også undersøkt, noe som muliggjør en omfattende analyse av den termodynamiske oppførselen til systemet.

Resultatene bidrar til en bedre forståelse av oxyfuel-forbrenning med vanntilsetning og dens innvirkning på diffusjonsflammer. Funnene gir verdifull innsikt i vanns rolle i å påvirke forbrenningsegenskaper, som flammestruktur og temperaturfordeling. Vurderingen av generering av entropi gir viktig informasjon om den generelle effektiviteten og ytelsen til forbrenningsprosessen.

Ved å kombinere reaktormodeller, tilpassede styrende ligninger og trinnvis tilsetning av vann til oksidasjonsmidlet, gir denne studien en omfattende analyse av oksyfuelforbrenning. Resultatene kan lede utviklingen av avanserte forbrenningssystemer med forbedret effektivitet og redusert miljøbelastning ved å optimalisere bruken av vann som tilsetningsstoff

Nomenclature

$\dot{m}$	Mass flux $\left[\frac{kgm^2}{s}\right]$
$\dot{\omega}$	Molar production rate $\left[\frac{mol}{m^3 s}\right]$
Λ	Pressure eigenvalue $\left[\frac{kg}{m^3 s}\right]$
λ	Thermal conductivity $\left[\frac{W}{mK}\right]$
μ	Dynamic viscosity $\left[\frac{kg}{ms}\right]$
ρ	Density $\left[\frac{kg}{m^3}\right]$
B	Coefficient in radiation model $\left[\frac{W}{m^2}\right]$
c_p	Specific heat capacity $\left[\frac{J}{kgK}\right]$
D	Multicomponent diffusion coefficient $\left[\frac{m^2}{s}\right]$
D^T	Soret diffusion coefficient $\left[\frac{m^2}{s}\right]$
h	Enthalpy $\left[\frac{J}{kg}\right]$
i	Reaction
j	Diffusive mass flux $\left[\frac{J}{kgm^2}\right]$
k	Species
k_f	Forward rate constant $\left[\frac{kmol}{m^3 s}\right]$
k_p	Planck mean absorption coefficient $[m^{-1}]$
L	Length of seperation $[m]$
N_R	Number of reactions
N_S	Number of species
q	Value of interest
r	Radial position $[m]$
S_L	Laminar flame speed
T	Temperature $[K]$
u	Axial velocity $\left[\frac{m}{s^2}\right]$
V	Scaled radial velocity $[s^{-1}]$

v	Radial velocity $\left[\frac{m}{s^2}\right]$
W	Molecular weight $\left[\frac{kg}{mol}\right]$
X	Molar fraction
Y	Mass fraction

Table of Contents

1 Introduction

1.1 Motivation and Background

Globally, reducing reliance on fossil fuels is becoming increasingly imperative. Climate change has been identified as the foremost concern for the future of humanity [1]. Fossil fuel accounts for the world's primary energy source, of which over 80% of energy comes from [2] [3] [4] [5]. Referred to as a red code situation on our beloved planet [6], reducing fossil fuel usage by optimizing renewable energy sources will be of essential importance.

Combustion uses fuel to produce energy in heat and power generation, and chemical reactions are crucial to understanding energy conversion. With innovative technology and increased capabilities of computers, computational fluid dynamics (CFD) has become an essential and handy tool to model chemical reactions. Computational Fluid Dynamics (CFD) is the ultimate design tool for designing and optimizing combustion processes providing detailed knowledge of temperature, concentrations, diffusion, heat, and mass fluxes, etc. that enable entropy generation and exergy destruction to be modeled in combustion devices, which is of great importance to understanding efficient energy use. However, cost-effective sub-models must be developed, implemented, and used optimally. Moreover, the CFD simulations must be carried out for transient conditions to study the effect of changing operating conditions and minimize these impacts through improved plant operation and operational guidelines [7].

The analysis of entropy generation and exergy loss based on the second law is a measure to optimize the performance of energy conversion systems [8]. Accordingly, studying entropy generation in laminar flames can give insight into energy conversion. Additionally, the strive for less-polluting devices has drawn more and more attention to synthetic gases [9]. Synthetic gas, or syngas, an explosive mixture containing varying amounts of H_2 and CO, is expected to play a significant role in future renewable and environmentally friendly energy demand. On the other hand, applying syngas introduces a large amount of CO, and incomplete combustion generates CO, leading to pollution.

1.2 Previous Work

The study of flames is reported in various problems involving diverse fuels, configurations, and conditions. Investigations and analyses have been conducted, exploring multiple scenarios. The conditions governing flame behavior are defined by many parameters, each varying in its degree of importance and impact on simulations. One crucial decision significantly influences simulations is whether to include or neglect turbulence. In the present project, the focus is explicit on the laminar behavior of flames. Accordingly, turbulent behavior is not directly applicable to the current study, it has provided valuable knowledge regarding the complex dynamics and transport processes involved in combustion, following that the simulation of turbulent flames consists of considering other transport processes, the addition of source terms, etc., [10] [11] [12] [13] [14]. This choice allows a deeper exploration of previous works primarily examining laminar flame configurations. Whether the

flame is characterized as premixed or non-premixed impacts the behavior, and it is essential to choose appropriate models based on the system considered. Variations in inlet conditions can significantly affect the flame structure, stability, and propagation. Among all these parameters, selecting an appropriate chemical mechanism to simulate the flame is of utmost significance. A chemical mechanism encompasses the reactions and species involved in the combustion process, providing reaction rates and kinetic data. Choosing a suitable chemical mechanism determines the accuracy and reliability of the flame simulations. It is crucial to consider mechanisms that have been extensively validated and optimized for the specific fuel and combustion conditions of interest.

This section presents an overview of previous works that have explored flame configurations, entropy generation and chemical kinetics. By examining the insights gained from these studies, we can identify the key findings, challenges, and gaps in knowledge, which will guide the research direction in this project.

1.2.1 Laminar Flames

Laminar flames have been highly investigated, both premixed and non-premixed, most reported by Salimanth and Ertesvåg [15]. In premixed flames, datta investigated confined jet flames [16] and confined jet flames with gravity [17]. Stanciu et al. [18] studied the same flame with methane in a global, one-step mechanism. Nishida et al. [19] reviewed both laminar premixed and non-premixed flames, with fuel as methane and hydrogen. All agreed that the entropy generation contribution due to conductive heat transfer was the largest, followed by chemical reactions and mass diffusion.

Chen et al. [20] agreed with the above, while studies of the non-premixed flame Chen et al. [21] showed chemical reactions more significant than heat conduction. Raghavan et al. [22], and Pope et al. [23] studied flame around a fuel droplet and found heat conduction to be the most significant contribution to entropy generation, followed by contribution due to chemical reactions and mass diffusion. All reported studies agreed that the contribution due to viscous forces was negligible. Zhang et al. [24] and Yan et al. [25] investigated entropy generation in sooting diffusion flames. Reducing chemical mechanisms, [26][27][28] are commonly seen in studies related to soot formation [29]. Studies showed that soot significantly affected entropy generation, particularly on contribution due to chemical reactions and mass diffusion.

Studies investigating diluted combustion processes report thermal, transport, chemical, and radiative effects [30] [31] [32] to be mainly affected. Yoo et al. [33] investigated the ignition and extinction of hydrogen and methane with varying water concentrations [34]. The studies revealed that H_2O promotes extinction and reduces the ignition range. These effects are primarily attributed to three-body reactions involving water vapor. Kuo-Hsing Yang et al. [35] analyzed NO formation in counterflow diffusion flames by varying the strain rate and diluent. The study demonstrated that adding H_2O reduces NO levels at high and low stretch rates. Reported by Giles et al. [36] in an air environment, showed that introducing diluent H_2O and CO_2 rather than N_2 are more effective in reducing pollution. Som et

al. [37] conducted experiments and numerical simulations to investigate the combustion of counterflow syngas with air under various conditions. These conditions included pressures, strain rates, CO/H2 ratios, and equivalence ratios of 6, 14, and 16 for partially premixed flames, which Wang et al. [38] simulated. Further, he investigated the addition of H_2O in oxyfuel utilizing an artificial H_2O component in a numerical model to separately investigate the effects of H_2O on CO production at the flame front.

1.2.2 Chemical Mechanism

Chemical mechanisms are an essential part of combustion modeling. Providing reactions and species involved in combustion processes and each species' reaction rates. Gri-Mech 3.0 is a widely used chemical mechanism for modeling methane combustion due to its comprehensive and detailed nature. It includes 325 reactions and 53 different species and has been optimized for modeling natural gas flames and ignition. Since Gri-Mech 3.0 is suitable for natural gas combustion, it is also assumed to be an appropriate mechanism for syngas combustion, as syngas can be reproduced from natural gas.

The CO/H_2 combustion mechanism is a fundamental aspect of hydrocarbon fuel combustion and has been the subject of extensive research [39, 40, 41, 42, 43, 44]. These studies are widely used for simulating the kinetics of CO/H_2 combustion. The Davis mechanism, proposed by Davis et al. [40], based on the Gri-Mech 3.0 mechanism [45], a detailed mechanism with 53 species and 325 reactions. The proposed mechanism was reduced to 14 species and 38 elementary reactions. Wang et al. [41] further optimized this mechanism and proposed the USCII mechanism, which utilized reaction rates for $CO + OH = CO_2 + H$ and $CO + HO_2 = CO_2 + OH$ as reported by Joshi et al.[46] and You et al. [47]. Li et al. [48], inspired by Mueller's H_2 oxidation mechanism [49], proposed the Li mechanism, a combustion mechanism of H_2/O_2.

Although these mechanisms have been successful in simulating syngas combustion, mainly in air atmosphere, the mechanisms fail to account for the impact of high concentration of H2O on the elementary reaction. Michael et al. [50] reported the importance of the kinetics of $H_2O + M = H + OH + M$, which Burke et al. [51] optimized to the kinetic data for the Li mechanism to account for. The Burke mechanism was extensively validated against a large body of experimental data. At high concentrations of H_2O, the high third-body efficiency of H_2O results in a tenfold increase in the rate of three-body reactions compared to an N_2 atmosphere [50, 55]. To make the addition of water more accurate, the kinetic data about the crucial three-body reactions ($M = H_2O$) must be adjusted to achieve highly accurate calculations. Sun et al. [39] proposed a modified mechanism based on this that showed promising results compared to other chemical mechanisms and experimental values.

1.3 Optimizing Entropy Generation Analysis with Water Addition in Combustion Processes

The presented studies have shown several flames and cases studied in detail, however, extensive research still awaits. By investigating the influence of H_2O addition on combustion processes, this study aims to contribute to the studies conducted and optimization of renewable energy utilization. The findings from this research will aid in developing more sustainable energy conversion systems and pave the way for a greener and more environmentally conscious future.

1.3.1 Objectives and Scope

Simulating non-ideal gases is a complex area. A second objective of the study is to establish a model incorporating the effects of water made on the assumptions of using initial values corresponding to liquid water at boiling temperature and utilizing a source term, the heat of vaporization, for the change of state to vapor.

Previous studies, as illustrative examples in Section 1.2.1 of prior research studies that have examined various parameters. The first objective is to continue the work of already established groundwork for understanding the effect of H_2O addition to oxy flame and study the entropy generation in oxyfuel counter diffusion flame with the addition of vapor H_2O. The aspects mentioned have not been extensively explored or reported in the existing literature. Given the limited extent of previous studies, it was essential to carefully select the parameters for variation to ensure a comprehensive analysis. This research goes beyond the boundaries of prior investigations, allowing for a detailed examination and in-depth understanding of the subject matter. The simulations are all simulated in intervals of adding molar H_2O in intervals of 0.025, 41 flames. This meant a detailed mechanism sometimes took one hour to solve. In addition, the flame simulations were conducted for three different fuel compositions, seven different inlet temperatures, nine different mass fluxes, and five different pressures. In addition, the simulations used to simulate the initial results are used with Gri-Mech 3.0 mechanism [45], which later was compared with the mechanism proposed by Sun et al. [39]. In addition, the fuel composition corresponding to equimolar CO/H_2 is compared with Davis mechanism [40], the USC II Mechanism [41] and Li mechanism [43],.

To assess entropy generation, the contributions from four irreversible processes: heat conduction, mass diffusion, viscous forces, and chemical reactions, mainly. Radiation was enabled in the cases that compared the mechanisms. Additionally, the Soret flux will be accounted for using a multicomponent formulation for the transport model. The custom ode implements a heat of vaporization source term in addition. Simulating premixed flames is not initially a scope of the study, respectively based on using already implemented flame models provided by Cantera [84]. Still, flame behavior between premixed flames and the implemented model is compared. Regarding other considerations, the analysis excludes variations in inlet pressure, which remains constant in the axial and radial directions. As a result, mass diffusion due to pressure differences is not considered. Various parameters, such as the addition of liquid parameters, allows for the examination of the transient responses and the influence of the added source term and performance. Including

actual liquid water in the combustion system introduces additional complexities, such as vaporization, heat transfer, and chemical interactions. These phenomena can be effectively analyzed by employing transient behavior, offering flame behavior of a premixed flame.

1.3.2 Research Questions

To provide a clear understanding of the research focus in the current project, the following research questions have been formulated:

1. How does adding molar H_2O in intervals of 0.025 impact the flame simulations? And how do fuel compositions, inlet temperatures, varying mass fluxes, and changing the pressure affect entropy generation?

2. How do different chemical mechanisms influence the result of entropy generation in the simulations? And can the optimized mechanism show any relevance to the transient flame?

3. How well can transient behavior analysis effectively capture the addition of water in flames? How does the addition of liquid parameters impact the transient responses and behavior of the combustion system?

Research on the addition of water to oxyfuel flames is relatively limited, underscoring the importance of comparing chemical mechanisms to gain valuable insights into flame behavior. Additionally, this study aims to investigate the utilization of liquid water, considering the heat of vaporization as an auxiliary source to account for the phase transition from liquid to vapor. It is worth noting that there is a shortage of conducted entropy generation analysis explicitly focusing on adding vapor water in counterflow diffusion flames to the extent explored in this study. Therefore, the research objectives are established to address this gap and provide a comprehensive understanding of entropy generation analysis by adding vapor water. The fundamental principles of thermodynamics, combustion, ideal gases, and more are essential for studying the process, as elaborated in Section 2.

2 Theory

2.1 Fundamental Thermodynamics

Thermodynamics allows analyzing and quantifying the energy transformations occurring within combustion systems. It provides valuable insights into combustion processes' efficiency, performance, and environmental impact. By delving into the foundational concepts of thermodynamics, we can gain a solid foundation for further exploration of combustion systems. Combustion systems are pivotal in various industries, such as power generation, transportation, and chemical processes. To comprehensively understand these systems, exploring several fundamental thermodynamic concepts is imperative. This section presents an overview of thermodynamic principles essential for studying combustion and reactive systems. According to Turns [78], in Chapter 2 of his book, the principles of thermodynamics are discussed in detail. Additionally, in Chapter 5 a comprehensive analysis of combustion processes.

2.1.1 Ideal Gas Mixture

In general, a fluid can exist in either a liquid or a gas state, with a notable distinction lying in the equation of state, which establishes a connection between pressure p, temperature T, and mass density ρ. The equation of state of an ideal gas can be expressed for a multicomponent mixture as

$$p = \frac{\rho R_u T}{\overline{W}}, \tag{1}$$

where R_u is the universal gas constant and $\overline{W}$ is the mixture molecular weight. Respectively, the composition of a mixture can be characterized by the species mole fractions and mass fractions. The mole fraction of a species k, denoted as X_k, is defined as

$$X_k = \frac{N_k}{N_{total}}, \tag{2}$$

and similarly, the mass fraction of a species k, denoted as Y_k, is defined as

$$Y_k = \frac{m_k}{m_{total}}. \tag{3}$$

In Eq. (2), N signifies the number of moles in a multicomponent mixture, while m signifies the amount of mass in Eq. (3).

Knowledge of species fraction can further be incorporated into Eq. (1), by translating the mixture molecular weight to be defined as a weighted sum of mole fraction

$$\overline{W} = \sum_k X_k W_k, \tag{4}$$

or mass fraction

$$\overline{W} = \frac{1}{\sum_k (Y_k / W_k}). \tag{5}$$

Respectively, W_k is the molecular weight of the individual species k. The fraction of species qualifies computing of several various weighted mixture properties [78].

2.1.2 Heat of Vaporization

The objective of this section is to provide a brief explanation of the heat of vaporization, also known as the enthalpy of vaporization or heat of evaporation. An essential application to thermodynamics is a thermodynamic property that represents the total heat content of a system. It combines the system's internal energy with the pressure-volume work done by or on the system. Enthalpy is denoted by the symbol "H" and for an ideal gas mixture, the specific enthalpy h property is expressed as a weighted sum of the species mass fraction, as seen in Eq. (6)

$$h = \sum_i Y_i h_i \tag{6}$$

Turns [78] define the transition from a liquid to a vapor phase holds immense importance in combustion processes, particularly in scenarios like the vaporization of a liquid fuel droplet before combustion. The heat of vaporization signifies the amount of heat needed at constant pressure to completely convert a unit mass of liquid into vapor at a specific temperature, and can be expressed as

$$h_{fg}(T.P) = h_{vapor}(T, P) - h_{liquid}(T, P), \tag{7}$$

where h_{fg} is the enthalpy of vaporization, and T and P represent the corresponding saturation temperature and pressure. Further, given the enthalpy of vaporization is kept constant at a given saturation temperature and pressure, the Calusius-Clapeyron equation, which can be expressed as

$$\frac{dP_{sat}}{P_{sat}} = \frac{h_{fg}}{R}\frac{dT_{sat}}{T_{sat}^2}. \tag{8}$$

can be used to calculate the saturation pressure dP_{sat} in varied temperatures. Although the latent heat of vaporization, in conjunction with the Clausius-Clapeyron equation, is frequently employed to estimate the variation in saturation pressure. A key condition for using this relation refers to a negligible specific volume of the liquid phase compared to the vapor, which also behaves as an ideal gas.

2.1.3 Energy conservation

Consider a simple campfire as illustrated in Fig. 1. Wood (fuel) is burned with oxygen (oxidizer), producing heat and light. The substance of wood has been heated to its ignition temperature, defined as the minimum temperature required to start or cause combustion. In the presence of oxygen reaction's mainly produces carbon dioxide and water vapor, although additional products are produced. The heat generated by the reaction causes nearby wood to catch fire, sustaining the combustion process. However, the combustion process in a fire camp is not completely efficient. Some of the energy released during combustion is lost to the surroundings in the form of heat, and some of it is used to heat up the logs and the air around.

The first law of thermodynamics, also known as the law of energy conservation, is a fundamental principle in physics and thermodynamics. It states that energy

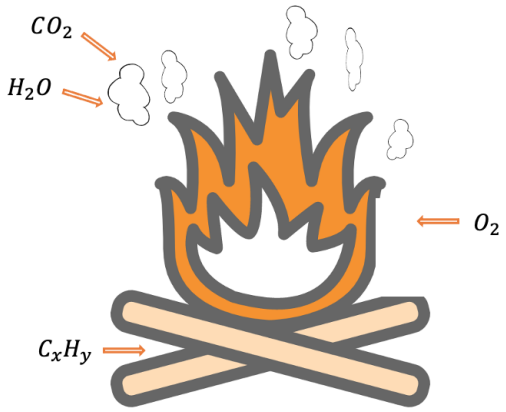

Figure 1: Simple schematic of a campfire.

cannot be created or destroyed; it can only be transferred or transformed from one form to another. Applied to the energy conservation for fixed mass systems,

$$Q - W = \Delta E_{1-2}, \tag{9}$$

it signifies that any energy added to a system in the form of heat Q increases its internal energy, and any work done by the system W decreases its internal energy. The first law establishes a connection between heat, work, and internal energy, emphasizing that energy is conserved within a closed system. The energy of the system in Eq. (9) is a state variable and is transformed to an instantaneous time rate to describe instantaneous rates of heat transfer and work expressed as

$$\dot{Q} - \dot{W} = \frac{dE}{dt} \tag{10}$$

2.2 Entropy

2.2.1 Second Law of Thermodynamics

This section aims to present entropy and provide insight into the second law of thermodynamics and the importance of application. According to Moran [76], Chapter 6, statements of the Second Law by Clausius and Kelvin-Planck. First, Chapter 5, the Clausius statement states that a system could never operate solely on energy transfer by heat from a cold to a hotter body. The Kelvin-Planck statement states that it is impossible for any system to operate in a thermodynamic cycle and deliver a net amount of energy by work to its surroundings while receiving energy by heat transfer from a single thermal reservoir. If a process violates the Clausius statement by allowing heat to flow from a colder body to a hotter body without any additional effects, it would also violate the Kelvin-Planck statement, as it would contradict the principle of converting heat into work without other energy inputs.

2.2.2 Clausius Inequality

In the preceding sections of this chapter, we have discussed the second law of thermodynamics and its corollaries in the context of cyclic systems exchanging heat with one or two thermal energy reservoirs. However, in this particular section, we introduce a corollary known as the Clausius inequality, which applies to any cycle regardless of the heat transfer source or recipient during the cycle.

The Clausius inequality, as seen in Eq. (11), is a fundamental principle that forms the basis for comprehending various concepts associated with entropy, entropy production, and entropy balance. A solid grasp of the underlying theory is essential as it facilitates a deeper understanding of the subsequent aspects explored in this study. Thus, the Clausius inequality serves as a vital foundation for the overall comprehension of the research.

$$\oint_C \left(\frac{\delta Q}{T}\right)_b \leq 0 \tag{11}$$

Here dQ represents the heat transfer and T is the absolute temperature at a particular part of the boundary b. The symbol C indicates that the integral is performed over the boundary of the system executing the cycle. The symbol r signifies that the integral is evaluated over all parts of the boundary and the entire cycle. The equality and inequality in the Clausius inequality have the same interpretation as the Kelvin-Planck statement of the second law. The equality holds when the system executing the cycle has no internal irreversibilities, indicating a reversible process. On the other hand, the inequality applies when there are internal irreversibilities present in the system. The Clausius inequality demonstrates using the Kelvin-Planck statement of the second law, as seen in Eq. (**??**).

$$\oint_C \left(\frac{\delta Q}{T}\right)_b \leq -\sigma_{cycle}. \tag{12}$$

Here, σ_{cycle} represents "strength" of the inequality, which is positive when internal irreversibilities are present, zero when no internal irreversibilities occur and can never be negative. The circular symbol on the integral sign $\oint$ emphasizes that the integral is evaluated over the entire thermodynamic cycle. It allows us to compute the sum of all heat transfers across every part of the boundary, and the total value must be less than or equal to zero. If irreversibilities exist in the system, the integral will have a negative value. Conversely, if the system consists solely of reversible processes, the integral will be zero. It is impossible for the integral to yield a positive value.

2.2.3 Entropy change

The previous sections introduced the second law of thermodynamics and Clausius inequality to understand entropy. Essentially, introduced in Section 2.1.3, energy is a term probably of some knowledge for whoever is reading this. Heard over and over again globally ambitious targets are set to accelerate the shift towards sustainable energy. Analysis of systems from a fundamental of the second law on

the other hand, is accomplished through entropy. It should be understood that entropy and energy are two completely different fundamentals of thermodynamics that shouldn't be though as relatable properties. The first law is simply an energy balance. The concept of entropy is introduced in Chapter 6 in Moran et al. [76] in conjunction with the Clausius inequality using two cycles executed by a closed system. The first cycle involves an internally reversible process A from state 1 to state 2, followed by an internally reversible process B, state 2 back to state 1. The second cycle follows a similar pattern, with an internally reversible process B from state 1 to state 2, followed by process C from state 2 back to state 1.

Applying the Clausius inequality, as seen in Eq. (12), to each cycle, and assuming the cycles are composed of internally reversible processes, the integral of dQ/T is the same for both processes A and B. It can be concluded that the integral of dQ/T has the same value for any internally reversible process connecting the two states, as seen in Eq. (13). This property is denoted as entropy and is represented by the symbol S. This integral represents the change in a property of the system and the change in entropy between the two states.

$$S_2 - S_1 = \left(\int_1^2 \frac{\delta Q}{T} \right)_{int\, rev}. \tag{13}$$

On a differential basis, as seen in Eq. (14), the equation for entropy change in internally reversible processes of closed systems. Here, dS represents an infinitesimal change in entropy, dQ is the heat transfer, and T is the temperature. The subscript "int rev" emphasizes that the integration is carried out over any internally reversible process connecting the two states.

$$dS = \left(\frac{\delta Q}{T} \right)_{int\, rev} \tag{14}$$

One well-known example of entropy in the real world is the process of ice melting. When a solid ice cube is exposed to heat, it absorbs energy from the surroundings and undergoes a phase change, transitioning into liquid water. The present study focus on water, steam and liquid, a comprehensive understanding of phase changes are essential to understand. Consider a closed system where liquid water initially sits at a temperature of 25°C, illustrated in 2.

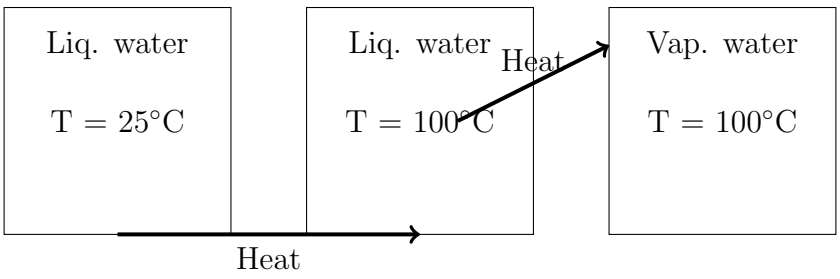

Figure 2: Application of closed system entropy balance

Liquid water is then heated and the temperature start to increase. However in a closed system, the transition from liquid to vapor (steam) occurs at a specific

temperature called the boiling point. The liquid water will essentially reach this point of 100°C (or 373.15 K) where the temperature can never go beyond. Applied to Eq. (14), the integral at which a change in state happens have equal values. Similar, if liquid water were to be heated from its boiling point of 100°C while keeping it in a closed system, the additional thermal energy supplied to the system would change the state of water, while keeping T constant. The example explicit to closed system only, a system that does not allow transfer beyond the system.

2.3 Chemical Equilibrium

The resulting combustion products are not of a simple gas mixtures, as a result of high-temperature combustion processes. In practice, achieving a completely reversible process is often not possible, as real-world systems involve various irreversibilities, such as heat losses, friction, or other forms of energy dissipation. According to Turns [78], the concept of entropy change based on reversible processes provides a useful tool for understanding the direction and magnitude of changes in a system's entropy, as one might assume based on basic stoichiometry calculations. Instead, the primary species undergo dissociation, leading to the formation of numerous minor species. The entropy product species entropies s are defined by Eq. (**??**)

$$s = s^{\circ} + R \ln\left(\frac{P}{P^{\circ}}\right) + \sum_{i=1}^{N} s_i^{\circ} \cdot Y_i \cdot T \tag{15}$$

Here, s°, s_i° and P° is the reference specific entropy, the reference specific entropy of species i and pressure. Definition of species entropies along with the specific enthalpy that may written by Eq. (6), the gibbs free energy us specified.

The Gibbs function (also known as Gibbs free energy or Gibbs energy), is a fundamental thermodynamic potential that provides information about the spontaneity and equilibrium of a chemical reaction or a physical process. It is defined as:

$$G = H - TS \tag{16}$$

where, H is the enthalpy of the system,T is the temperature of the system, and S is the entropy of the system.

The Gibbs function is particularly useful because it combines both the enthalpy and entropy contributions to determine the energy available to do useful work in a system at constant temperature and pressure.

2.4 Flames

In combustion processes, a wide range of one-dimensional reacting flows can be considered which are characterized as premixed or non-premixed flames. The flames can be further divided into laminar and turbulent flames, but in the context of studying these flames, laminar flames are often considered advantageous due to their relative simplicity and well-defined characteristics, with the reactants and

products flowing in distinct layers and making them easier to study than turbulent flames. On the other hand, turbulent flames exhibit highly chaotic and irregular flow behavior, with intense mixing of the reactants and products. Turbulent flames are more complex and challenging to analyze due to the presence of turbulence, which introduces additional transport processes and influences the flame structure, even though, significant progress has been seen in recent years in the simulation of turbulent flames. However, the focus will be purely on the fundamental principles and concepts related to laminar flame behavior.

2.4.1 Laminar Premixed Flame

Laminar premixed flames serve as a valuable starting point for studying combustion and represent an essential class of combustion phenomena extensively studied in combustion science and engineering. In premixed flames, the fuel and oxidizer are mixed before the combustion process, explained in detail in Turns, Chapter 8 [78].

One type of premixed flame is the freely-propagating premixed laminar flame. Unburned reactants, composed of the fuel and oxidizer, approach the flame front with speed defined as the laminar flame speed or the laminar burning velocity. The temperature rises within the flame, and the composition transforms from that of the reactant mixture to that of the product mixture. Illustrated in Fig. 3, the temperature and composition profiles of an CO-H_2-O_2 freely-propagating premixed laminar flame.

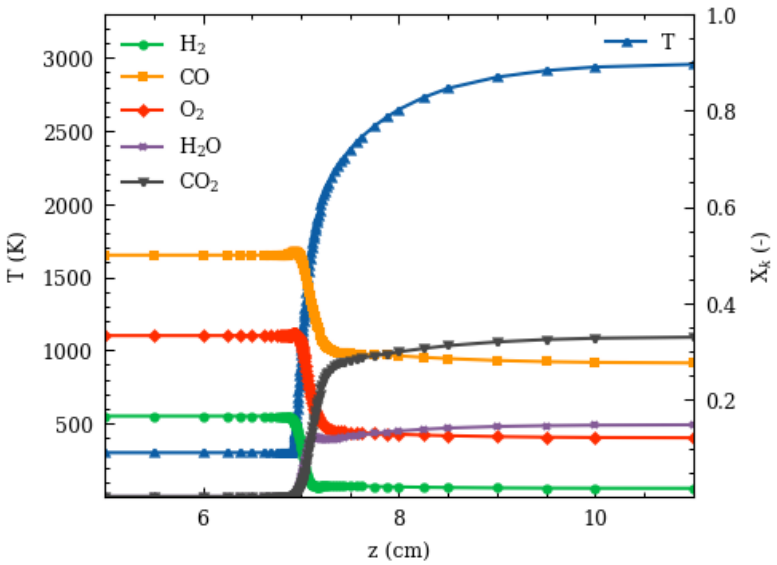

Figure 3: Temperature (T [K]) and molars fraction (X), respectively of H_2, CO, O_2, H_2O and CO_2, distributions along the flame axial position (z [cm]).

2.4.2 Counterflow Diffusion Flame

In the counterflow diffusion flame, the fuel and oxidizer streams are introduced separately, which gives rise to a non-premixed combustion process. Counterflow diffusion flame is presented in Turns, chapter 9 [78], and a schematic of the counterflow diffusion flame made from previous studies [71] is illustrated in Fig. 4. In this configuration, two opposing jets of fuel and oxidizer are aimed directly at each other, which creates a stagnation plane where all component's velocities are equal to zero, which depends on the relative magnitudes of the initial momentum fluxes of the oxidizer and fuel jets. When the momentum fluxes are similar, the stagnation plane lies at the midpoint between the two exit planes, as indicated by the dotted line in the figure. If the initial flux of one stream is increased over the other, the stagnation plane moves closer to the stream with the decreased momentum flux. A diffusion flame establishes between the fuel jet and the oxidizer jet given appropriate conditions, where the mixture is nominally stoichiometric.

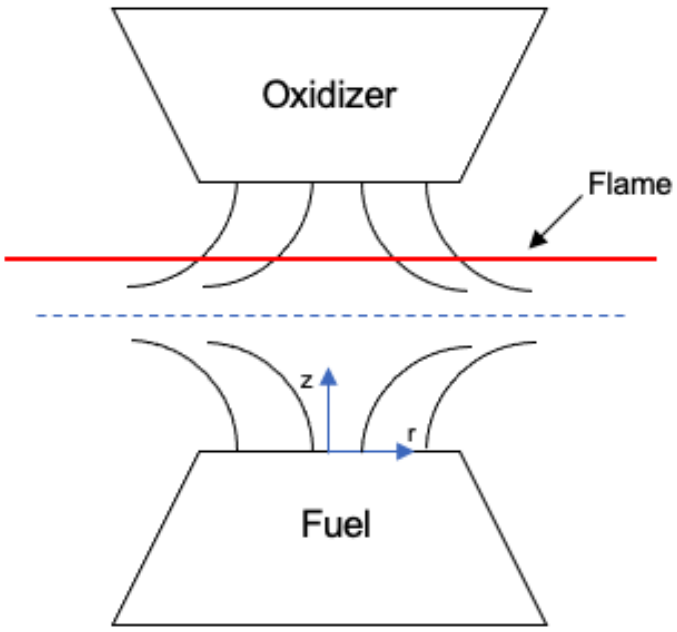

Figure 4: Laminar counterflow diffusion flame as illustrated by Turns [78], where the counterflow diffusion flame lies above the stagnation plane.

For the counterflow configuration, a strain rate is occasionally set instead of inlet mass flux rates, defined in terms of the axial strain rate along the stagnation streamline. The current notation uses the global strain rate a proposed by Williams [65] seen in Eq. 17.

$$a = \frac{2u_{\text{oxid}}}{L}\left(1 + \sqrt{\frac{u_{\text{fuel}}^2 \rho_{\text{fuel}}}{u_{\text{oxid}}^2 \rho_{\text{oxid}}}}\right) \tag{17}$$

where u_{oxid} represents the oxidizer velocity, L represents the flame length, u_{fuel} represents the fuel velocity, ρ_{fuel} and ρ_{oxid} represents the density. The velocities on the fuel side and the oxidant side are assumed to be equal. Therefore, based on the given formula, the velocity can be determined based on only setting the strain rate, an example of setting the strain rate is illustrated in Fig. 5.

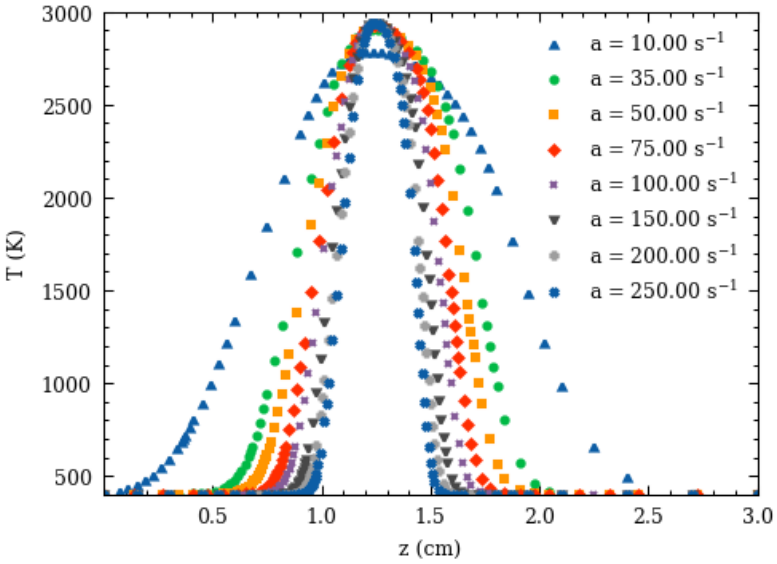

Figure 5: Changing the global strain rate in a CO-H_2-O_2 flame.

2.5 Governing Equations

The following Section, and additionally Section 2.6, Section 2.7, Section 2.8 and Section 2.10 are presented in a previous study [71]. Although, alterations were made to include radiation and heat of vaporization as additional source terms when applicable to energy, seen in Eq.(20). The governing equations are derived using a similarity solution to reduce the three-dimensional equations to a single dimension. The following model was developed by Kee et al. [80], available in his book. The equations include continuity,

$$\frac{\partial \rho u}{\partial z} + 2\rho V = 0, \tag{18}$$

radial momentum,

$$\rho u \frac{\partial V}{\partial z} + \rho V^2 = -\Lambda + \frac{\partial}{\partial z}\left(\mu \frac{\partial V}{\partial z}\right), \tag{19}$$

energy,

$$\rho c_p u \frac{\partial T}{\partial z} = \frac{\partial}{\partial z}\left(\lambda \frac{\partial T}{\partial z}\right) - \sum_{k=1}^{N_S} j_k c_{p,k} \frac{\partial T}{\partial z} - \sum_{k=1}^{N_S} h_k W_k \dot{\omega}_k, \tag{20}$$

and species transport

$$\rho u \frac{\partial Y_k}{\partial z} = -\frac{\partial j_k}{\partial z} + W_k \dot{\omega}_k. \tag{21}$$

Here, z is the axial position with u as the axial velocity. Similarly, r is the radial position, and v is the radial velocity. V is used in lieu of the radial components as the scaled radial velocity, $V = \frac{v}{r}$. Further, ρ is the mass density, μ is the dynamic viscosity of the mixture, c_p is the specific heat capacity of the mixture at constant pressure, T is the temperature in kelvin. Respectively, h_k, W_k, Y_k are the enthalpy, the molar mass, and the mass fraction of species k, and N_S is the number of species. Further on, λ is the thermal conductivity, $\dot{\omega}_k$ is the volumetric molar production rate of species k, Λ is the pressure eigenvalue and finally, j_k is the diffusive mass flux of species k in the z-direction.

The tangential velocity, w, is assumed to be zero, and the fluid is assumed to behave as an ideal gas. The pressure eigenvalue, Λ, is independent of the axial position, z, and a differential equation for this scalar is also provided to aid in the solution of the problem, $\frac{\partial \Lambda}{\partial z} = 0$. The axial momentum equation, which governs the conservation of momentum in the axial direction, can additionally be seen in Eq. (22).

$$\rho u \frac{\partial u}{\partial z} = -\frac{\partial p}{\partial z} + \frac{4}{3}\frac{\partial}{\partial z}\left[\mu \frac{\partial u}{\partial z} - \mu V\right] + 2\mu \frac{\partial V}{\partial z}. \tag{22}$$

2.5.1 Boundary Conditions

Boundary conditions play a crucial role in numerical simulations of flames. They are used to specify the values of various parameters at the boundaries of the computational domain. In this context, we can discuss the inlet and outlet boundary conditions for flames. The inlet boundary condition is specified at a point located at $z = z_0$. At this point, values are supplied for the temperature T_0, the species mass fractions $Y_{k,0}$, the scaled radial velocity V_0, and the mass flow rate $\dot{m}_0$ (except

in the case of the freely-propagating flame). The axial momentum equation is also solved at the inlet.

The following equations, respectively Eq. (23), Eq. (24) and Eq. (25), are solved at the point $z = z_0$. However, Eq. (26) is solved, only for specified inlet mass flow rates, otherwise Eq. (27) is solved.

$$T(z_0) = T_0 \tag{23}$$

$$V(z_0) = V_0 \tag{24}$$

$$\dot{m}_0 Y_{k,0} - j_k(z_0) - \rho(z_0)u(z_0)Y_k(z_0) = 0 \tag{25}$$

$$\rho(z_0)u(z_0) = \dot{m}_0, \tag{26}$$

$$\Lambda(z_0) = 0. \tag{27}$$

The outlet boundary condition is specified at a point located at $z_0 = L$. At this point, Eq. (28), Eq. (30), Eq. (29) and Eq. (31) are solved.

$$\Lambda(z_0) = 0 \tag{28}$$

$$\left.\frac{\partial T}{\partial z}\right|_{z_0} = 0 \tag{29}$$

$$\left.\frac{\partial Y_k}{\partial z}\right|_{z_0} = 0 \tag{30}$$

$$V(z_0) = 0 \tag{31}$$

For freely propagating flames, the only difference occurs in boundary conditions. Respectively, the premixed flame is mixed prior to an inlet, thus solved at the inlet boundar.

2.6 Chemical Kinetics

Turns et al., Chapter 4 [78], provides an introduction to the fundamental principles of chemical kinetics, which is the study of the rates of chemical reactions, particularly how fast a reaction proceeds and what factors affect its rate. In combustion, chemical kinetics is important because the rate of combustion is controlled by the chemical reaction rate. The net production rate of a species in a combustion reaction mechanism, which is the rate at which a particular species is being produced or consumed, can be calculated using the stoichiometry of the reactions involved.

The molar net production rate of species k in a multistep mechanism is expressed as

$$\dot{\omega}_k = \sum_{i=1}^{N_R} \upsilon_{ki} q_i. \tag{32}$$

Here N_R is the number of reactions, $\upsilon_{ki} = \upsilon''_{ki} - \upsilon'_{ki}$ are the stoichiometric coefficients of reaction i, which relate the changes in the numbers of moles of each species k in the reaction. The rate-of-progress variable, q_i, is the difference between

the forward and backward reaction rates of reaction i, expressed as

$$q_i = k_{fi} \prod_{k=1}^{N_S} \left(\frac{\rho Y_k}{W_k} \right)^{\upsilon'_{ki}} - k_{ri} \prod_{k=1}^{N_S} \left(\frac{\rho Y_k}{W_k} \right)^{\upsilon''_{ki}}. \tag{33}$$

Here N_S is the number of species, W_k is the molar mass of species k and Y_k is its mass fraction. Furthermore, the forward rate coefficient, k_{fi}, is a measure of how fast the forward reaction proceeds, expressed as

$$k_{fi} = A_i T^{\beta_i} exp \left(\frac{-E_i}{R_u T} \right), \tag{34}$$

while, the reverse rate coefficient, k_{ri}, is a measure of how fast the backward reaction proceeds, expressed as

$$k_{ri} = \frac{k_{fi}}{K_{ci}}. \tag{35}$$

Here, A_i, β_i and E_i are parameters that depend on the specific reaction mechanism in the forward rate coefficient Eq. (34). The reverse rate coefficient Eq. (35) is related to the forward rate coefficient by the equilibrium constant, K_{ci}.

2.7 Diffusive Mass Flux

Diffusive mass flux is the transport of mass due to a concentration gradient in a fluid. This phenomenon is essential in many areas of science and engineering, including chemical reaction engineering, materials science, and environmental science used to model and predict the behavior of many systems. For example, in chemical reaction engineering, the diffusive mass flux can affect the rate of reaction and the distribution of reactants and products in a system. In materials science, the diffusive mass flux can affect the rate of diffusion and the distribution of atoms or molecules in a material. In environmental science, the diffusive mass flux can affect the transport and fate of pollutants in the environment [79].

The rate of diffusive mass flux is governed by Fick's law, which states that the flux is proportional to the concentration gradient and the diffusion coefficient of the species in the fluid [81]. Fick's law can be expressed mathematically as

$$J = -D \nabla C, \tag{36}$$

where J is the diffusive mass flux, D is the diffusion coefficient of the species, and ∇C is the concentration gradient of the species in the fluid. The negative sign in the equation indicates that the mass flux is in the direction of decreasing concentration [79].

As defined in Chapter 3.5.2 in Kee et al. [80], fluids that experience chemical-composition variations have a tendency for chemical species to be transported by molecular diffusion from regions of higher concentration to regions of lower concentration. The diffusive mass flux of species k in the axial direction z is expressed as

$$j_k = \rho Y_k V_k. \tag{37}$$

Tied to Fick's laws of diffusion, in cases with multicomponent transport, the diffusion coefficient D_{ki}, represents a matrix of ordinary multicomponent diffusion coefficients relating species k to i.

The diffusion coefficient D_{ki} depends on the properties of the fluid and the diffusing species, including the viscosity and temperature of the fluid, the size and shape of the diffusing species, and the interaction between the diffusing species and the fluid. In some cases, the diffusion coefficient may also depend on the concentration of the diffusing species [79]. For cases with multicomponent transport, the diffusion coefficient is used to calculate the diffusion velocity, expressed as

$$V_k = \frac{1}{X_k \overline{W}} \sum_{i \neq k}^{N_S} W_i D_{ki} d_i - \frac{D_k^T}{\rho Y_k} \frac{\partial \ln T}{\partial z}. \tag{38}$$

Here, the mole fraction X_k is multiplied in the first term with the mixture molar mass $\overline{W}$, D_k^T represents the thermal diffusion coefficients, also known as the Soret coefficient and lastly d_i, represents the gradients in the concentration and pressure field as

$$d_i = \frac{\partial X_i}{\partial z} + (X_i - Y_i) \frac{\partial}{\partial z} ln(p), \tag{39}$$

which is also known as the diffusion driving force.

2.8 Viscous Forces

Viscous forces are an essential concept in fluid dynamics that relate to the resistance of a fluid to flow. Particularly relevant in the study of transport phenomena in various engineering applications, such as heat transfer, mass transfer, and chemical reactions [79].

In a fluid, viscous forces arise due to the interactions between adjacent layers of the fluid that have different velocities. The magnitude of the viscous forces is proportional to the viscosity of the fluid and the rate of deformation of the fluid. This relationship is described by the Navier-Stokes equation, which is the fundamental equation of fluid mechanics [82]. The application of Navier-Stokes equations to the analysis of laminar flame is covered in Turns, Chapter 7 [78]. The Navier-Stokes equations are used to describe the conservation of mass, momentum, and energy in a fluid, and they include the effects of viscosity and diffusion.

Turns notes that in the analysis of laminar flame, viscous forces are usually considered to be small compared to other forces, such as the pressure gradient and the buoyancy force [78]. However, in some cases, the effects of viscosity cannot be neglected. For example, in the study of soot formation in flames, the effects of viscosity on the flame structure must be taken into account [83].

Here, viscous stress is included. In the axial momentum Eq. (22), its presented as

$$\tau = \mu \left(\frac{\partial u}{\partial z} + \frac{\partial u}{\partial z} \right) - \frac{2}{3} \mu \frac{\partial u}{\partial z}, \tag{40}$$

and in the radial momentum Eq. (19), its expressed as

$$\tau = \frac{4}{3} \mu \frac{\partial u}{\partial z}. \tag{41}$$

2.9 Radiation

In one-dimensional flames, the radiative heat transfer is often modeled using the gray or non-gray gas models. The gray gas model assumes that the absorption coefficient of the gas mixture is a constant over a wide range of frequencies and is often used to model non-sooting flames [88]. On the other hand, the non-gray gas model accounts for the absorption coefficient's wavelength dependence and is typically used to model sooting flames where the presence of soot particles strongly affects the radiation transfer [89]. The radiative heat transfer in flames is typically described by the radiative transfer equation (RTE) [87]. However, the complexity in multi-dimension makes the modeling of the term a difficult task [38]. Radiative heat transfer is not essential for the study, and the radiation model proposed by Liu and Rogg [90] is used, as seen in (42).

The radiation model is commonly used to simulate radiative heat transfer in combustion systems, which is a non-gray gas model that accounts for the wavelength dependence of the absorption coefficient.

$$\frac{\partial q_{rad}}{\partial z} = 2k_p \left(2\sigma T^4 - B_w - B_e\right), \tag{42}$$

The term on the left side of Eq. (42) is implemented as an additional source term to Eq. (20), if the radiation model is enabled. Further, k_p is the Planck mean absorption coefficient, σ is the Stefan-Boltzmann coefficient and B can be expressed as, $B = \epsilon\sigma T^4$, where ϵ is the emissivity.

2.10 Entropy generation

In thermodynamic systems, entropy generation (or production) is defined as the amount of entropy created during irreversible processes. The following irreversible processes were considered in this project: viscous forces, conduction, mass diffusion, chemical reactions, thermal radiation, and heat of vaporization. The equations are presented in the same order as stated in Eqs. (43)-(46), in accordance to Salimath et al. [15].

$$\sigma_{visc} = \frac{\tau}{T}\frac{\partial u}{\partial z} \tag{43}$$

$$\sigma_{cond} = \frac{\lambda}{T^2}\left(\frac{\partial T}{\partial z}\right)^2 \tag{44}$$

$$\sigma_{diff} = \sum_{k=1}^{N_S}(-j_k)\left(\frac{1}{T}\frac{\partial h_k}{\partial z} - \frac{\partial s_k}{\partial z}\right) \tag{45}$$

$$\sigma_{chem} = -\frac{1}{T}\sum_{k=1}^{N_S} W_k g_k \dot{\omega}_k \tag{46}$$

It should be noted, that the last term in Eq. (38), the Dufour flux, was neglected in the calculations of the mass diffusion entropy generation contribution following

[15]. In addition, the last term in Eq. (38) was reformulated for ideal gases, $\partial h_k = C_{p,k}\partial T$ and $\partial s_k = \left(\frac{C_{p,k}}{T}\right)\partial T - \left(\frac{R_k}{p_k}\right)\partial p_k$, with the species gas constant $R_k = \frac{R_u}{W_k}$ and pressure $p_k = X_k p$, hence calculated as,

$$\left(\frac{1}{T}\frac{\partial h_k}{\partial z} - \frac{\partial s_k}{\partial z}\right) = \frac{R_k}{p_k}\frac{\partial p_k}{\partial z} = \frac{R_u}{W_k}\left(\frac{1}{X_k}\frac{\partial X_k}{\partial z} + \frac{1}{p}\frac{\partial p}{\partial z}\right). \tag{47}$$

The chemical entropy generation, Eq. (46), summarizes all chemical reactions. The term was reformulated to get the contribution provided from every elementary reaction as

$$\sigma_{chem,i} = -\sum_{k=1}^{N_S} \frac{g_k}{T} W_k \upsilon_{ki} q_i, \tag{48}$$

where, the specific Gibbs function can be expressed for each species as $g_k = h_k - T s_k$. The sum of the ith elementary reactions, Eq. (48), will correspond to Eq. (46), $\sigma_{chem} = \sum_{i=1}^{N_R} \sigma_{chem,i}$. Finally, the sum of all the following contributions corresponds to the total volumetric entropy generation rate,

$$\sigma = \sigma_{visc} + \sigma_{cond} + \sigma_{diff} + \sigma_{chem} \tag{49}$$

The additional source that contributed due to the heat of vaporization is intentionally left out in the following derivation of sources due to the complexity of non-premixed flames. Further details are presented in Section 2.12.

2.11 Exergy

Chapter 7 of Moran and Shapiro [76] comprehensively explains exergy. Although it is not the focus of the study, exergy shares similarities with entropy and is also defined based on the second law of thermodynamics. When considering an arbitrary system and a predefined environment, the thermomechanical exergy represents the maximum theoretical work achievable from the interactions between the system and the environment until equilibrium is reached. The exergy balance quantifies the change in exergy between two states and can be derived from the entropy and energy balance, expressed as

$$E_2 - E_1 = \int_1^2 \left(1 - \frac{T_0}{T_b}\right)\delta Q - [W - p_0(V_2 - V_1] - T_0\sigma. \tag{50}$$

Here, Q represents the heat transferred across the boundary at temperature T_b, while T_0 and p_0 denote the temperature and pressure of the environment, respectively. Furthermore, W represents the work done by or on the system, σ indicates the entropy production (entropy generation), V_1 represents the volume of the system in the initial state, and V_2 represents the volume in the final state.

In Eq. (50), the first term represents the exergy transferred to or from the system through heat, while the second term accounts for exergy transfer through work. The last term quantifies the exergy destroyed by irreversibilities, which includes σ that showcases how the entropy generation relates to exergy. In thermal systems, involving combustion, the exergy supplied to the system primarily originates from

the fuel's exergy. In the presence of a reacting system, it becomes necessary to incorporate chemical exergy, expressed as

$$\begin{aligned}\overline{e}^{ch} = &\left[\overline{h}_F + \left(a + \frac{b}{4}\right)\overline{h}_{O_2} - a\overline{h}_{CO_2} - \frac{b}{2}\overline{h}_{H_2O}\right] \\ &-T_0\left[\overline{s}_F + \left(a + \frac{b}{4}\right)\overline{s}_{O_2} - a\overline{s}_{CO_2} - \frac{b}{2}\overline{s}_{H_2O}\right] \\ &+\overline{R}ln\left[\frac{\left(X^e_{O_2}\right)^{a+\frac{b}{4}}}{\left(X^e_{O_2}\right)^{a}\left(X^e_{O_2}\right)^{\frac{b}{4}}}\right].\end{aligned} \tag{51}$$

The definition of chemical exergy defined in Chapter 13.6 of Moran and Shapiro [76] is the maximum theoretical work attainable by allowing the system to react with the environment through oxidation. In Eq. (51), a and b represent the number of moles of carbon and hydrogen in the fuel. h denotes the total specific enthalpy, and s represents the particular total entropy of the different species at temperature T_0 and pressure p_0. The universal gas constant is denoted by $\overline{R}$, and X^e signifies the molar fraction of the species in the environment.

2.12 Reactor Model

Reactor models are widely utilized in the study of combustion to simulate the behavior of flames in various combustion systems. These models offer a simplified representation that allows for incorporating additional terms not explicitly defined by the governing equations, defined in Section 2.5.1. In Section 2.12.3, these models account for the conservation of mass, momentum, and energy within the systems. By incorporating these factors, reactor models comprehensively describe the combustion process.

Chapter 6 of Turns [78] book, offers a comprehensive introduction to reactor modeling and its application in combustion studies. The book covers a broad range of topics, including the development of reactor models, the conservation equations employed in these models, and the different types of reactor models commonly used in combustion analysis. Numerous examples and exercises are included to demonstrate the practical utilization of reactor models in analyzing combustion systems. Here, the featured reactor models are available in Chapter 16 of Kee et al. [80] book, respectively the second edition. One feature that will be further detailed, however from Chapter 3 of Turns [78] book. The section is explicitly introduced here, as it introduces the fundamental of the study's use of reactor models.

2.12.1 Heat of Vaporization

Section 2.1.2 is continued in Turns [78] for a simple model of droplet burning. This is not the case in this study, although a common practice. However, mass transfer is introduced in Chapter 3 [78] and presents the boundary conditions between the liquid-vapor interface. Assuming equilibrium exists between the interface of states and the assumption of ideal gases, the partial pressure of gas must equal

the saturation pressure associated with the temperature of the liquid. The temperature may be defined, although energy balances for the liquid and gas phases are generally solved with the appropriate boundary conditions at the interface. Referring back to Section 2.2.3, and illustrated in Fig. 2. The change in state from liquid water to vapor water at an equal temperature of 373.15 (K) demonstrates a hypothetical crossing of a liquid-vapor boundary. Accordingly, as was established, this occurs at a constant temperature; the continuity of temperature and energy is conserved.

Heat is transferred from gas to liquid, Q_{gas}, and some cause the heating of liquid Q_{liquid}, while the remaining heat causes the phase change. The net heat transfer is defined in Eq. (52).

$$\dot{Q}_{gas} - \dot{Q}_{liquid} = \dot{Q} = \dot{m} h_{fg} \tag{52}$$

2.12.2 Batch Reactors

A batch reactor is a constant-volume reactor where the reaction occurs in a closed system. This should be a familiar fundamental by now; however, the molar production rates and the net heat transfer Eq. (52) are of primary concern here. The mass conservation of species in a batch reactor, characterized by a fixed amount of mass, as seen in Eq. (53). Here the mass of species k is defined from the systems volume V, the molecular mass of species k, and the molar production of chemical species k.

$$\frac{dm_k}{dt} = \dot{\omega}_k W_k V \tag{53}$$

A source term for the heat of vaporization, seen in Eq. (54) was obtained in cooperation with the supervisor, by deriving Eq. (52) and Eq. (53), as shown in Appendix **??**. Tthe heat of vaporization is defined as a system characterized by a fixed amount of mass. Respectively, as stated numerous times throughout the study, in accordance with the explicit importance of fundamental understanding, the heat of vaporization h_{fg} is constant in a closed system.

$$\dot{Q} = \dot{\omega}_k (W_k V \, h_{fg}) \tag{54}$$

The mass fraction Y_k of a species k, as defined on numerous occasions, yields a convenient representation of the species conservation equation, seen in Eq. (55). The terms $\frac{dYk}{dt}$ represents the rate of change of the mass fraction concerning time. Accordingly, no additional parameters are introduced in a closed system.

$$\frac{dY_k}{dt} = \frac{\dot{\omega}_k W_k}{\rho} \tag{55}$$

In the work by Kee et al., [80], additional details, including plug-flow reactors, are available. Although not fit for our purposes. Finally, the perfectly stirred reactor included in his book is presented.

2.12.3 Perfectly Stirred Reactors

The perfectly stirred reactor, also named continuously stirred tank reactor, is well acknowledged and recognized in the area of studying combustion. Following the objective of the study, the details of the implemented model are further presented in Section 3.3.2. This section presents the fundamental and general conditions for a perfectly stirred reactor model. A schematic is illustrated in Fig. 6, where the reactor inlet conditions are noted with $*$, and the mass flow rate has been established constant as mass is conserved. Accordingly, the inlet temperature T^* and mass fraction composition Y^* enters the reactor with mass flow rate $\dot{m}$. Once the gases reach inside, the gases are assumed to mix perfectly instantly. The effect which temperature and composition are perfectly uniform.

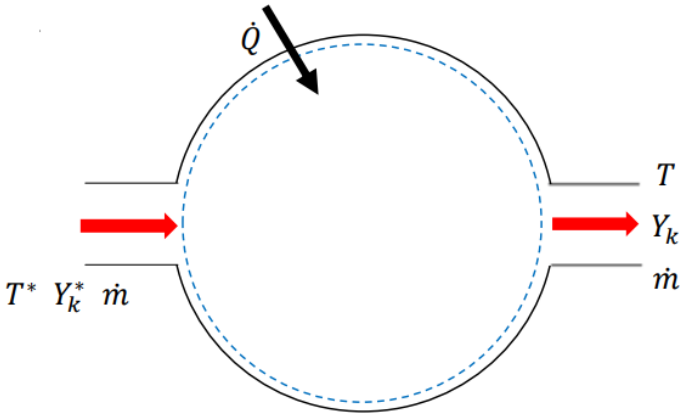

Figure 6: Schematic illustration of a perfectly stirred reactor.

Inside the reactor, chemical reactions occur within a homogeneous environment, where temperature, composition, and residence time determine the extent of the response. In steady flow conditions, the mass flow rate of reacted gases entering and exiting the reactor remains constant. The reactor's exit states T, Y_k, and the mass flow rate is assumed to be equivalent to the internal state. Further, the governing equations are defined as shown in Eq. (56) for species conservation and and shown in Eq. (57) energy conservation. Additional background, definitions, and details on the derived equations are shown in Appendix **??**.

$$\frac{dY_k}{dt} = \frac{\dot{m}}{\rho V}(Y_k^* - Y_k) + \frac{\dot{\omega}_k W_k}{\rho} \tag{56}$$

$$c_p \frac{dT}{dt} = \frac{m}{\rho V}\sum_{k=1}^{K} Y_k^*(h_k^* - h_k) - \sum_{k=1}^{K}\frac{h_k \dot{\omega}_k W_k}{\rho} + \frac{\dot{Q}}{\rho V} \tag{57}$$

3 Methodology

The methodology throughout the study is presented, with the goal of presenting the model in detail. Although First, the CFD program utilized and features are presented in Section 3.1. Section 3.2 addresses the chemical mechanism, and the Model setup in Section 3.3.

3.1 Cantera

Cantera [84] is an open-source software suite for simulating chemical kinetics in various applications, including combustion and flames. It provides a user-friendly interface for specifying chemical reactions, thermodynamic properties, and transport coefficients, and it uses numerical methods to solve the governing equations for chemical kinetics as established by Kee et al., [80] provided in the study.

Cantera [84] has several advantages over other software packages for chemical kinetics modeling. It is open-source and freely available, allowing users to modify and extend its capabilities to suit their needs. It also has a modular architecture, which allows users to customize the software to include their chemical reaction mechanisms and thermodynamic data as suited. Cantera [84] provides a wide range of already established models for solving zero- and one-dimensional models, accordingly reactors flames. Designed to simulate various well-defined and frequently encountered research areas. For more detailed insight, detailed documentation and several scripts are provided by Cantera [84] for various applications.

In the conducted studies Cantera [84] was used in the Python interface, which can be easily integrated with other scientific computing libraries, such as Matplotlib [85] and numpy [86], making it a powerful tool for analyzing and visualizing the results of simulations. The Python interface also allows for the easy scripting of complex simulations, making it a popular tool for researchers and engineers in various fields. The following sections present some of the relevant aspects of Cantera [84] for the conducted study.

3.1.1 Cantera Models

Cantera [84] provides models for simulating steady-state, quasi-one-dimensional reacting flows on the form [80] represented in Section 2.5.1. These models can simulate various flames, including freely-propagating premixed laminar flames, burner-stabilized premixed flames, counterflow diffusion flames, and counterflow (strained) premixed flames. Additionally, Cantera can simulate surface reactions to represent combustion on a catalytic surface or chemical vapor deposition processes. These different flame configurations are modeled using a standard set of governing equations within a one-dimensional flow domain, with variations in the boundary conditions applied to represent the differences between the models [84].

In Cantera [84], simulations can be conducted in zero-dimensional reactors or one-dimensional flames. A reactor represents a chemically reacting system as a thermodynamic control volume. Within a reactor, all state variables are uniformly distributed, which implies that all states are time-dependent. While transient changes can occur due to chemical reactions, the reactor assumes the presence of thermody-

namic equilibrium in all instances. While a reactor by itself defines the governing equations of the reactor, it is necessary to assign reactors to a reactor network to solve the governing equations, as time integration is performed in reactor networks. In other words, a reactor network must be defined to solve the governing equations, even if only a single reactor is considered. Applied to a reactor network, Cantera [84] uses its solver to integrate the stiff ODEs of reacting systems, referring to the governing equations defining the reactors. In addition to solving mass flow from one reactor into another, heat can be incorporated, or a wall in between can move. It enables simulations of various scenarios and studying different reactor models, including well-stirred, plug-flow, and batch reactors.

One-dimensional models allow for investigating important flame properties, which Cantera [84] provides models for. These properties include premixed flames that involve the combustion of a fuel and oxidizer mixture that is uniformly mixed before entering the reaction zone. In the diffusion flame, in contrast, the fuel and oxidizer mix and react under conditions where their velocities are substantially different and given initial values at two opposite sides are set. Both flame models are initiated by defining the necessary parameters provided with a solution of the desired chemical mechanism. For premixed, temperature, gas composition, and pressure are specified for the solution. While for models including counterflow flames, the initial temperature and pressure are determined for the solution without setting any composition. A flame object is created, and inlet conditions for the two opposite jets are set, including temperature, composition, and mass flow rates. Width is set to represent the physical extent of the space within.

In addition to the fundamental features, additional customization options are of particular interest for premixed and counterflow flames. The ability to adjust boundary emissivities refers to the efficiency with which a surface emits thermal radiation. Setting appropriate refine criteria ensures that the flame structure is adequately resolved, capturing any sharp gradients or features that may be present. Transport, by default, assumes a mixture-averaged transport model; mixture mixtures are weighted averages of the individual species' properties. However, a multicomponent system is set by specifying the transport, including the soret effect, which accounts for the diffusion of species induced by thermal gradients and can significantly impact species concentrations and flame structure.

To solve the flame models, Cantera [84] utilizes its solve function, which integrates the ordinary differential equation (ODE) system governing the flame's evolution. This integration process considers the detailed chemical kinetics, transport phenomena, and energy conservation within the reactor. Furthermore, based on the specific details of the model and the user's preferences, the adjustment of a log-level parameter that controls the amount of diagnostic information printed during the simulation is set.

3.1.2 Reactions

An input file contains the chemical mechanism including properties for reactions and species. A commonly utilized file format for such input files is YAML. YAML provides a structured and human-readable format, making it convenient for spec-

ifying settings and parameters in the chemical mechanism file [**?**]. The following section present the basic reaction types and reaction types that are essential for complex combustion models.

Elementary reactions are of the basic reaction type, a homogeneous reaction, format as

$$\mathrm{A} + \mathrm{B} \rightleftharpoons \mathrm{C} + \mathrm{D}, \tag{58}$$

and is characterized by a rate coefficient independent of pressure and mass action kinetics. A forward rate constant k_f is defined using a modified Arrhenius function, expressed as

$$k_f = AT^b e^{-E_a/RT}. \tag{59}$$

Here, A represents the pre-exponential factor, T denotes the temperature, b is the temperature exponent, E_a signifies the activation energy, and R represents the gas constant. The forward reaction rate can be calculated as

$$R_f = [\mathrm{A}][\mathrm{B}]k_f. \tag{60}$$

A three-body reaction is represented in the form

$$\mathrm{A} + \mathrm{B} + \mathrm{M} \rightleftharpoons \mathrm{AB} + \mathrm{M}. \tag{61}$$

Here, M represents an unspecified collision partner responsible for dissipating excess energy to stabilize the AB molecule in the forward direction or supplying energy to break the AB bond in the reverse direction, additionally, it is possible to explicitly designate a specific colliding species, in which case Cantera [84] automatically infers the reaction type. The effectiveness of different species as collision partners can vary. A species significantly lighter than A and B may have limited capacity to transfer its kinetic energy, resulting in inefficiency as a collision partner. Conversely, a species with a transition from its ground state that closely matches a transition in the AB* activated complex can exhibit enhanced energy exchange capabilities beyond expectations. To incorporate these effects, a collision efficiency ϵ is defined for each species. This efficiency quantifies the fraction of collisions that result in successful reactions. As a result, the forward reaction rate can be expressed as

$$R_f = [\mathrm{A}][\mathrm{B}][\mathrm{M}]k_f(T), \tag{62}$$

where the collision partner is expressed as

$$[\mathrm{M}] = \sum_k \epsilon_k C_k. \tag{63}$$

C_k represent the concentration of species k and the rate coefficient k_f can absorb any constant collision efficiency, that is set default to 1 if the collision efficiency isn't specified. Furthermore, if [M] increases, the rate defined in Eq. (62) becomes independent of [M], and a falloff reaction is of the type characterized by a rate that

is first-order in [M], while applicable for independent of [M]. The Lindemann form is the simplest expression for the rate coefficient of a falloff reaction, expressed as

$$k_f(T,[\mathrm{M}]) = \frac{k_0[\mathrm{M}]}{1+\frac{k_0[\mathrm{M}]}{k_\infty}}, \tag{64}$$

which can be written as

$$k_f(T,P_r) = k_\infty \left(\frac{P_r}{1+P_r}\right). \tag{65}$$

by defining the non-dimensional reduced pressure, expressed as

$$P_r = \frac{k_0[\mathrm{M}]}{k_\infty}. \tag{66}$$

$$k_f(T,P_r) = k_\infty \left(\frac{P_r}{1+P_r}\right) F(T,P_r) \tag{67}$$

In the presented study however, the troe falloff function proposed by Gilbert et al. [70] according to Eqs. (68), (69), (70), (71), and (72). Required for solving are three component, A, T_3, and T_1.

$$\log_{10} F(T,P_r) = \frac{\log_{10} F_{cent}(T)}{1+f_1^2} \tag{68}$$

$$F_{cent}(T) = (1-A)\exp(-T/T_3) + A\exp(-T/T_1) + \exp(-T_2/T) \tag{69}$$

$$f_1 = (\log_{10} P_r + C)/(N - 0.14(\log_{10} P_r + C)) \tag{70}$$

$$C = -0.4 - 0.67\ \log_{10} F_{cent} \tag{71}$$

$$N = 0.75 - 1.27\ \log_{10} F_{cent} \tag{72}$$

3.2 Chemical Mechanism

The modified mechanism utilized in this study is primarily Gri-Mech 3.0, but was later implemented a proposed mechanism based on recent experimental and calculated data published by Sun et al. [39]. The modified mechanism consists of 14 species and 40 elementary reactions.

The H_2 sub-mechanism of the modified mechanism predominantly originates from the Burke mechanism. Specifically, the elementary reactions H_2O + M = H + OH + M and H + O_2 (+M) = HO_2 (+M) for M = H_2O were modified with separate expressions to accurately represent their behavior. The kinetic data for the reaction H_2O + H_2O = H + OH + H_2O was obtained from experimental data reported by Michael et al. [50]. Similarly, the rate parameter for the reaction H + O_2 (+H_2O) = HO_2 (+H_2O) was based on the kinetic data reported by Bates et al. [55].

The sub-mechanism for CO oxidation in the modified mechanism was adopted from the USCII mechanism [41]. The rate parameters for the reactions CO + OH

= CO_2 + H and CO + HO_2 = CO_2 + OH were obtained from theoretical studies conducted by Joshi and Wang [46], respectively. Thermodynamic and transport data were incorporated from the USCII mechanism.

In this study, the Gri-Mech 3.0 [45], Davis [40], Li [43]. This calculation allowed for an evaluation of the modified mechanism's impact on the combustion behavior of the CO/H2/O2/H2O system. By following this methodology, the modified mechanism was developed to accurately represent the kinetics of the CO/H_2 combustion in the presence of high concentrations of H_2O. The modified mechanism incorporation of H_2O as a fictitious species facilitated the examination of the chemical effects resulting from H_2O addition.

3.3 Model setup

3.3.1 Counter Diffusion Flame

To investigate the influence of water addition on the combustion process, simulations were performed for various flame compositions within an interval of 0.025, representing the molar fraction of H_2O in the syngas oxidizer. The maximum temperature was then determined for each case to assess the effects of water addition on the combustion characteristics. To initiate the counter diffusion flame, necessary parameters are defined. A solution provided with a chemical mechanism, temperature, and pressure is specified without setting any composition. Using the provided parameters, a flame object is created in Cantera [84], tailored for simulating a counter-diffusion flame. Inlet conditions for the opposite jets are set, including temperature, composition, and mass flow rates. A flame width is set to represent the physical extent of the flame within. Additional customization options are available, such as adjusting boundary emissivities, refining criteria, and enabling features like transport modeling, Soret effect, and radiation modeling. The flame model is then solved using Cantera's [84] solve function, which integrates the ordinary differential equation (ODE) system governing the flame's evolution. This enables the determination of species concentrations, temperature, and other variables within the reactor.

The temperature and mass fractions were specified at each inlet for all cases, where $z = 0$ specified the fuel inlet and $z = L$ specified the oxidizer inlet for the counterflow diffusion flame. While $z = 0$ specified the reactants (fuel + oxidizer) inlet for the freely propagating flame. Further, mass fluxes were specified at the counterflow flame inlets.

The fuels were syngas with fuel composition with molar fraction ratio X_{H_2}/X_{CO}= 0.25/0.75, 0.50/0.50 and 0.75/0.25, while the oxidizer pure oxidizer with flame simulated at intervals of $X_{H_2O} = 0.25$ addition to the oxidizer. In total 41 flames were simulated for all cases. Initially the GRI Mech 3.0 [45] mechanism, provided by Cantera [84], was used. GRI Mech 3.0 [45], a common mechanism used for modeling natural gas combustion, consists of 53 species and 325 elementary reactions. Later simulation were mostly used with the Sun et al. [39] mechanism, and also compared with Li mechanism [43], Davis mechanism [40].

Initiating the flames using a solution at the specified parameters. When solving the flame, the boundary emissivities were kept at zero, while radiation was enabled

for some cases, but the multi-component transport and Soret flux were enabled for all cases. Since it was advisable to use the multi-component transport model, Soret Flux had to be enabled. Further, the solver had an adaptive grid that determined the convergence based on the refined criteria set. The first criterion is the ratio, which determines the maximum size ratio allowed between adjacent cells, set to 2. The second criterion is the slope, which measures the maximum relative difference in value between adjacent points. The third criterion is the curve, which evaluates the maximum relative difference in slope between adjacent cells. Both set to 0.2. Lastly, the prune criterion sets a minimum threshold for either the slope or curve values. If the computed slope or curve value falls below this threshold for all components, the points will be removed from the grid, unless a neighboring point has already been marked for deletion, prune was set to 0.

The solver could provide solutions to all equations presented in Section 2.5.1. However, none of the entropy generation terms, as shown in Section 2.10, can be provided by the solver, and their own script had to be created.

3.3.2 Reactor

Cantera [84] automatically sets up the ordinary differential equation (ODE) system based on the reactor type and reaction mechanism. Systems describing the time evolution of species concentrations, temperature, and other variables inside the reactor. Using numerical integration methods provided by Cantera [84], such as the "advance" or "step" functions the ODE integrates the system over time. Although the simulated reactor represented a custom reactorOde, initial simulations solved the Eqs. (73) and (74). The residual time seen in Eq. (75) was set to solve governing equations and additional parameters. The heat of vaporization of water at a given temperature T used the Water class from the Cantera library to compute the enthalpy difference between the liquid and vapor phases of water.

$$\frac{dY}{dt} = \frac{Y_w - Y_k}{\tau_{res}} + \frac{\dot{\omega}_k W_k}{\rho} + \frac{\dot{\omega}_w W_w}{\rho} \tag{73}$$

$$\frac{dT}{dt} = \sum_{k=1} \frac{\dot{\omega}_k h_k W_k}{\rho c_p} + \frac{T_w - T_k}{\tau_{res}} - \frac{h_{fg} W_w \dot{\omega}_w}{\rho c_p} \tag{74}$$

$$\tau_{res} = \frac{\rho V}{\dot{m}} \tag{75}$$

Further, the calculated water parameter was fed into a reactorODE that represents the ordinary differential equation (ODE) system for the reactor model. It defines the ODE function that calculates the time derivatives of temperature and species mass fractions. The ODE function depends on the current temperature T, the species mass fractions Y, and other properties of the gas and water. The class also includes methods for calculating water addition and heat release rates based on temperature and gas composition.

Further simulations were conducted with out the first source term in Eq. (73) and the second source term in Eq. (74). Additionally simulations were experimented on with the mass diffusion.

Unfortunately, the results are not included in this report. Due to a lack of time, but significant time used on this problem, the results were not analyzed. However, we have obtained significant results for the counter diffusion, which have been included in this report. Apologize for any inconvenience caused in future research or reports. Additional plots and figures related to the experiments can be found in the 6.2 materials. These visuals provide further insights into the data and support the main findings discussed in this report.

3.4 Oxy-fuel

In this section, we present the conducted research and simulation methodology for investigating the water in oxy-fuel flames, with a particular focus on syngas fuel burning in pure oxygen. While experiments involving highly flammable flames are typically conducted in specialized research facilities or laboratories, simulation models can provide valuable insights and complement experimental investigations. The simulation methodology outlined here aims to understand combustion processes, flame dynamics, and related phenomena associated with these hazardous flames.

Oxy-fuel, are of the highest laminar nature, with the temperature reaching ranges of 3200-3500 kelvin making research on real-life oxy flames a particularly unsafe area for combustion studies. Experiments are typically performed in specialized research facilities equipped with state-of-the-art equipment, safety protocols, and expert guidance. They aim to investigate flame characteristics, flame stability, heat release rates, and pollutant emissions, among other important parameters. However, due to the extreme conditions involved and a crucial area of combustion, the study hopes to expand our understanding of combustion and improve safety measures.

4 Model verification and validation

4.1 Counter Diffusion Flame Model

Luo et al. [52] experimented on the 1-dimensional model presented in Eqs. (18)-(21), by comparing it to an actual three-dimensional model. Their studies concluded that the 1-dimensional model represented the 3-dimensional, considering the actual reality. Som et al. [39] performed experiments for counterflow diffusion flame of syngas combustion with air, Wang et al. [38] performed simulations for the experiments, with the modified mechanism by Sun et al. [39]. Similar to the initial condition in this study comparing the simulation with the references, this section aimed to complete model verification and validation of the counter flow diffusion flame. Where the condition are set to conditions seen in Table 1 with fuel as equimolar CO/H_2,

Table 1: Conditions of validation cases et al. [37] [38]

Strain rate	PPF/NPF	Fuel composition	Oxidizer	z (cm)	$V_O = V_F(m/s)$	T (K)	P (atm)	Φ
35	NPF	$X_{CO/H_2} = 0.50/0.50$	Air	1.27	13.84	300	1	1
35	PPF	$X_{CO/H_2} = 0.50/0.50$	Air	1.27	13.84	300	1	6

Wang et al. [38] used two radiation models, OPT (Optical Thin Model) and SNBCK, simulated with the OPPDIF code [59]. The two models showed insignificant differences. Accordingly, the effects due to radiation are not of significant focus, thus the radiation model was not altered with and corresponds to the standard radiation model in Cantera [84]. The temperature profile as a function of the axial flame position for the two flames, as seen in Fig. 1, shows no significant differences compared to the simulations in the referenced studies. The model was concluded verified and validated for further investigations of the opposed-flow flames. The model was in addition compared using the Li mechanism, USC II mechanism, GriMech 3.0 mechanism, and the Davis mechanism. The shift seen for the temperature peak was in Som et al. [37] concluded to be a result of suction of excess fuel.

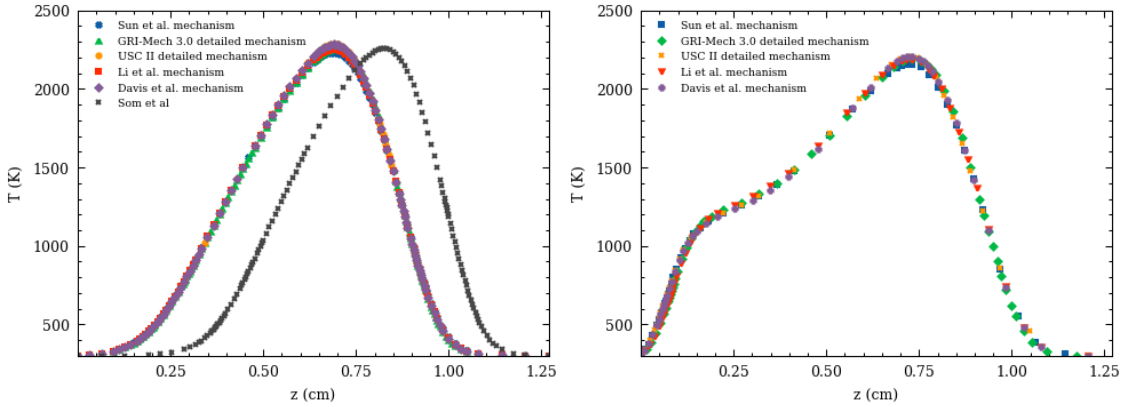

(a) A subfigure (b) A subfigure

Figure 7: A figure with two subfigures

4.2 Implemented Mechanism

The models utilized in this study were considered sufficiently accurate, as believed by previous researchers. It is important to emphasize that this work does not introduce any new mechanisms but instead employs previously validated mechanisms. The mechanism as modified by Sun et al. [39] was used and written in a file format manually. Thus to ensure the correct implementation of the mechanism a comparison seemed fit. For comparison the characterized flame by Wang et al. [38] is similar to the NPF case in Table 1 with the differences being the addition of H_2O. Respectively, the O_2/H_2O molar fraction ratio was set to 0.275/0.725. The temperature and species molar fractions are illustrated in Fig. 8, results of molar fractions CO, H_2, O_2, H_2O. The difference is seen to be insignificant for the flame model and mechanism, and the model and chemical mechanism can be concluded correctly and effectively employed.

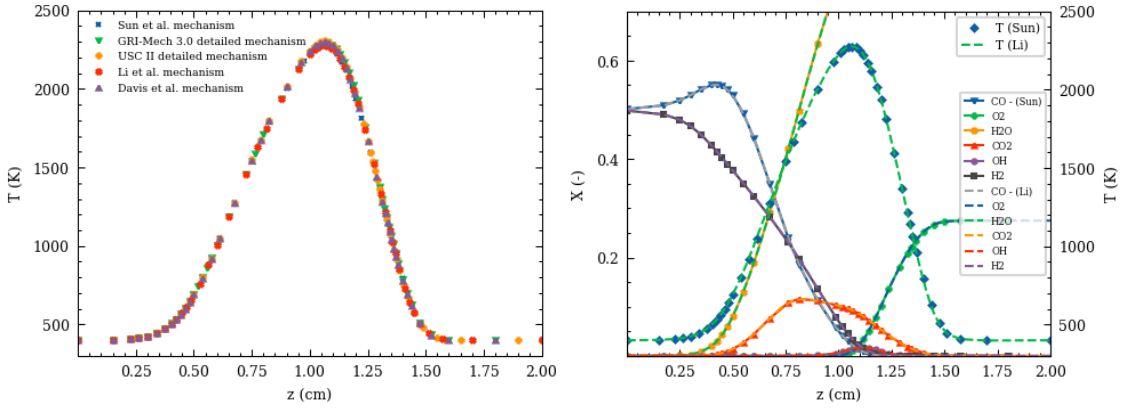

Figure 8: Temperature (T [K]) along the axial flame position (z [cm]) with five different mechanisms are compared. [39, 40, 41, 43, 45], and molar fractions of CO, H_2, O_2, H_2O, CO_2 and OH with Sun et al. [39] compared to Li et al. [43] mechanism with

Additionally, the molar fraction for species of CO, H_2, O_2, and H_2O are available for specific species with the different chemical mechanisms, see Appendix D.

4.3 Entropy Generation Model

The entropy generation model presented in this study was already deemed valid and verified in previous work [71]. Conducted experiments in counterflow diffusion flame with this model are not common. Lorentzen [72] studies were chosen in the project from previous work, because he used the same entropy generation model, verified and validated with the referenced experiments Som et al. [37] and Wang et al.[38], which is similar to the present cases. Thus, this section aimed to complete model verification and validation by comparing the two models.

The mass fluxes were set to 2 kg/(m^2s) for air and 1 kg/(m^2s) for fuel, for the counterflow diffusion flame. Table 2 shows the calculated entropy generation rate components integrated over the length of the domain as a function of time for conduction, diffusion, and chemical reactions. The calculated results show no significant differences, despite a lower mass diffusion for syngas, but the purpose of this section is to ensure the correct coding implementation. It was believed that the methane-air and syngas-air models could be deemed accurate enough and therefore it was reasonably concluded that the current models presented in this previous work were validated and verified, and could be used in further investigations.

Table 2: Integrated entropy generation along the axial position [kW/(m^2K)]

Methane-air	Present	Lorentzen [Table 1]
Conduction	323.7	317.4
Diffusion	118.9	119
Chemical	209.2	209.6
Syngas-air	Present	Lorentzen [Table 1]
Conduction	359.1	361.2
Diffusion	128.8	134.2
Chemical	86.8	86.8

5 Results and Discussion

This section presents the results of the conducted experiments and simulations and discusses their implications. The section is organized based on the parameters investigated, with each subsection presenting the results of varying parameters, an entropy generation analysis, followed by a corresponding discussion.

5.1 Temperature

5.1.1 Effect of varying inlet temperatures on the counter diffusion flame

To investigate the effects of temperature and water addition on the combustion process, three cases were selected with inlet temperatures of 400 K, 600 K, and 800 K to study the inlet temperature effects. The maximum temperature along the axis, with the addition of H_2O to the oxidizer, was determined for each temperature as illustrated in Fig. 9. In the left-sided results, the orange line represents T_{fuel} = $T_{oxidizer}$ = 400 K, the green line represents T_{fuel} = $T_{oxidizer}$ = 600 K, and the blue line represents T_{fuel} = $T_{oxidizer}$ = 800 K. These results were obtained using the detailed Gri-Mech 3.0 mechanism utilized in early studies. The results showed that increased inlet temperatures are flammable for higher concentrations of H_2O.

To assess the performance of the proposed mechanism, developed by Sun et al. [39], included for comparison: the Li mechanism and the Davis mechanism. Notably, the Li and proposed mechanisms consider three-body reaction mechanisms.

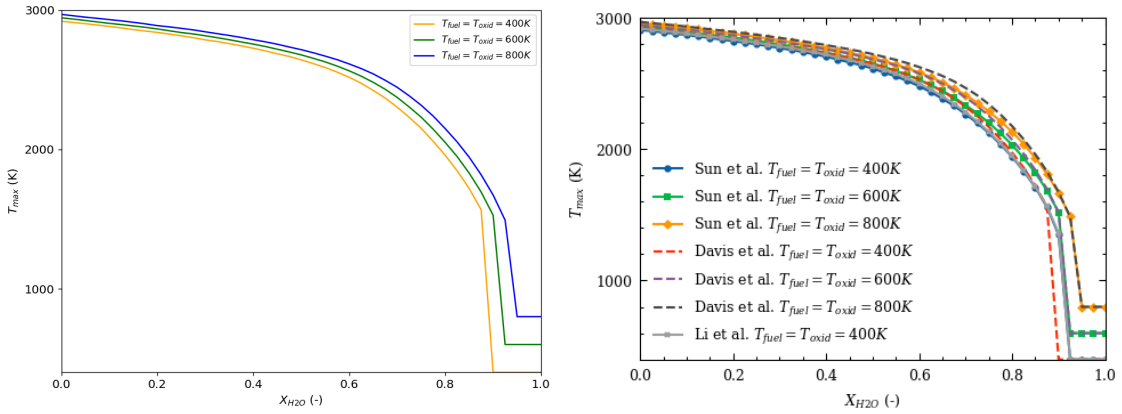

Figure 9: The maximum flame temperature (T_{max}) as a function of molar H_2O fraction (X_{H_2O}) in the oxidizer under conditions with different, but equal fuel and oxidizer inlet temperatures ($T_{oxidizer} = T_{fuel}$). p = 1 atm, $X_{CO} = 0.75$, $X_{H_2} = 0.25$, $\dot{m}_{fuel} = 1\ \frac{kg}{m^2 s}$, $\dot{m}_{oxidizer} = 2\ \frac{kg}{m^2 s}$.

A remarkable finding emerged after analyzing the results at an inlet temperature of 400 K. The mechanism lacking the three-body reaction mechanism showed extinction at a lower molar fraction of H_2O, specifically at approximately 0.90. This unprecedented observation was caught by surprise, indicating that optimizing the three-body mechanism in sustaining the combustion process in the presence of water is essential. In contrast, no discernible differences were observed among the

mechanisms investigated for higher inlet temperatures. Further, a good tool for understanding the chemical processes is rates contributions. Fig. 10 illustrates the top five reactions contributing to volumetric heat production in the case of inlet temperatures at 400 K, compared to the molar fraction at high concentration (X_{H_2O} = 0.80). Comparing the Sun mechanism to Gri-Mech 3.0 suggest that the three-body reactions contribute to a higher heat of reactions, considerably R13 is mainly the most significant contributor but is seen to be lower than R30 at high concentrations of CO. The five most contributed to heat of reaction are also available for other molar fractions of H_2O (X_{H_2O} = 0.20, 0.40, 0.60 and 0.80) at 400 K, 600 K, and 800 K in Appendix 6.2.

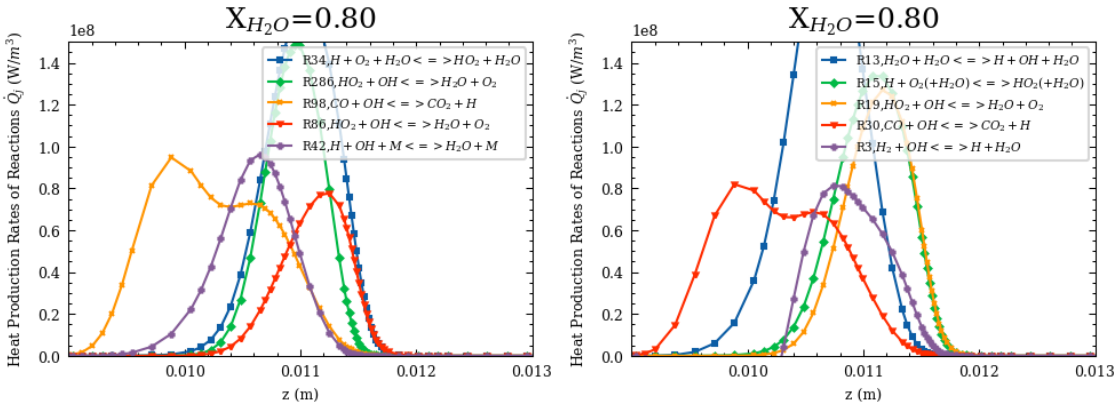

Figure 10: The maximum flame temperature (T_{max}) as a function of molar H_2O fraction (X_{H_2O}) in the oxidizer under conditions with different, but equal fuel and oxidizer inlet temperatures ($T_{oxidizer} = T_{fuel}$). p = 1 atm, $X_{CO} = 0.75$, $X_{H_2} = 0.25$, $\dot{m}_{fuel} = 1\ \frac{kg}{m^2 s}$, $\dot{m}_{oxidizer} = 2\ \frac{kg}{m^2 s}$.

As the molar fraction of H2O in the oxidizer increases, the heat release of these reactions also varies. This indicates the influence of water addition on the combustion process and its impact on the heat of reactions. These findings highlight the importance of water concentration in the oxidizer and its effect on the overall energy release during combustion. Further analysis of the reaction mechanisms and water's role in promoting or inhibiting specific reactions will provide deeper insights into the combustion behavior under varying conditions of water addition. Further, the temperature profile along the axis with the addition of 20 %, 40 %, 60 %, and 80 % molar diluent H_2O to pure O_2 oxidizer for the selected temperatures is illustrated in Fig. 11. The shape of the flame, other than starting at higher inlet temperatures, shows insignificant effects; some drops in temperatures at higher concentrations of H_2O can be seen.

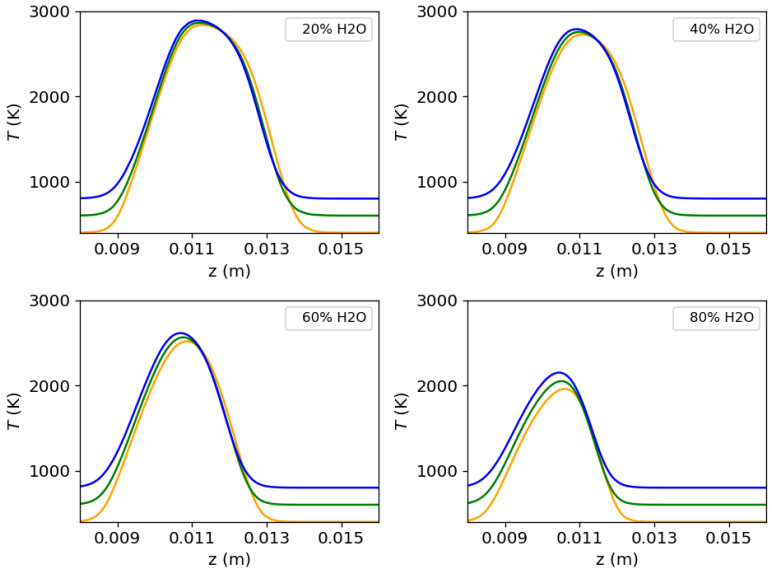

Figure 11: Temperature (T [K]) distributions along the flame axial position (z [m]) at X_{H_2O} = [0.20, 0.40, 0.60, 0.80] at $T_{fuel} = T_{oxidizer}$ = [400, 600, 800] K. p = 1 atm, $X_{CO} = 0.75$, $X_{H_2} = 0.25$, $\dot{m}_{fuel} = 1\ \frac{kg}{m^2 s}$, $\dot{m}_{oxidizer} = 2\ \frac{kg}{m^2 s}$.

The variation of different inlet temperatures was investigated at constant fuel inlet temperature, T_{fuel} = 400 K at varied oxidizer inlet temperatures of 400 K, 600 K, and 800 K. Accordingly, the temperature was investigated at constant oxidizer inlet temperature, $T_{oxidizer}$ = 400 K at varied fuel inlet temperatures of 400 K, 600 K, and 800 K. The results are illustrated in Fig. 13, at the maximum temperature along the axis, adding H2O to the syngas oxidizer for the selected temperatures. Respectively, the orange line represents 400 K, the green line represents 600 K, and the blue line represents = 800 K.

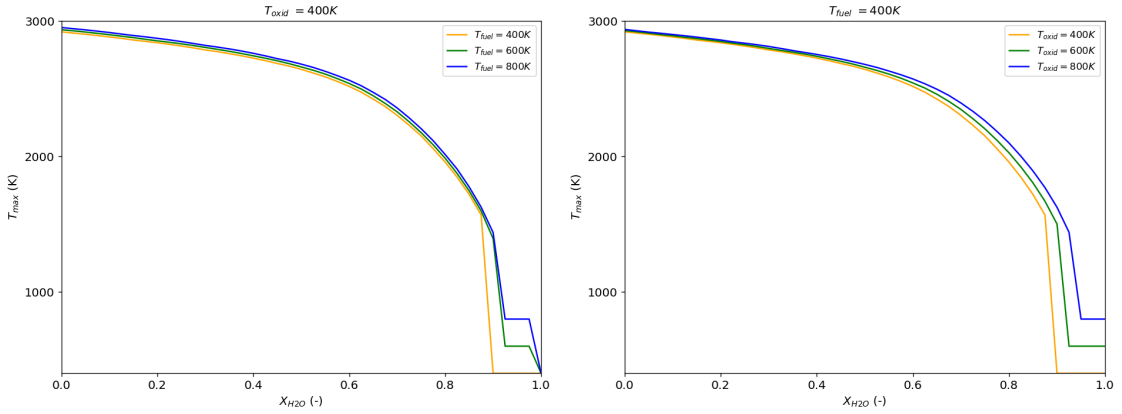

Figure 12: The maximum flame temperature (T_{max} [K]) as a function of molar H_2O fraction (X_{H_2O}) at T_{fuel} = 400 K and $T_{oxidizer}$ = 400 K. p = 1 atm, $X_{CO} = 0.75$, $X_{H_2} = 0.25$, $\dot{m}_{fuel} = 1\ \frac{kg}{m^2 s}$, $\dot{m}_{oxidizer} = 2\ \frac{kg}{m^2 s}$

Further, the temperature profile along the axis with the addition of 20 %, 40 %,

60 %, and 80 % molar diluent H_2O to pure O_2 oxidizer for the selected temperatures is shown in Fig. 13.

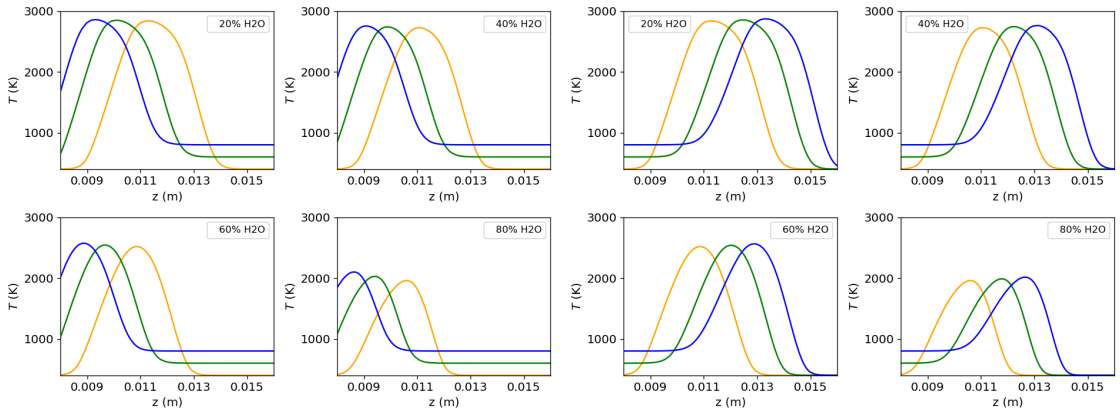

Figure 13: Temperature (T [K]) distributions along the flame axial position (z [m]) at $X_{H_2O} = [0.20,\ 0.40,\ 0.60,\ 0.80]$ at $T_{fuel} = 400$ K and $T_{oxidizer} = 400$ K. p = 1 atm, $X_{CO} = 0.75$, $X_{H_2} = 0.25$, $\dot{m}_{fuel} = 1\ \frac{kg}{m^2 s}$, $\dot{m}_{oxidizer} = 2\ \frac{kg}{m^2 s}$.

The results show that the effects are relatively insignificant and differ mainly from a shift of the flame profile, and the effects of using a three-body are expected to give the same results as the already established results. Accordingly, the result is not of concern in the next section, in which the impacts of temperature effects on entropy generation are reported for 400 K, 600 K, and 800 K.

5.1.2 Effect of Varying Inlet Temperatures on Conductive Heat Transfer Contribution to Entropy Generation

The influence of different inlet temperatures on conductive heat transfer within the flame was investigated. Fig. 14 presents the maximum conductive entropy generation ($\sigma_{cond,max}$) as a function of molar H_2O content (X_{H_2O}) for three different temperatures (400 K, 600 K, and 800 K). It can be observed that the maximum conductive entropy generation increases with increasing molar H_2O content. Additionally, at a given molar H_2O content, the maximum conductive entropy generation is higher for lower temperatures. This is attributed to the higher thermal gradients and increased conductive heat transfer rates at lower temperatures, leading to higher conductive entropy generation.

Based on theoretical expectations, it was anticipated that lower temperatures would lead to higher levels of conduction entropy generation. Revealed in our finding the maximum conductive entropy generation was found to be the largest at 400 K and the smallest at 800 K. The results of three-body mechanisms in the Li mechanism and Sun mechanism compared to Davis at 400K is as concluded by the temperature corresponding to a higher heat contribution from the reactions. Other than the effects already established the three-body reactions show no significant effects trough out the maximum entropy conduction generation and suggest that the reaction does play some but small effects.

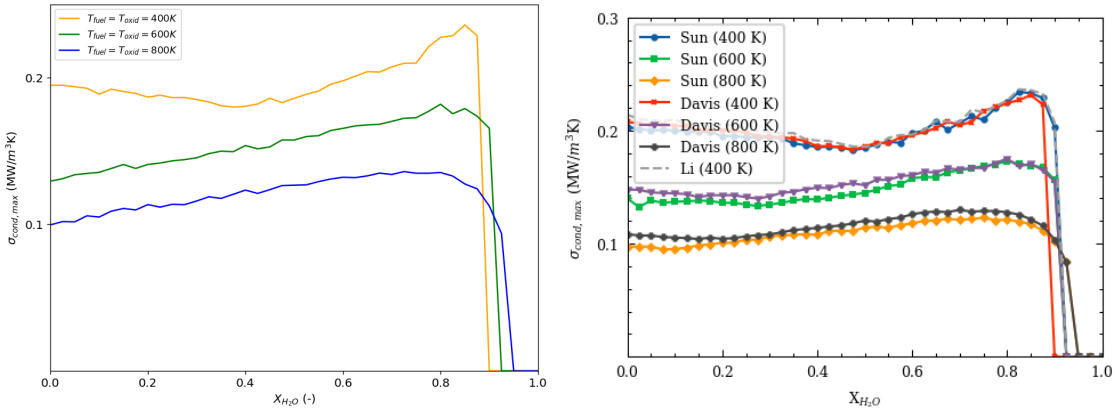

Figure 14: Maximum conduction entropy generation ($\sigma_{cond,max}$) as a function of molar H_2O fraction (X_{H_2O}) at $T_{fuel} = T_{oxidizer} = [400, 600, 800]$ K.

The distribution of conduction entropy generation along the flame length was examined at various molar H_2O fractions in the oxidizer (20%, 40%, 60%, and 80%). Fig. 15 illustrates the conduction entropy generation as a function of flame length for the three different inlet temperatures (400 K, 600 K, and 800 K) at the specified molar H_2O fractions. At 20% H_2O, the highest peak of conduction for 400 K is closer to the fuel inlet, while for 600 K and 800 K, the peak is slightly closer to the oxidizer inlet. As the H_2O content increases, the fuel peak decreases, and the oxidizer peak increases, resulting in a shift towards higher entropy generation near the oxidizer inlet. This behavior was consistent across all inlet temperatures.

These findings indicate that the distribution of conduction entropy generation

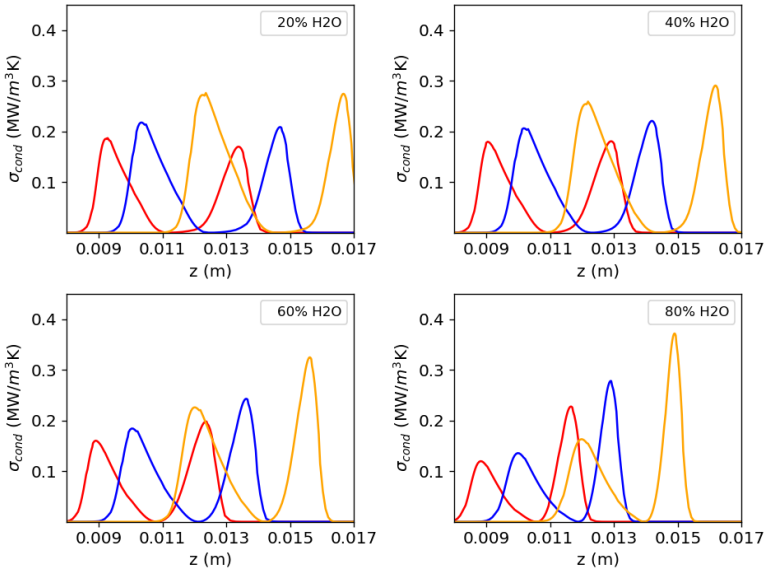

Figure 15: Conduction entropy generation distributions along the flame axial position at different molar H_2O fractions and temperatures.

within the flame is mainly governed by the water content in the oxidizer rather than the inlet temperature. The observed shift towards higher entropy generation near the oxidizer inlet with increasing water content can be attributed to the increased heat transfer from the oxidizer to the fuel due to the increased thermal conductivity of the mixture. It is worth noting that the changes in the flame structure and maximum flame temperature were relatively small as the water content in the oxidizer was increased. This suggests that, for inlet temperatures, the impact of water content on the overall flame behavior may be relatively small compared to other factors such as fuel composition, mass flux, and pressure.

In summary, the results indicate that water content in the oxidizer significantly affects the distribution of conduction entropy generation within the flame, while the inlet temperature may play a less significant role. Further investigations are needed to better understand the interplay between water content and other flame parameters and their impact on the overall flame behavior.

5.1.3 Effect of Varying Inlet Temperatures on Chemical Reaction Contribution to Entropy Generation

Continuing with the investigation of chemical reactions the effects of different, but equal inlet temperatures $T_{\text{fuel}} = T_{\text{oxidizer}}$ on maximum chemical entropy generation as a function of molar H_2O (X_{H_2O}) were examined at temperatures of 400 K, 600 K, and 800 K. The results are presented in Fig. 16.

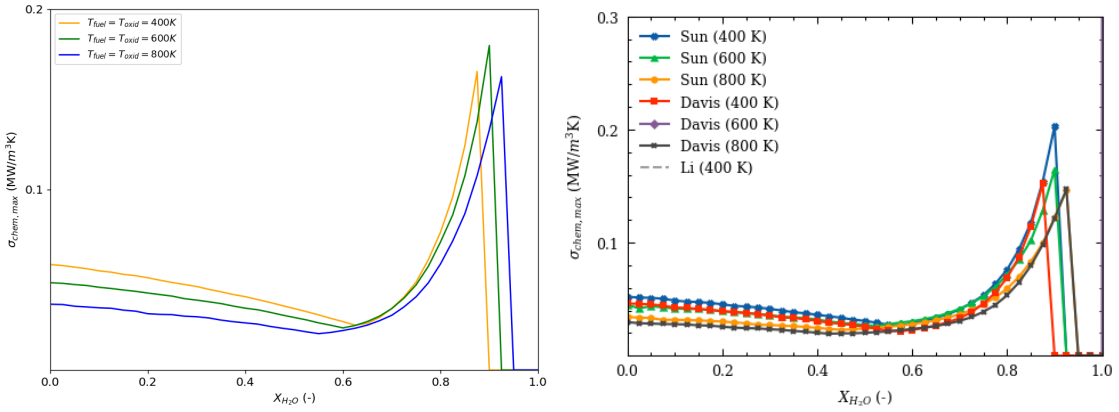

Figure 16: The maximum chemical entropy generation ($\sigma_{chem,max}$ $[\frac{MW}{m^3K}]$) as a function of molar H_2O fraction (X_{H_2O}) at $T_{fuel} = T_{oxidizer} = [400, 600, 800]$ K. p = 1 atm, $X_{CO} = 0.75$, $X_{H_2} = 0.25$, $\dot{m}_{fuel} = 1$ $\frac{kg}{m^2s}$, $\dot{m}_{oxidizer} = 2$ $\frac{kg}{m^2s}$.

Initially, it was observed that lower temperatures generated higher chemical entropy generation. However, with the addition of molar H_2O to the oxidizer, there was a decrease in maximum chemical entropy generation for all three cases. Eventually, the maximum chemical entropy generation reached a similar value at a molar fraction corresponding to $X_{H_2O} \approx 0.65$. Moreover, it was found that the maximum chemical entropy generation started to increase at lower levels of molar H_2O for higher temperatures, compared to lower temperatures. This suggests that higher temperatures promote more intense reactions and subsequently higher chemical entropy generation. Additionally, as the amount of molar H_2O increased, a significant increase in maximum chemical entropy generation was observed for all cases.

Initially, the case with an inlet temperature of 600 K exhibited the highest peak of maximum chemical entropy generation, surpassing even the case with the highest inlet temperature. Conversely, the case with an inlet temperature of 800 K demonstrated the lowest peak of maximum chemical entropy generation, despite having the highest inlet temperature. This discrepancy can be attributed to higher temperatures providing more energy to break chemical bonds, resulting in more complete combustion and less chemical entropy generation. In contrast, lower temperatures may lead to incomplete combustion, generating higher chemical entropy. When compared to the three-body reaction effect of the Sun mechanism and Li mechanism, the result was seen to be quite different, the three-body reactions that contribute to not going extinct as the Gri-Mech 3.0 and Davis mechanism, generated a large amount of entropy generation at 400 K that was not initially studied on.

Respectively, the Li mechanisms at 400 K illustrated in Fig. 16 followed the excact same path as the Sun mechanism. Due to three-body reactions, this large amount of chemical entropy generation is formed at the higher concentration on H_2O. It suggests the importance of three-body reactions to generate accurate results.

Further, the chemical entropy generation, along the axis with the addition of 20 %, 40 %, 60 %, and 80 % molar diluent H_2O to pure O_2 oxidizer is illustrated in Fig. 17

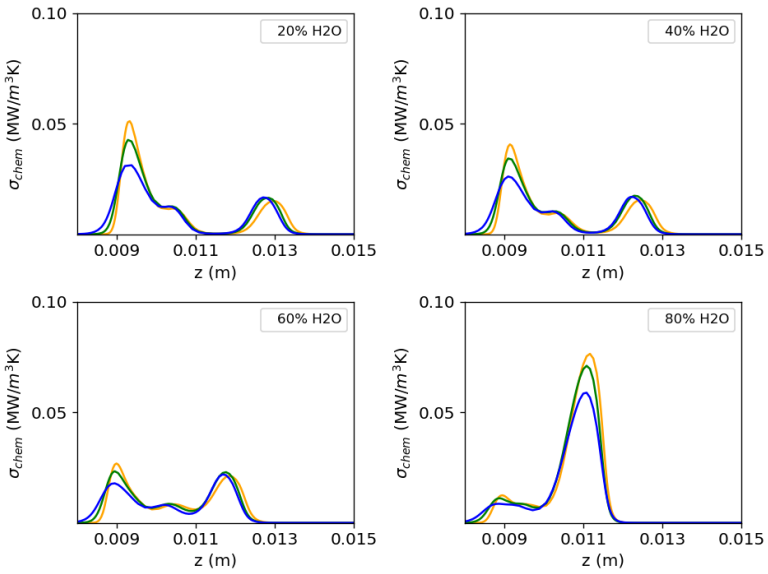

Figure 17: Chemical entropy generation (σ_{chem} $[\frac{MW}{m^3K}]$) distributions along the flame axial position (z [m]) at X_{H_2O} = [0.20, 0.40, 0.60, 0.80] at $T_{fuel} = T_{oxidizer}$ = [400, 600, 800] K. p = 1 atm, $X_{CO} = 0.75$, $X_{H_2} = 0.25$, $\dot{m}_{fuel} = 1$ $\frac{kg}{m^2s}$, $\dot{m}_{oxidizer} = 2$ $\frac{kg}{m^2s}$.

At lower levels of H_2O, the fuel peak was most pronounced, with the case at 400 K exhibiting the largest peak, followed by 600 K and 800 K. However, as the levels of molar H_2O increased, the fuel peak decreased in size, while no significant changes were observed for the oxidizer peak. At $X_{H_2O} = 0.60$, the similarity between the cases became almost identical, as anticipated from the results presented in Fig. 16. Furthermore, at $X_{H_2O} = 0.80$, a significant oxidizer peak formed due to the production of more OH radicals, leading to intensified fuel oxidation and, subsequently a higher oxidizer peak.

In summary, lower inlet temperatures generate higher chemical entropy, whereas higher temperatures generate lower ones. These findings are consistent with previous studies that have examined the influence of temperatures in counter-diffusion flames (Section 1.2.1). In addition the study indicates the importance of three-body reactions at high levels of molar H_2O. Whereas, higher temperatures show insignificant effects.

5.1.4 Effect of Varying Inlet Temperatures on Mass Diffusion Contribution to Entropy Generation And Total Entropy Generation

Mass diffusion, particularly the diffusion of water (H_2O), plays a crucial role in combustion processes, significantly influencing reactant transport, product formation, and overall combustion performance. In this section, we investigate the effect of water on mass diffusion by examining the maximum mass diffusion entropy generation ($\sigma_{diff,max}$) as a function of the molar fraction of water (X_{H_2O}). Fig. 27 illustrates the results, showing the variation of $\sigma_{diff,max}$ with X_{H_2O} for different inlet temperatures. It becomes evident that increasing the temperature promotes mass diffusion and enhances the chemical reactions within the flame. Higher temperatures result in higher maximum mass diffusion entropy generation, indicating more vigorous diffusion and increased chemical activity. The impact of H_2O is although not really affecting the mass diffusive entropy generation at low concentration, the impact is more pronounced at higher X_{H_2O} values. The case with Gri-Mech 3.0 mechanism showed all cases leveling out regardless of temperature beyond the extinction point. When compared to the three-body effects in the Sun mechanism there is seen a big drop for 400 K at the point corresponding to X_{H_2O} = 0.90.

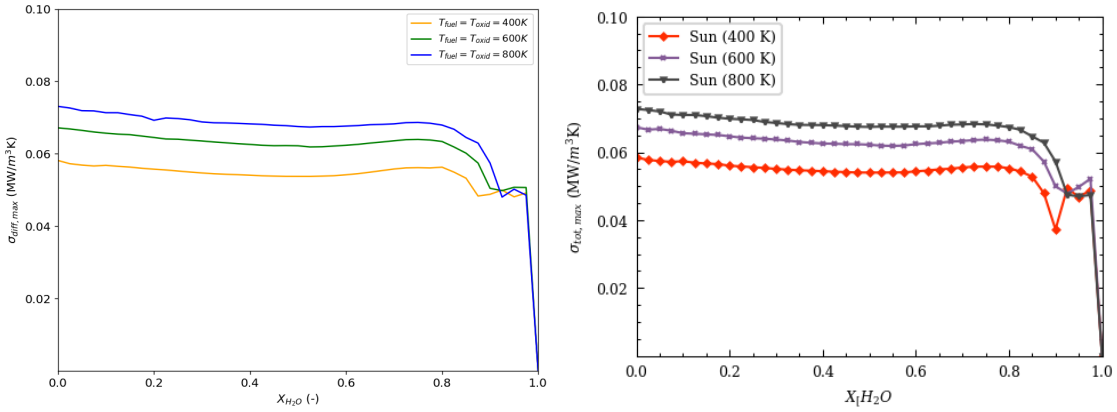

Figure 18: The maximum mass diffusion entropy generation ($\sigma_{dfiff,max}$ $[\frac{MW}{m^3K}]$) as a function of molar H_2O fraction (X_{H_2O}) at $T_{fuel} = T_{oxidizer}$ = [400, 600, 800] K. p = 1 atm, $X_{CO} = 0.75$, $X_{H_2} = 0.25$, $\dot{m}_{fuel} = 1\ \frac{kg}{m^2s}$, $\dot{m}_{oxidizer} = 2\ \frac{kg}{m^2s}$.

Illustrated in Fig. 28, the distribution of mass diffusion entropy generation σ_{diff} along the axial position (z) of the flame for specific X_{H_2O} values ([0.20, 0.40, 0.60, 0.80]) at the same inlet temperatures 400 K, 600 K and 800 K. The results demonstrate that higher temperatures enhance diffusion and, subsequently, higher entropy generation.

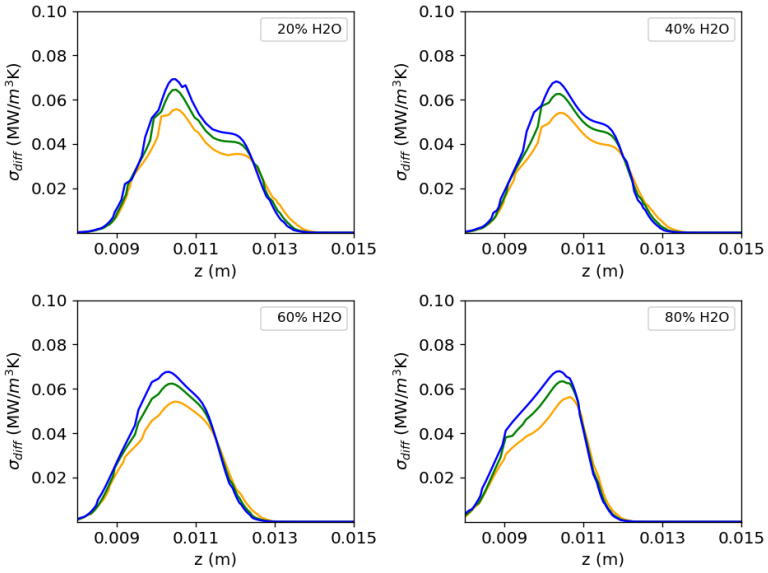

Figure 19: Mass diffusion entropy generation (σ_{diff} $[\frac{MW}{m^3K}]$) distributions along the flame axial position (z [m]) at X_{H_2O} = [0.20, 0.40, 0.60, 0.80] at $T_{fuel} = T_{oxidizer}$ = [400, 600, 800] K. p = 1 atm, $X_{CO} = 0.75$, $X_{H_2} = 0.25$, $\dot{m}_{fuel} = 1$ $\frac{kg}{m^2s}$, $\dot{m}_{oxidizer}$ = 2 $\frac{kg}{m^2s}$.

Finally, the total effects also take viscous forces into account, but the rate is small so not reported but the effects are accounted for. The influence of different inlet temperatures resulting in total entropy generation, illustrated in Fig. 29 is the sum of conduction, chemical reaction, mass diffusion, and viscous contribution. The radiative effects are not in this particular results taken into consideration. The largest contribution to the entropy generation is mainly through the effects of conduction but at a higher molar fraction of H_2O the effects are past by chemical reactions at least for the cases of inlet temperatures with 400 K.

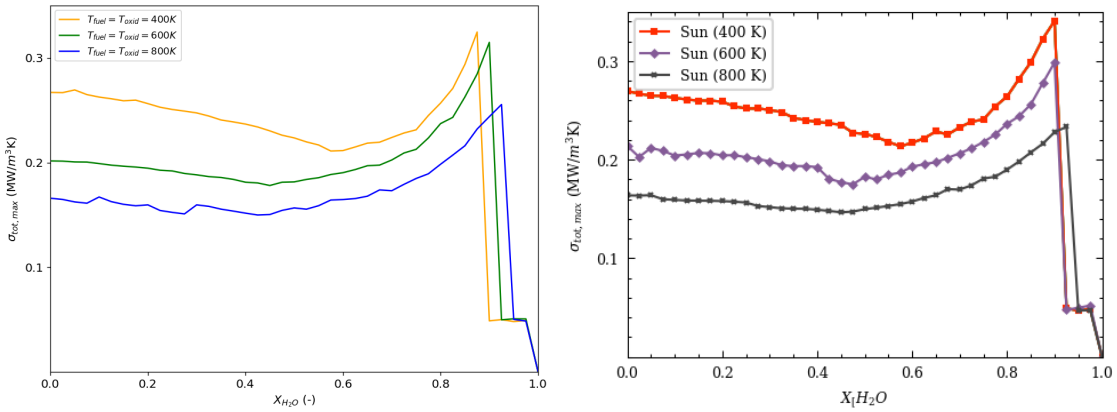

Figure 20: The maximum total entropy generation ($\sigma_{dfiff,max}$ $[\frac{MW}{m^3K}]$) as a function of molar H_2O fraction (X_{H_2O}) at $T_{fuel} = T_{oxidizer} = [400, 600, 800]$ K. p = 1 atm, $X_{CO} = 0.75$, $X_{H_2} = 0.25$, $\dot{m}_{fuel} = 1$ $\frac{kg}{m^2s}$, $\dot{m}_{oxidizer} = 2$ $\frac{kg}{m^2s}$.

5.1.5 Disscusion

Results investigated the effects of temperature and water addition on the combustion process. Three cases were selected with inlet temperatures of 400 K, 600 K, and 800 K to study the inlet temperature effects. The maximum temperature along the axis, with the addition of H_2O to the oxidizer, was determined for each temperature. The results showed that increased inlet temperatures are flammable for higher concentrations of H_2O. To assess the performance of the proposed mechanism, two other mechanisms (Li mechanism and Davis mechanism) were included for comparison. Notably, the Li and proposed mechanisms consider three-body reaction mechanisms. The first notable finding in the results was observed at an inlet temperature of 400 K. The mechanism lacking the three-body reaction mechanism showed extinction at a lower molar fraction of H_2O, specifically at approximately 0.90. This surprising observation highlights the importance of optimizing the three-body mechanism to sustain the combustion process in the presence of water. However, no discernible differences were observed among the mechanisms for higher inlet temperatures.

Further analysis was conducted to understand the chemical processes and their contribution to heat production. The top five reactions contributing to volumetric heat production were compared between the Sun mechanism and Gri-Mech 3.0 mechanism at 400 K and high concentration of CO. The results showed that the three-body reactions contribute to a higher heat of responses, with reaction R13 being the most significant contributor. However, at high concentrations of CO, reaction R30 was observed to be higher than R13. Similar analyses were performed for other molar fractions of H_2O and temperatures. The variation of different inlet temperatures was investigated, both at constant fuel inlet temperature and at constant oxidizer inlet temperature. The results showed that the effects of temperature variation were relatively insignificant, mainly resulting in a shift of the flame profile. The use of a three-body mechanism was expected to yield similar results as the already established findings.

The study investigated the influence of different inlet temperatures on conductive heat transfer within a flame. The maximum conductive entropy generation ($\sigma_{cond,max}$) was analyzed as a function of molar H_2O content (X_{H_2O}) for three different temperatures: 400 K, 600 K, and 800 K. The results showed that the maximum conductive entropy generation increases with increasing molar H_2O content. Moreover, at a given molar H_2O content, the maximum conductive entropy generation is higher at lower temperatures. This is attributed to the higher thermal gradients and increased conductive heat transfer rates at lower temperatures, leading to higher conductive entropy generation. The distribution of conduction entropy generation along the flame length was also examined for various molar H_2O fractions in the oxidizer (20%, 40%, 60%, and 80%). The findings indicated that as the H_2O content increases, the peak of conduction entropy generation shifts towards higher entropy generation near the oxidizer inlet. This behavior was consistent across all inlet temperatures.

Overall, the results suggest that the distribution of conduction entropy generation within the flame is primarily influenced by the water content in the oxidizer rather than the inlet temperature. The increased heat transfer from the oxidizer to the fuel, due to the increased thermal conductivity of the mixture with higher water content, is responsible for the observed shift in entropy generation. It is important to note that the changes in flame structure and maximum flame temperature were relatively small as the water content in the oxidizer increased, indicating that the impact of water content on the overall flame behavior may be relatively small compared to other factors such as fuel composition, mass flux, and pressure.

Further research is required to gain a better understanding of the interaction between water content and other flame parameters, as well as their overall impact on flame behavior. The investigation of chemical reactions in this study focused on the effects of different inlet temperatures ($T_{\text{fuel}} = T_{\text{oxidizer}}$) on maximum chemical entropy generation as a function of molar H_2O (X_{H_2O}). The temperatures examined were 400 K, 600 K, and 800 K. The results are presented in Figure 16.

The findings revealed that lower temperatures led to higher chemical entropy generation initially. However, as molar H_2O was added to the oxidizer, there was a decrease in maximum chemical entropy generation for all three cases. Eventually, the maximum chemical entropy generation reached a similar value at a molar fraction corresponding to $X_{H_2O} \approx 0.65$. Moreover, it was observed that higher temperatures resulted in the maximum chemical entropy generation starting to increase at lower levels of molar H_2O compared to lower temperatures. This suggests that higher temperatures promote more intense reactions and subsequently higher chemical entropy generation. Additionally, a significant increase in maximum chemical entropy generation was observed as the amount of molar H_2O increased for all cases.

Interestingly, the case with an inlet temperature of 600 K exhibited the highest peak of maximum chemical entropy generation, surpassing even the case with the highest inlet temperature of 800 K. On the other hand, the case with an inlet temperature of 800 K demonstrated the lowest peak of maximum chemical entropy generation, despite having the highest temperature. This discrepancy can be attributed to higher temperatures providing more energy to break chemical bonds, resulting in more complete combustion and less chemical entropy generation. In

contrast, lower temperatures may lead to incomplete combustion, generating higher chemical entropy.

The study also compared the three-body reaction effects of the Sun mechanism and Li mechanism. The results showed significant differences, with the three-body reactions in the Sun mechanism and Li mechanism generating a large amount of entropy generation at 400 K. This highlights the importance of three-body reactions for generating accurate results.

Furthermore, the distribution of chemical entropy generation along the flame axial position (z) was investigated by adding 20%, 40%, 60%, and 80% molar diluent H_2O to pure O_2 oxidizer. As the levels of molar H_2O increased, the fuel peak decreased in size, while no significant changes were observed for the oxidizer peak. At $X_{H_2O} = 0.60$, the cases became almost identical, as anticipated from the previous results. At $X_{H_2O} = 0.80$, a significant oxidizer peak formed due to the production of more OH radicals, leading to intensified fuel oxidation and a higher oxidizer peak. The effect of varying inlet temperatures on mass diffusion contribution to entropy generation and total entropy generation was also investigated. The results showed that increasing the temperature promoted mass diffusion and enhanced chemical reactions within the flame. Higher temperatures resulted in higher maximum mass diffusion entropy generation, indicating more vigorous diffusion and increased chemical activity. The impact of H_2O on mass diffusive entropy generation was more pronounced at higher X_{H_2O} values.

Finally, the total entropy generation, which includes contributions from conduction, chemical reaction, mass diffusion, and viscous forces, was examined. The results showed that increasing the inlet temperature resulted in higher total entropy generation, reflecting the combined effects of these processes.

5.2 Fuel Composition

5.2.1 Effect of varying Fuel Composition on the counter diffusion flame

To further investigate the behavior of the flame and with the addition of H_2O a counter diffusion flame was simulated to investigate the maximum temperatures along the flame axis as a function of the molar concentration of water (H_2O) in the oxidizer. Two different reaction mechanisms were considered: the Grimech mechanism and the Sun mechanism, which takes three-body reactions into consideration. The results of the simulation are presented in Figure 21, the left plot corresponding to the Gri-Mech 3.0 mechanism and the right plot corresponding to the Sun mechanism, respectively.

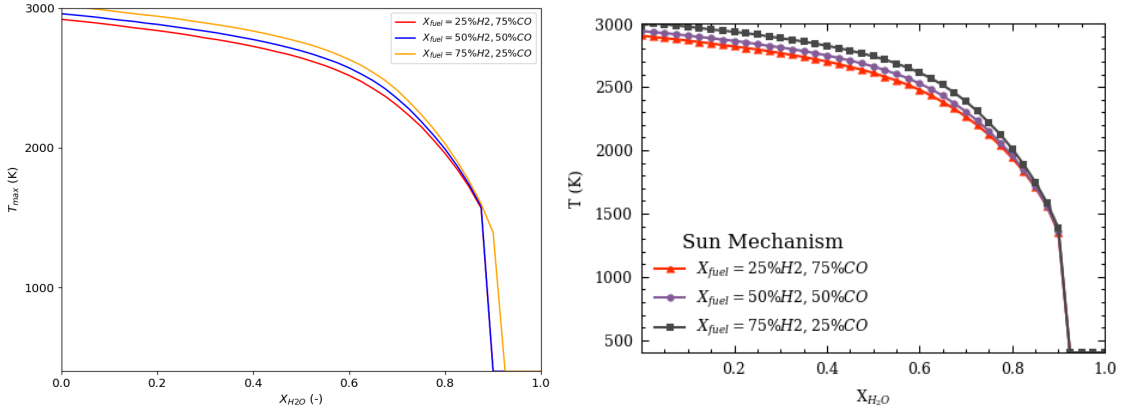

Figure 21: The maximum flame temperature (T_{max} [K]) as a function of molar H_2O fraction (X_{H_2O}) at X_{CO/H_2} = 25/75, 50/50, 75/25. p = 1 atm, $\dot{m}_{fuel} = 1\ \frac{kg}{m^2 s}$, $\dot{m}_{oxidizer} = 2\ \frac{kg}{m^2 s}$, $T_{fuel} = T_{oxidizer} = 400$ K.

It is observed that for fuel composition $X_{H_2} = 0.25$ and $X_{CO} = 0.75$, let's call it fuel composition 1 for further simplicity, the maximum temperature is relatively high initially. However, as the molar fraction of H_2O in the oxidizer increases, the temperature gradually decreases. Notably, fuel composition $X_{H_2} = 0.50$ and $X_{CO} = 0.50$, fuel composition 2, and fuel composition $X_{H_2} = 0.75$ and $X_{CO} = 0.25$, respectively, fuel composition 3, higher temperatures are achieved compared to fuel composition 1. This trend indicates that increasing the molar fraction of H_2 in the fuel leads to higher maximum temperatures. However, an interesting observation is that all fuel compositions follow the same trend until a molar fraction of H_2O equal to 0.80 in the oxidizer. Beyond this point, the maximum temperature remains constant for all fuel compositions until reaching a molar fraction of H_2O equal to 0.90, where all cases eventually go extinct.

This result demonstrates that the inclusion of three-body reactions in the Sun mechanism prevents the extinction of the flame for fuel compositions 1 and 2 in contrast to the Grimech mechanism. Further, the temperature profile along the axis with the addition of 20 %, 40 %, 60 %, and 80 % molar diluent H_2O to pure O_2 oxidizer for the three cases are illustrated in Fig. 22. Already seen, that maximum temperatures are rather unchanged, the same can be seen for the profile. The only

significant difference is that a higher amount of H_2, respectively lower amounts of CO, shifts toward the oxidizer inlet.

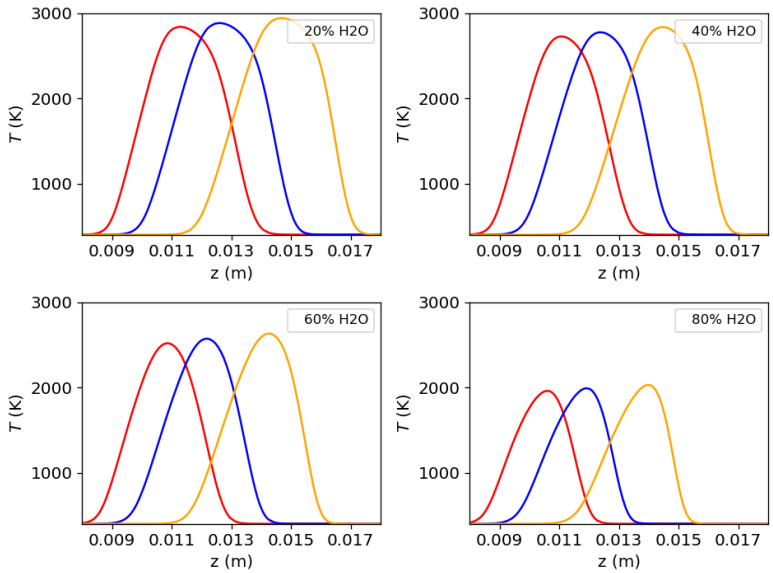

Figure 22: Temperature (T [K]) distributions along the flame axial position (z [m]) at X_{H_2O} = [0.20, 0.40, 0.60, 0.80] at X_{CO/H_2} = 25/75, 50/50, 75/25. p = 1 atm, $\dot{m}_{fuel} = 1\ \frac{kg}{m^2 s}$, $\dot{m}_{oxidizer} = 2\ \frac{kg}{m^2 s}$, $T_{fuel} = T_{oxidizer} = 400$ K.

5.2.2 Effect of Fuel Composition on the Conductive Entropy Generation

In addition to temperature and oxidizer humidity, the fuel composition also plays a significant role in determining the conduction entropy generation within the flame. To investigate this effect, the maximum conduction entropy generation of the studied fuel compositions as a function of molar H_2O fraction (X_{H_2O}) was compared, as shown in Fig. 23.

Fig. 23 clearly demonstrates that the fuel composition substantially impacts the maximum conduction entropy generation. It can be observed that fuels with lower molar X_{CO} and higher molar X_{H_2} exhibit higher maximum conduction entropy generation. This result is consistent with previous studies (REF), which have shown that hydrogen-rich fuels tend to have higher combustion efficiency and heat release rates, leading to increased conduction entropy generation.

Interestingly, as molar H_2O was added to the oxidizer, the maximum conduction entropy generation showed minimal changes at low levels of H_2O, but slight decreases were observed. However, as the levels of H_2O increased, the entropy generation began to increase. Among the fuel compositions, the largest increase in conduction entropy generation was observed for the 25CO/75H_2 case, followed by 50CO/50H_2, and 75CO/25H_2 with a lower increase.

To gain further insights into the effect of fuel composition on conduction entropy generation, the distribution of entropy generation along the flame length was examined for the three fuel cases at different percentages of H_2O in the oxidizer. Fig. 24

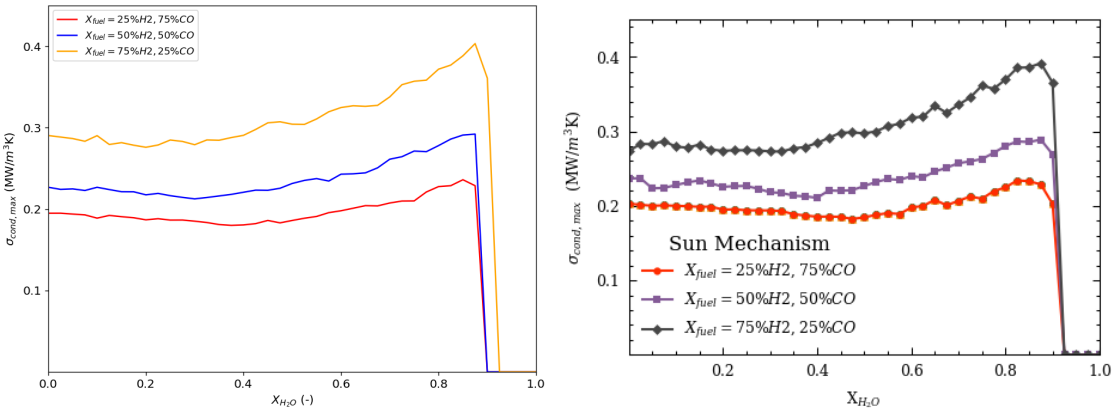

Figure 23: The maximum conduction entropy generation ($\sigma_{cond,max}$ $[\frac{MW}{m^3K}]$) as a function of molar H_2O fraction (X_{H_2O}) at X_{CO/H_2} = 25/75, 50/50, 75/25. p = 1 atm, $\dot{m}_{fuel} = 1$ $\frac{kg}{m^2s}$, $\dot{m}_{oxidizer} = 2$ $\frac{kg}{m^2s}$, $T_{fuel} = T_{oxidizer} = 400$ K.

presents the conduction entropy generation as a function of flame position for the three fuel cases at 20%, 40%, 60%, and 80% molar H_2O fraction in the oxidizer.

At low levels of H_2O, the conduction entropy generation peaks are relatively similar for all fuel compositions. However, as more molar H_2O was added, the peak on the oxidizer side increased, while the peak on the fuel side decreased. This behavior was observed for all fuel compositions, but the effect was more pronounced with higher levels of molar H_2. As the percentage of H_2O in the oxidizer reached higher levels, the differences between the fuel cases became more apparent.

The observed trend of higher maximum entropy generation with higher levels of molar H_2 and lower levels of molar CO in the fuel is consistent with previous studies. It can be attributed to the higher combustion efficiency and heat release rate associated with hydrogen-rich fuels. The cooling effect of H_2O on flames is believed to contribute to the shift in conduction entropy generation peaks towards the oxidizer side as the percentage of H_2O in the oxidizer increases.

The differences between the three fuel cases became more apparent as the percentage of H_2O in the oxidizer increased. This can be explained by the fact that the effect of H_2O on the flame is more pronounced for fuels with higher levels of molar H_2 due to the greater cooling effect H_2O has on hydrogen combustion. Thus, the observed trend of decreasing fuel peak and increasing oxidizer peak with increasing H_2O levels was more significant for the higher X_{H_2} fuel.

These results highlight the intricate interplay between fuel composition, oxidizer humidity, and conduction entropy generation within the flame. The findings contribute to a better understanding of the fundamental principles governing combustion and can have implications for the design of more efficient and environmentally friendly combustion systems.

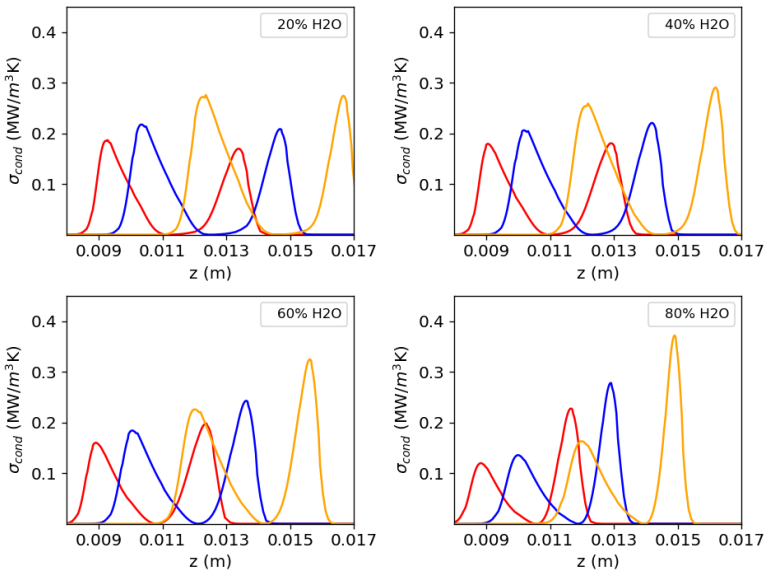

Figure 24: Conduction entropy generation (σ_{cond} $[\frac{MW}{m^3K}]$) distributions along the flame axial position (z [m]) at X_{H_2O} = [0.20, 0.40, 0.60, 0.80] at X_{CO/H_2} = 25/75, 50/50, 75/25. p = 1 atm, $\dot{m}_{fuel} = 1\ \frac{kg}{m^2 s}$, $\dot{m}_{oxidizer} = 2\ \frac{kg}{m^2 s}$, $T_{fuel} = T_{oxidizer} = 400$ K.

5.2.3 Effects of Fuel Composition on Chemical Entropy Generation

The effect of fuel composition on maximum chemical entropy generation as a function of molar H_2O was investigated for fuel compositions with CO/H_2 molar ratios of 25/75, 50/50, and 75/25. The results are illustrated in Fig 25.

Initially, slight differences in the maximum chemical entropy generation were observed among the different fuel compositions. However, as molar H_2O was added to the oxidizer, a noticeable decrease in the maximum chemical entropy generation was observed for all three cases. The decline was more pronounced as the molar fraction of H_2O increased.

For the fuel composition with CO/H_2 molar ratio of 25/75, the maximum chemical entropy generation reached a minimum at a molar fraction corresponding to $X_{H_2O} \approx 0.55$. On the other hand, for fuel compositions with CO/H_2 molar ratios of 50/50 and 75/25, the minimum value of maximum chemical entropy generation was observed at molar fractions of $X_{H_2O} \approx$ 0.60-0.65.

Furthermore, it was found that the fuel composition with CO/H_2 molar ratio of 25/75 exhibited the most significant chemical contribution, followed by the configurations with CO/H_2 molar ratios of 50/50 and 75/25. This suggests that the fuel composition significantly influences the maximum chemical entropy generation.

It is worth noting that the maximum chemical entropy generation was observed to peak just before the flame went extinct for all fuel compositions. This indicates that flame behavior and extinction are closely linked to the chemical entropy generation process. H_2O o further investigate the effects of fuel composition and molar H_2O fraction on chemical entropy generation, and additional analyses were performed.

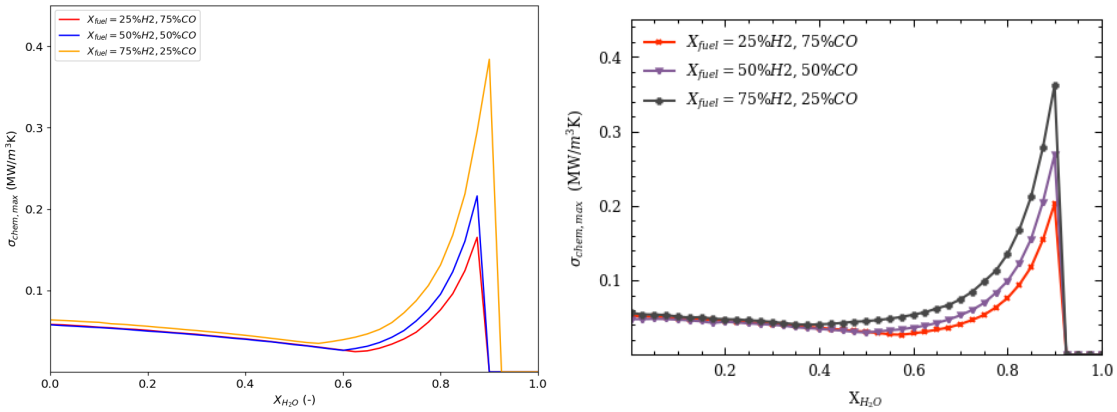

Figure 25: The maximum chemical entropy generation ($\sigma_{chem,max}$ $[\frac{MW}{m^3K}]$) as a function of molar H_2O fraction (X_{H_2O}) at X_{CO/H_2} = 25/75, 50/50, 75/25. p = 1 atm, $\dot{m}_{fuel} = 1$ $\frac{kg}{m^2 s}$, $\dot{m}_{oxidizer} = 2$ $\frac{kg}{m^2 s}$, $T_{fuel} = T_{oxidizer} = 400$ K.

Fig. 26 presents the chemical entropy generation distributions for different fuel compositions at specific molar fractions of H_2O (X_{H_2O} = 0.20, 0.40, 0.60, and 0.80).

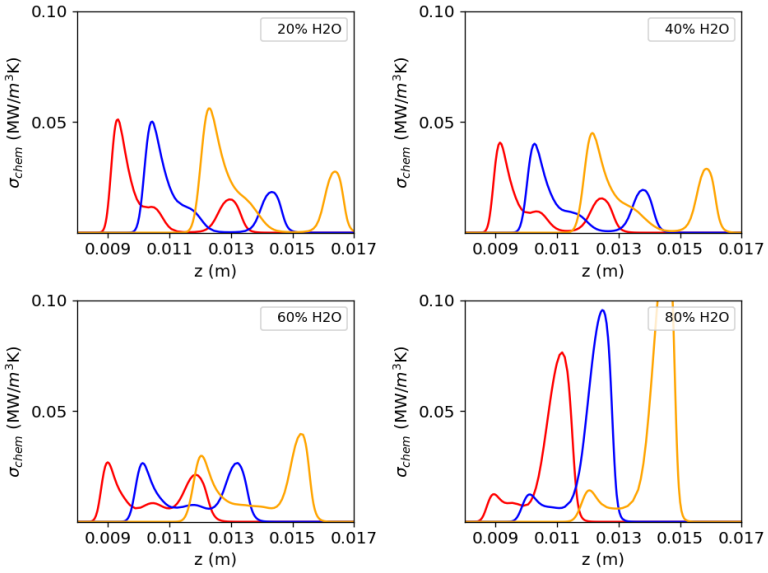

Figure 26: The chemical entropy generation ($\sigma_{chem,max}$ $[\frac{MW}{m^3K}]$) as a function of molar H_2O fraction (X_{H_2O}) at X_{CO/H_2} = 25/75, 50/50, 75/25. p = 1 atm, $\dot{m}_{fuel} = 1$ $\frac{kg}{m^2 s}$, $\dot{m}_{oxidizer} = 2$ $\frac{kg}{m^2 s}$, $T_{fuel} = T_{oxidizer} = 400$ K.

At $X_{H_2O} = 0.20$, the largest contribution to chemical entropy generation was observed on the fuel side for all fuel compositions. This suggests that at lower levels of H_2O in the oxidizer, the fuel composition plays a dominant role in determining the chemical entropy generation.

At $X_{H_2O} = 0.40$, the oxidizer side showed relatively little change, while the fuel side exhibited a slight decrease in chemical entropy generation. This indicates that the addition of H_2O to the oxidizer has a limited effect on the chemical activity of

the oxidizer at this molar fraction.

As X_{H_2O} increased to 0.60, significant effects of H_2O addition became evident. The oxidizer side started to form, and it was observed that the fuel composition with CO/H_2 molar ratio of 25/75 had a larger contribution on the oxidizer side compared to the fuel side. This suggests that at higher levels of H_2O, the oxidizer becomes more influential in determining the chemical entropy generation.

At $X_{H_2O} = 0.80$, a large peak in chemical entropy generation was observed on the oxidizer side for all fuel compositions, accompanied by a smaller contribution from the fuel side. This indicates that at high molar fractions of H_2O, the oxidizer becomes the primary contributor to chemical entropy generation, while the fuel side plays a secondary role.

These findings highlight the intricate relationship between fuel composition, molar H_2O fraction, and chemical entropy generation. The results provide valuable insights into the combustion processes and energy conversion systems, aiding in the optimization of these systems for improved efficiency and performance.—

5.2.4 Effect of Fuel Compositions on Mass Diffusion Contribution to Entropy Generation And Total Entropy Generation

In this section, we investigate the effect of water on mass diffusion by examining the maximum mass diffusion entropy generation ($\sigma_{diff,max}$) as a function of the molar fraction of water (X_{H_2O}). Fig. 27 illustrates the results, showing the variation of $\sigma_{diff,max}$ with X_{H_2O} for the different fuel compositions. It becomes evident that higher fuel composition of H_2 promotes mass diffusion and enhances the chemical reactions within the flame. Higher temperatures result in higher maximum mass diffusion entropy generation, indicating more vigorous diffusion and increased chemical activity. The effect of which higher H_2 composition promoted. Different from the prior section, the impact of H_2O shows is seen to show a bit more effects as the concentration dilutes the mass diffusive entropy generation decreases slightly at low concentration. The case with Gri-Mech 3.0 mechanism for fuel composition 3, compared to fuel composition 1 and 2 shows some similarities when compared to the three-body effects in the Sun mechanism where a big drop is seen at the point corresponding to $X_{H_2O} = 0.90$.

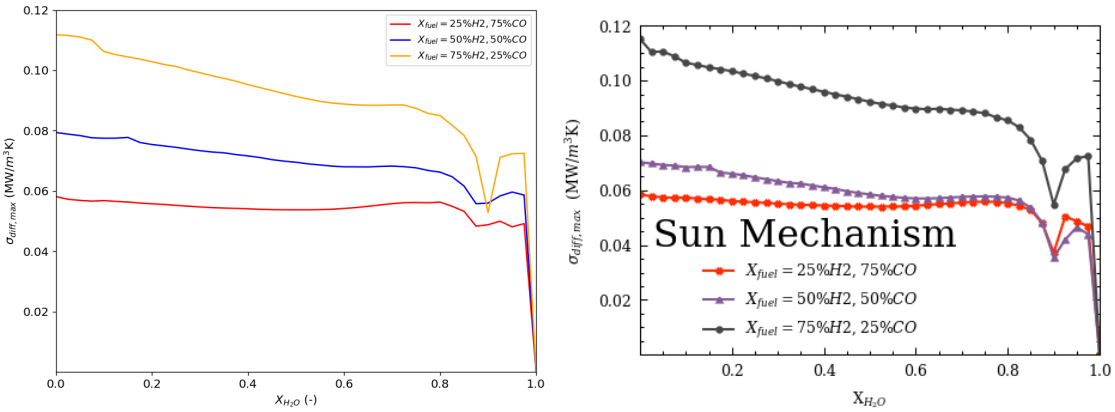

Figure 27: The maximum mass diffusion entropy generation ($\sigma_{dfiff,max}$ $[\frac{MW}{m^3K}]$) as a function of molar H_2O fraction (X_{H_2O}) at X_{CO/H_2} = 25/75, 50/50, 75/25. p = 1 atm, $\dot{m}_{fuel} = 1$ $\frac{kg}{m^2s}$, $\dot{m}_{oxidizer} = 2$ $\frac{kg}{m^2s}$, $T_{fuel} = T_{oxidizer} = 400$ K.

Illustrated in Fig. 28, the distribution of mass diffusion entropy generation σ_{diff} along the axial position (z) of the flame for specific X_{H_2O} values ([0.20, 0.40, 0.60, 0.80]) at the same different fuel compositions. The results demonstrate that higher H_2 composition enhances diffusion and, subsequently, higher entropy generation.

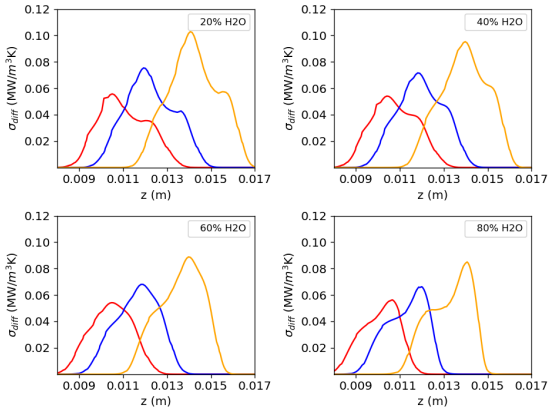

Figure 28: Mass diffusion entropy generation (σ_{diff} $[\frac{MW}{m^3K}]$) distributions along the flame axial position (z [m]) at X_{H_2O} = [0.20, 0.40, 0.60, 0.80] at X_{CO/H_2} = 25/75, 50/50, 75/25. p = 1 atm, $\dot{m}_{fuel} = 1$ $\frac{kg}{m^2s}$, $\dot{m}_{oxidizer} = 2$ $\frac{kg}{m^2s}$, $T_{fuel} = T_{oxidizer} = 400$ K.

Finally, the total effects also take viscous forces into account, but the rate is small so not reported but the effects are accounted for. The influence of different fuel compositions resulting in total entropy generation, illustrated in Fig. 29 is the sum of conduction, chemical reaction, mass diffusion, and viscous contribution. The radiative effects are not in this particular results taken into consideration. The most significant contribution to the entropy generation is mainly through the effects of conduction, but at a higher molar fraction of H_2O chemical reactions are a significant contributor.

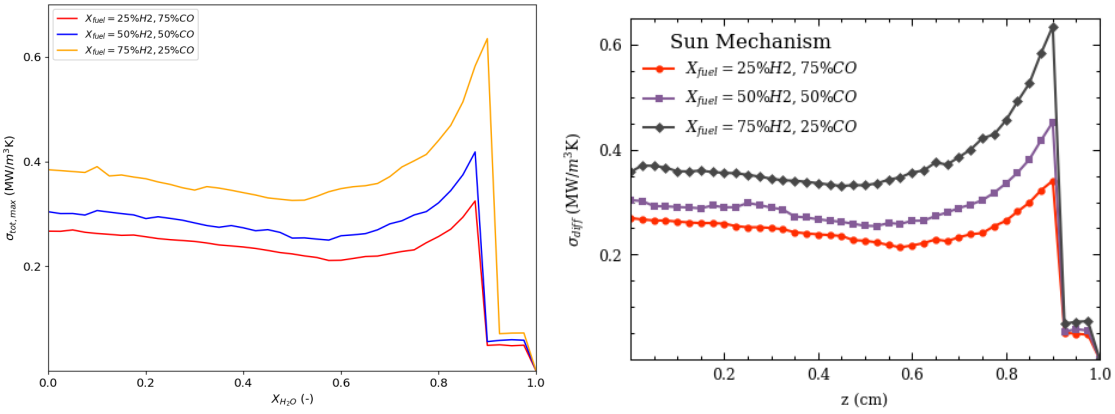

Figure 29: The maximum total entropy generation ($\sigma_{dfiff,max}$ $[\frac{MW}{m^3K}]$) as a function of molar H_2O fraction (X_{H_2O}) at X_{CO/H_2} = 25/75, 50/50, 75/25. p = 1 atm, $\dot{m}_{fuel}$ = 1 $\frac{kg}{m^2s}$, $\dot{m}_{oxidizer}$ = 2 $\frac{kg}{m^2s}$, $T_{fuel} = T_{oxidizer}$ = 400 K.

5.2.5 Discussion

The effects on the flammability limit of molar H_2O with various fuel compositions are compared in Fig. 21. At small X_{H_2O}, the maximum flame temperature showed some, but rather small differences. Following the maximum flame temperature as X_{H_2O} increased the differences became even smaller until the flame went extinct at around 88% molar H_2O for the cases with the fuel molar ratio 75/25 and 50/50 CO/H_2 and the fuel molar ratio 25/75 CO/H_2 went extinct at around 90-92% molar H_2O. Compared to temperature, the variations in fuel compositions showed a smaller impact on the flammability limit.

In the case of fuel ratios $X_{CO}/X_{H_2} = 75/25$ and $X_{CO}/X_{H_2} = 50/50$. The extinction occurs at equal percentages of molar H_2O in the oxidizer as a result of the overall fuel composition having a similar reaction kinetic. When the CO/H_2 ratio is smaller, the reaction kinetics are faster, and the flame temperature is higher, also seen in Fig. 22, which can enhance the mixing of the fuel and oxidizer and promote flame sustainability. As a result, the molar fuel ratio CO/H_2 = 25/75 leads to faster reaction kinetics and therefore higher flame temperatures compared to the other two cases.

Moving on to the conduction entropy generation, it is found that the fuel composition significantly influences the maximum conduction entropy generation. Fuels with lower molar CO and higher molar H_2O exhibit higher maximum conduction entropy generation. This result is consistent with previous studies and can be attributed to the higher combustion efficiency and heat release rates associated with hydrogen-rich fuels.

When H_2O is added to the oxidizer, the maximum conduction entropy generation shows minimal changes at low levels of H_2O but starts to increase as the levels of H_2O increase. The largest increase in conduction entropy generation is observed for the fuel composition with 25% CO and 75% H_2, followed by 50% CO and 50% H_2, and 75% CO and 25% H_2 with a lower increase. The distribution of entropy generation along the flame length shows that as more H_2O is added, the peak on the oxidizer side increases while the peak on the fuel side decreases. This behavior is more pronounced for fuels with higher levels of molar H_2, indicating the cooling effect of H_2O on flames.

The provided text discusses the effects of water on mass diffusion and entropy generation in combustion processes. It presents several figures that illustrate the relationship between the molar fraction of water (X_{H_2O}), fuel composition, and different entropy generation components.

Starting with chemical entropy, Fig. 25 shows that increasing the molar fraction of water leads to a decrease in the maximum chemical entropy generation ($\sigma_{chem,max}$). This reduction is more pronounced with higher water fractions and is influenced by the fuel composition. Specifically, the CO/H_2 molar ratio of 25/75 exhibits the highest chemical entropy generation. Fig. 26 further demonstrates that the fuel composition has a greater impact on chemical entropy generation at lower water fractions, while the oxidizer becomes more influential as the molar fraction of water increases.

Moving on to mass diffusion entropy, Fig. 27 reveals that higher fuel compo-

sitions of H_2 promote mass diffusion and enhance chemical reactions within the flame. This effect is more pronounced at higher temperatures. Interestingly, the addition of water slightly decreases mass diffusion entropy generation at low concentrations. Moreover, there is a similarity observed between fuel composition 3 and the Gri-Mech 3.0 mechanism, where a significant drop occurs at $X_{H_2O} = 0.90$.

Fig. 28 provides insight into the distribution of mass diffusion entropy generation along the axial position of the flame for specific molar fractions of water. It demonstrates that higher H_2 compositions result in enhanced diffusion and, consequently, higher entropy generation.

Considering the total effects, Fig. 29 illustrates the maximum total entropy generation, which includes contributions from conduction, chemical reactions, mass diffusion, and viscous forces. Conduction is found to have the most significant contribution to entropy generation, but chemical reactions become more substantial at higher molar fractions of H_2O.

In summary, the text highlights that the presence of water in combustion processes has a significant influence on entropy generation. It affects both chemical entropy and mass diffusion entropy, with the fuel composition and temperature playing crucial roles. The findings provide valuable insights for optimizing combustion systems, considering factors such as fuel composition and water content, to improve efficiency and performance.

5.3 Mass Flux And Pressure

Due to little time, the mass flux and pressure won't be addressed in the exact details as temperature seen in Section 5.1 and fuel composition seen in Section 5.2, respectively, in comparison to the sun mechanism. There is still a lot of good data, but explicitly not addressing the three-body reactions, and the simulated results are only solved with the Gri-Mech 3.0 Mechanism. The sections are also slightly different, as there are first provided results and then discussion before addressing the entropy generation.

5.3.1 Effect of Varying Mass Fluxes on the Counter Diffusion Flame

To study the effects of different fuel and oxidizer inlet mass fluxes, three cases were tested, and the following fuel/oxidizer mass fluxes were set: $\dot{m}_{fuel}/\dot{m}_{oxidizer} = 1/2\ \left[\frac{kg}{m^2 s}\right]$, $\dot{m}_{fuel}/\dot{m}_{oxidizer} = 5/10\ \left[\frac{kg}{m^2 s}\right]$ and $\dot{m}_{fuel}/\dot{m}_{oxidizer} = 10/20\ \left[\frac{kg}{m^2 s}\right]$. The maximum flame temperature as a function of diluent molar H_2O fraction in the oxidizer is shown in Fig. 30. Respectively, the fuel/oxidizer mass flux ratio 1/2 is represented in red, 5/10 in green, and 10/20 in orange.

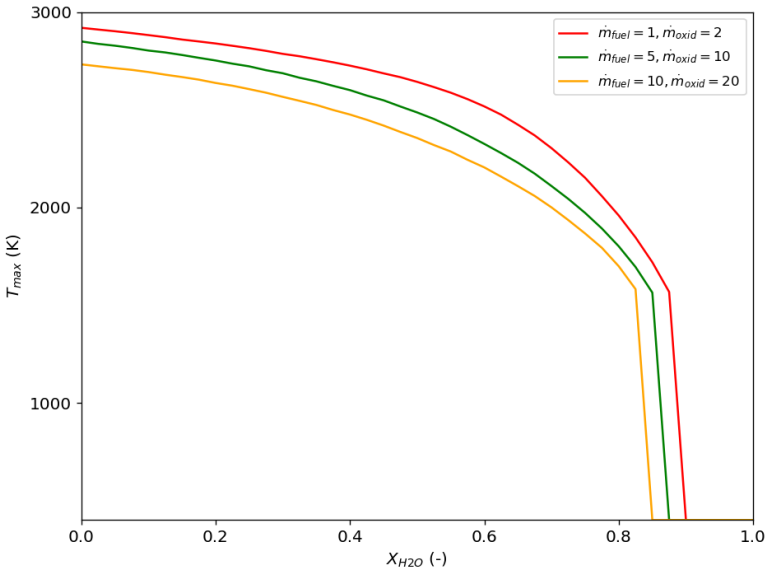

Figure 30: The maximum flame temperature (T_{max} [K]) as a function of molar H_2O fraction (X_{H_2O}) at $\dot{m}_{fuel} = [1, 5, 10]\ \frac{kg}{m^2 s}$, $\dot{m}_{oxidizer} = [2, 10, 20]\ \frac{kg}{m^2 s}$. p = 1 atm, $X_{CO} = 0.75$, $X_{H_2} = 0.25$, $T_{fuel} = T_{oxidizer} = 400$ K.

Further, the temperature profile along the axis with the addition of 20 %, 40 %, 60 %, and 80 % molar diluent H_2O to pure O_2 oxidizer for the three cases are shown in Fig. 31.

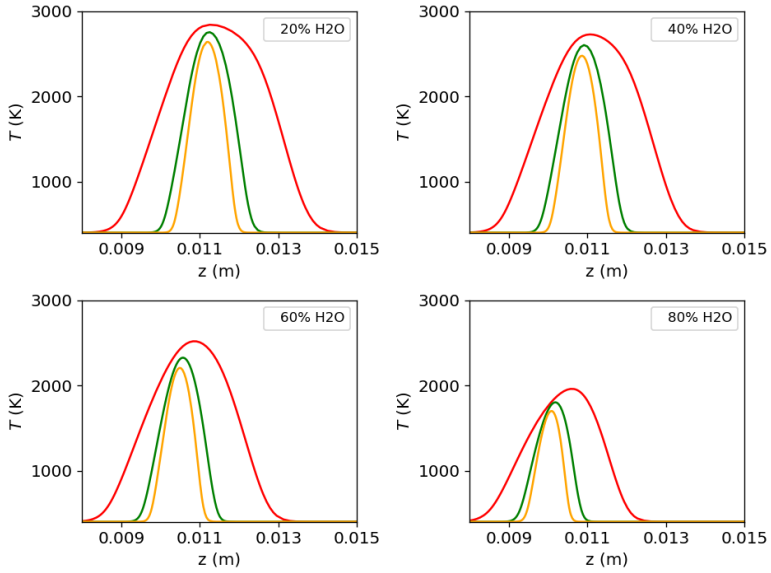

Figure 31: Temperature (T [K]) distributions along the flame axial position (z [m]) at X_{H_2O} = [0.20, 0.40, 0.60, 0.80] at $\dot{m}_{fuel}$ = [1, 5, 10] $\frac{kg}{m^2 s}$, $\dot{m}_{oxidizer}$ = [2, 10, 20] $\frac{kg}{m^2 s}$. p = 1 atm, X_{CO} = 0.75, X_{H_2} = 0.25, T_{fuel} = $T_{oxidizer}$ = 400 K.

To study the effects of equal fuel and oxidizer inlet mass fluxes, four cases were set: $\dot{m}_{fuel}$ = $\dot{m}_{oxidizer}$ = 2, 5, 10, and 20 $\left[\frac{kg}{m^2 s}\right]$. The maximum flame temperature as a function of diluent molar H_2O fraction in the oxidizer is shown in Fig. 32. The fuel and oxidizer mass fluxes are represented as follows: $\dot{m}$ = 2 $\left[\frac{kg}{m^2 s}\right]$ in red, $\dot{m}$ = 5 $\left[\frac{kg}{m^2 s}\right]$ in blue, $\dot{m}$ = 10 $\left[\frac{kg}{m^2 s}\right]$ in orange, and $\dot{m}$ = 20 $\left[\frac{kg}{m^2 s}\right]$ in green.

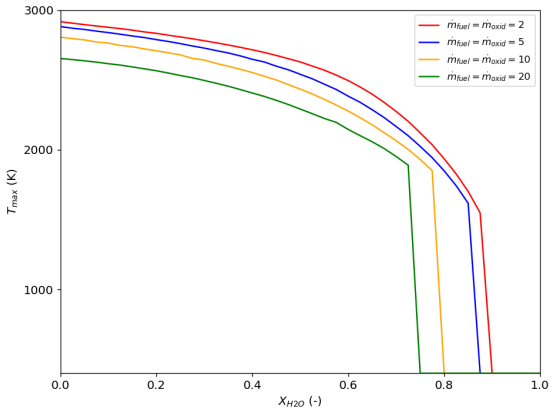

Figure 32: The maximum flame temperature (T_{max} [K]) as a function of molar H_2O fraction (X_{H_2O}) at $\dot{m}_{fuel}$ = $\dot{m}_{oxidizer}$ = [2, 5, 10, 20] $\frac{kg}{m^2 s}$. p = 1 atm, X_{CO} = 0.75, X_{H_2} = 0.25, T_{fuel} = $T_{oxidizer}$ = 400 K.

Further, the temperature profile along the axis with the addition of 20 %, 40 %, 60 %, and 80 % molar diluent H_2O to pure O_2 oxidizer for the four cases are shown in Fig. 33.

Studies were conducted with different and equal mass fluxes for the fuel and

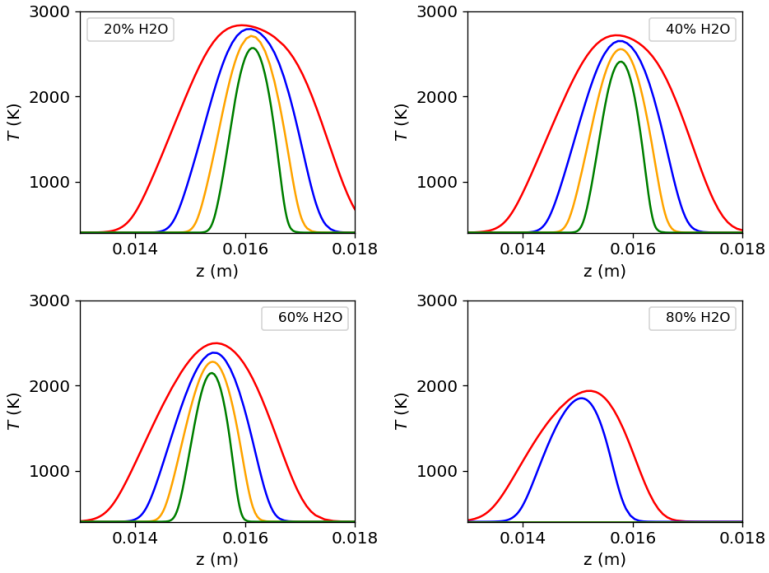

Figure 33: Temperature (T [K]) distributions along the flame axial position (z [m]) at X_{H_2O} = [0.20, 0.40, 0.60, 0.80] at $\dot{m}_{fuel} = \dot{m}_{oxidizer}$ = [2, 5, 10, 20] $\frac{kg}{m^2 s}$. p = 1 atm, $X_{CO} = 0.75$, $X_{H_2} = 0.25$, $T_{fuel} = T_{oxidizer} = 400$ K.

oxidizer inlets. However, for the cases where the mass fluxes weren't similar, the fuel/oxidizer mass flux ratio was kept the same, $\dot{m}_{fuel}/\dot{m}_{oxidizer} = 0.5$. This was mainly conducted to keep the flame zone close to the center.

Flame extinction is often studied by looking at the strain rate, closely related to the mass fluxes of the fuel and oxidizer. Here, the effects are investigated by choosing mass fluxes before simulating the flame. Still, one could also have specified an equivalence ratio, and the mass flux ratio between the fuel and the oxidizer would automatically be determined. This would be ideal if the oxidizer were a pure specie, hence irrelevant for the conducted studies due to water being added to the oxidizer.

The effects on the flammability limit of molar H_2O with similar mass flux ratios but different fuel and oxidizer mass fluxes are compared in Fig. 30. When the mass fluxes of fuel and oxidizer are increased, one can see that the flammability limit decreases, in terms of X_{H_2O}, with the increase of mass fluxes. This is a result of the mixing rates between the reactants increasing as mass fluxes are increased, which leads to higher reaction rates and faster heat release, resulting in a smaller flame zone, as seen from Fig. 31.

Eventually, telling us if the mass fluxes are increased beyond a certain point, the flame will become unstable and go extinct. It might be explained due to the higher momentum of reactant streams occurring at higher mass fluxes, which disrupts the flame structure and causes the reactant to separate before sufficient heat release. In addition to the smaller flame zone and increased extinction tendency, the flame temperature decrease with increasing mass flux. As a result of the higher mixing rates of the reactants, more heat is lost to the surroundings due to increased heat transfer.

The effects on the flammability limit of molar H_2O with equal mass fluxes for the fuel and oxidizer inlets are compared in Fig. 32. Similar to the different mass

flux cases, higher mass fluxes go extinct before the smaller ones, in terms of X_{H_2O}, and have a smaller flame temperature due to the increased mixing at higher mass fluxes. This leads to higher heat transfer rates to the surroundings and a reduced residence time for the reactants in the flame zone, resulting in incomplete combustion and, ultimately, flame extinction. As a result of more reactants introduced into the system, the flame zone and flame temperature decrease; see Fig. 33. Additionally, the cause of flame extinction occurring quicker at higher mass fluxes can be explained due to increased convective and radioactive cooling.

In summary, the studies investigated the effects of different and equal mass fluxes for the fuel and oxidizer inlets on flame extinction and flammability limit. The mixing rates between the reactants increased with higher mass fluxes, leading to higher reaction rates and faster heat release, resulting in a smaller flame zone and decreased flame temperature. As a result, if the mass fluxes are increased beyond a certain point, the flame will become unstable and extinct due to disrupted flame structure and separation of reactants. The flammability limit decreased with increasing mass fluxes, and higher mass fluxes went extinct before smaller ones. Increased convective and radioactive cooling explained the cause of flame extinction occurring quicker at higher mass fluxes.

5.3.2 Effect of Varying Pressure on the Counter Diffusion Flame

Five cases were selected with operating pressure 1, 2, 5, 10, and 20 atm to study the effects of pressure. The maximum flame temperature as a function of diluent molar H_2O fraction in the oxidizer is shown in Fig. 34. Respectively, 1 atm in orange, 2 in green, 5 in blue, 10 in red, and 20 in cyan.

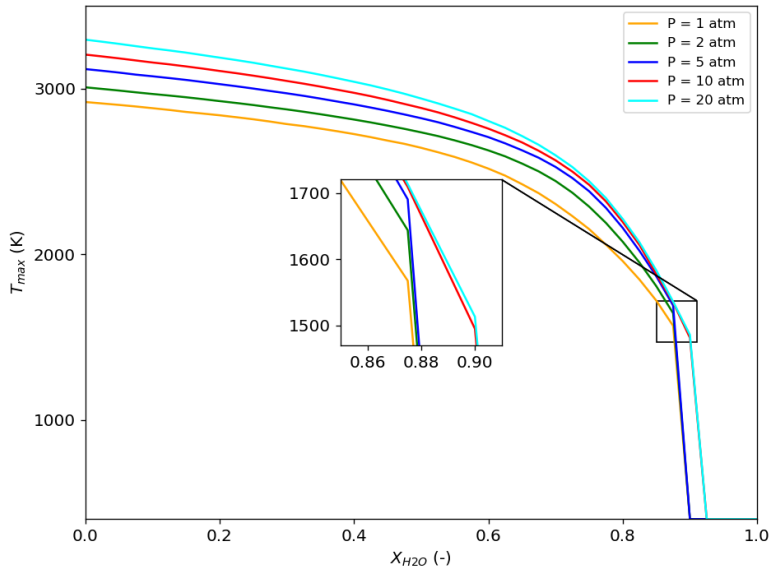

Figure 34: The maximum flame temperature (T_{max} [K]) as a function of molar H_2O fraction (X_{H_2O}) at p = [1, 2, 5, 10, 20] atm. $X_{CO} = 0.75$, $X_{H_2} = 0.25$, $\dot{m}_{fuel} = 1$ $\frac{kg}{m^2 s}$, $\dot{m}_{oxidizer} = 2$ $\frac{kg}{m^2 s}$, $T_{fuel} = T_{oxidizer}$=400 K.

Further, the temperature profile along the axis with the addition of 20 %, 40 %, 60 %, and 80 % molar diluent H_2O to pure O_2 oxidizer for the five pressure cases are shown in Fig. 35.

The different pressures studied showed that the force has an effect on the sustainability of the flame at low levels of molar H_2O, but the effect becomes smaller as X_{H_2O} increase. This behavior might be explained by considering the impact of pressure on diffusion rates and reaction kinetics. Since the diffusion rates are higher at higher pressures, which leads to better mixing of the reactants, enhancing reaction rates and increasing the flame temperature at higher pressures, seen in Fig. 34-35. This effect showed to be more pronounced at lower levels of X_{H_2O}, where the flame is more sensitive to changes in the mixing and reaction rates.

However, as the level of X_{H_2O} increases, one can see less of an effect on the flame temperature, and the flame extinction occurs at similar molar H_2O levels across different pressure cases. It might be a result of the mixing and reaction rates being less sensitive in the flame at higher X_{H_2O} as it is seen that all cases in the range 1-10 atm went extinct at more or less the same point, at around 88% molar H_2O. The reactions became increasingly controlled by water availability, resulting in slight differences in flame extinction.

The slightly higher extinction point, in terms of X_{H_2O}, for the flame at 20 atm might be explained by thermal energy. Thermal energy supplied to the system

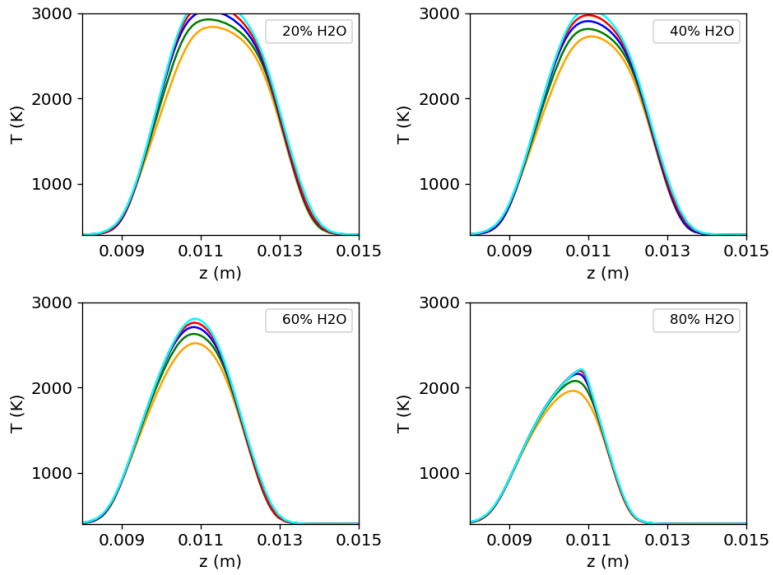

Figure 35: Temperature (T [K]) distributions along the flame axial position (z [m]) at X_{H_2O} = [0.20, 0.40, 0.60, 0.80] at p = [1, 2, 5, 10, 20] atm. $X_{CO} = 0.75$, $X_{H_2} = 0.25$, $\dot{m}_{fuel} = 1\ \frac{kg}{m^2 s}$, $\dot{m}_{oxidizer} = 2\ \frac{kg}{m^2 s}$, $T_{fuel} = T_{oxidizer} = 400$ K.

increases at higher pressures, enhancing the mixing and reaction rates. However, the effect is relatively small compared to the dominant control of water availability on flame sustainability at higher levels of molar H_2O.

Overall, these results suggest that the pressure has a minor impact on the sustainability of the flame at higher levels of molar H_2O. At the same time, the availability of water molecules becomes the dominant control of flame extinction.

5.3.3 Effect of Inlet Mass fluxes and Pressure on Conduction Entropy Generation

The effect of mass flux on maximum conduction entropy generation as a function of molar H_2O is investigated for the four cases with equal inlet fuel and oxidizer mass fluxes. Fig. 36 illustrates the results obtained. It can be observed that the effect of adding H_2O to the oxidizer depends on the mass flux of fuel and oxidizer. For the cases where $\dot{m} = 2$ and $\dot{m} = 5$, a minimal change in maximum conduction entropy generation is observed with the addition of H_2O; however, a slight increase is noticed. Conversely, the cases with higher fuel and oxidizer mass fluxes exhibit a noticeable increase in maximum conduction entropy generation as the molar H_2O in the oxidizer increases.

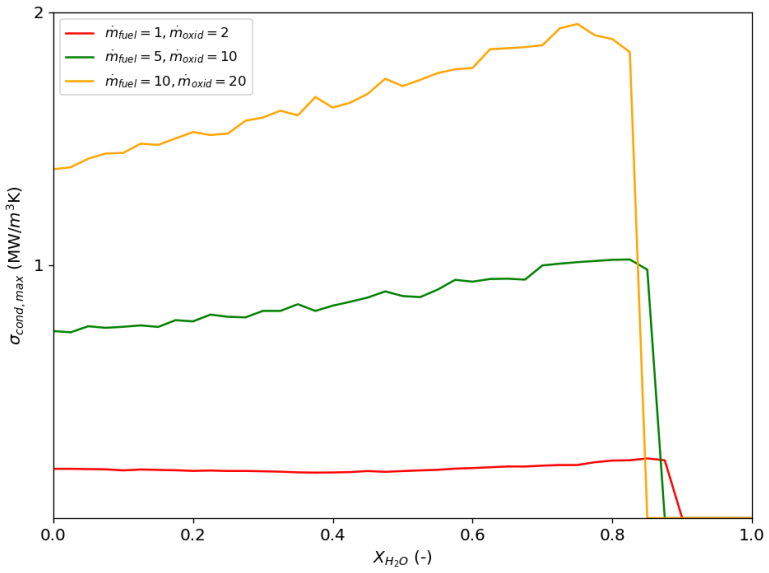

Figure 36: The maximum conduction entropy generation ($\sigma_{cond,max}$ $[\frac{MW}{m^3K}]$) as a function of molar H_2O fraction (X_{H_2O}) at $\dot{m}_{fuel} = [1, 5, 10]$ $\frac{kg}{m^2s}$, $\dot{m}_{oxidizer} = [2, 10, 20]$ $\frac{kg}{m^2s}$. p = 1 atm, $X_{CO} = 0.75$, $X_{H_2} = 0.25$, $T_{fuel} = T_{oxidizer} = 400$ K.

The results presented in this study suggest that conduction entropy generation in flames is dependent on the mass flux of fuel and oxidizer. When the mass flux of fuel and oxidizer is low, such as in the case with $\dot{m}_{fuel} = 1$ and $\dot{m}_{oxidizer} = 2$, a minimal change in maximum conduction entropy generation is observed with the addition of molar H_2O to the oxidizer. However, in cases with higher mass fluxes, such as $\dot{m}_{fuel} = 10$ and $\dot{m}_{fuel} = 20$ and $\dot{m}_{oxidizer} = 10$ and $\dot{m}_{oxidizer} = 20$, respectively, an increase in maximum conduction entropy generation is observed as the molar H_2O in the oxidizer increases.

One possible explanation for this observation is that the presence of H_2O in the oxidizer affects the heat transfer mechanisms in the flame. When the mass flux of fuel and oxidizer is high, the presence of water vapor in the oxidizer leads to higher heat losses from the flame to the surroundings, resulting in lower flame temperatures (see Section 3.2). Additionally, the higher mass fluxes could cause

more mixing of the fuel and oxidizer streams, leading to a more diffuse flame with a larger flame front area and, therefore, lower peak temperatures.

On the other hand, in cases where the mass flux of fuel and oxidizer is low, the effect of water vapor on the flame temperature is not significant enough to cause a substantial increase in maximum conduction entropy generation. In these cases, the observed increase in maximum conduction entropy generation with the addition of molar H_2O to the oxidizer is likely due to the effect of water vapor on the transport properties of the fluid. Water vapor can affect the thermal conductivity and specific heat capacity of the fluid, thereby influencing the heat transfer mechanisms in the flame.

Furthermore, the conduction entropy generation along the flame axial position was investigated at different X_{H_2O} concentrations, as illustrated in 37. The results demonstrate that as the X_{H_2O} concentration increases, the conduction moves closer to the oxidizer, and this difference is most pronounced with larger mass fluxes. This observation suggests that the presence of H_2O in the oxidizer can significantly impact flame characteristics by influencing the flame structure and heat transfer mechanisms.

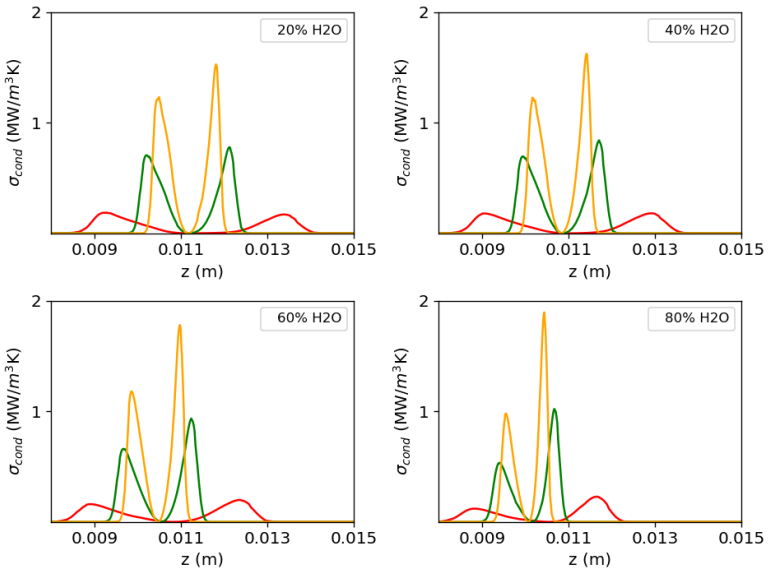

Figure 37: Conduction entropy generation (σ_{cond} $[\frac{MW}{m^3K}]$) distributions along the flame axial position (z [m]) at X_{H_2O} = [0.20, 0.40, 0.60, 0.80] at $\dot{m}_{fuel}$ = [1, 5, 10] $\frac{kg}{m^2s}$, $\dot{m}_{oxidizer}$ = [2, 10, 20] $\frac{kg}{m^2s}$. p = 1 atm, X_{CO} = 0.75, X_{H_2} = 0.25, T_{fuel} = $T_{oxidizer}$ = 400 K.

It is worth noting that even though smaller mass fluxes exhibit smaller changes in maximum conduction, the flame goes extinct at higher levels of X_{H_2O} compared to the higher mass fluxes. This observation indicates that flame extinctions occur at higher levels of X_{H_2O} for smaller mass fluxes, potentially due to the lower mass fluxes' increased sensitivity to changes in the reaction conditions. For instance, at lower mass fluxes, the flame may be more susceptible to quenching due to the increased heat capacity of the mixture with the addition of water vapor. Additionally,

the lower mass fluxes may have a narrower range of operating conditions in which the flame can be sustained. Finally, Fig. 2 presents the distributions of conduction entropy generation (σ_{cond}) along the flame axial position at various X_{H_2O} concentrations. As the X_{H_2O} concentration increases, the conduction moves closer to the oxidizer, and this trend is most pronounced with larger mass fluxes.

The effect of mass flux on maximum conduction entropy generation as a function of molar H_2O is shown in Fig. 38 for the four cases with equal inlet fuel and oxidizer mass fluxes. The results demonstrate that the effect of adding H_2O to the oxidizer depends on the mass flux of fuel and oxidizer. For the cases where $\dot{m} = 2$ and $\dot{m} = 5$, there is a minimal change in maximum conduction entropy generation with the addition of H_2O; however, a slight increase is observed. In contrast, the cases with higher fuel and oxidizer mass fluxes ($\dot{m} = 10$ and $\dot{m} = 20$) exhibit a noticeable increase in maximum conduction entropy generation as the molar H_2O in the oxidizer increases. Additionally, flame extinction occurs in the order of highest to lowest mass fluxes.

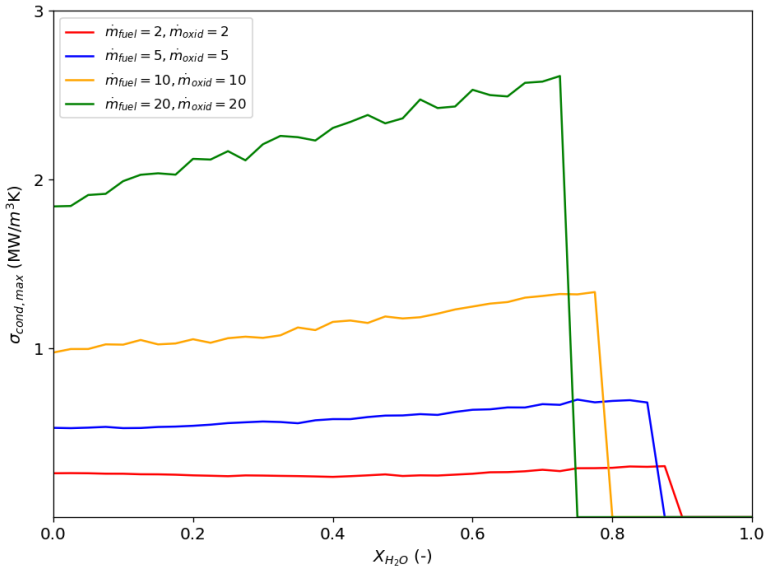

Figure 38: The maximum conduction entropy generation ($\sigma_{cond,max}$ $[\frac{MW}{m^3K}]$) as a function of molar H_2O fraction (X_{H_2O}) at $\dot{m}_{fuel} = \dot{m}_{oxidizer} = [2, 5, 10, 20]$ $\frac{kg}{m^2s}$. p = 1 atm, $X_{CO} = 0.75$, $X_{H_2} = 0.25$, $T_{fuel} = T_{oxidizer} = 400$ K.

The maximum conduction entropy generation ($\sigma_{cond,\max}$ $[\frac{MW}{m^3K}]$) is plotted as a function of molar H_2O fraction (X_{H_2O}) at $\dot{m}_{fuel} = \dot{m}_{oxidizer} = [2, 5, 10, 20]$ $\frac{kg}{m^2s}$ in Fig. 38. The results indicate that the presence of H_2O in the oxidizer has a significant impact on the conduction entropy generation, particularly at higher mass fluxes. The observed increase in maximum conduction entropy generation with the addition of molar H_2O to the oxidizer suggests that the heat transfer mechanisms in the flame are affected. When the mass flux of fuel and oxidizer is high, the presence of water vapor in the oxidizer leads to higher heat losses from the flame to the surroundings, resulting in lower flame temperatures (see Section 5.3.3). Moreover, the higher mass fluxes enhance the mixing of the fuel and oxidizer

streams, leading to a more diffuse flame with a larger flame front area and lower peak temperatures.

Conversely, when the mass flux of fuel and oxidizer is low, the effect of water vapor on the flame temperature is not significant enough to cause a substantial increase in maximum conduction entropy generation. In these cases, the observed increase in maximum conduction entropy generation with the addition of molar H_2O to the oxidizer can be attributed to the influence of water vapor on the transport properties of the fluid. Water vapor affects the thermal conductivity and specific heat capacity of the fluid, thus influencing the heat transfer mechanisms in the flame.

Furthermore, the effect of molar H_2O was investigated at X_{H_2O} = [0.20, 0.40, 0.60, 0.80]. Fig. 39 illustrates the distributions of conduction entropy generation (σ_{cond}) along the flame axial position at various X_{H_2O} concentrations and for $\dot{m}_{fuel}$ = $\dot{m}_{oxidizer}$ = [2, 5, 10, 20] $\frac{kg}{m^2 s}$. The results indicate that as the X_{H_2O} concentration increases, the conduction moves closer to the oxidizer. This trend is particularly pronounced with larger mass fluxes. Consequently, the presence of H_2O in the oxidizer significantly impacts flame characteristics by altering the flame structure and heat transfer mechanisms.

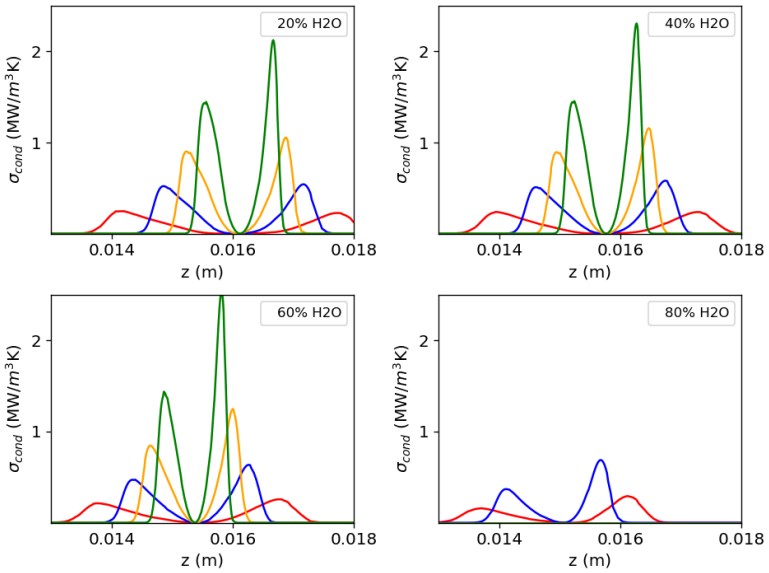

Figure 39: Conduction entropy generation (σ_{cond} $[\frac{MW}{m^3 K}]$) distributions along the flame axial position (z [m]) at X_{H_2O} = [0.20, 0.40, 0.60, 0.80] at $\dot{m}_{fuel}$ = $\dot{m}_{oxidizer}$ = [2, 5, 10, 20] $\frac{kg}{m^2 s}$. p = 1 atm, X_{CO} = 0.75, X_{H_2} = 0.25, T_{fuel} = $T_{oxidizer}$ = 400 K.

It is noteworthy that even though smaller mass fluxes exhibit smaller changes in maximum conduction entropy generation, the flame goes extinct at higher levels of X_{H_2O} compared to higher mass fluxes. This observation suggests that flame extinctions occur at higher X_{H_2O} levels for smaller mass fluxes, potentially due to the lower mass fluxes' increased sensitivity to changes in the reaction conditions. At lower mass fluxes, the flame may be more susceptible to quenching due to the

increased heat capacity of the mixture with the addition of water vapor. Additionally, the lower mass fluxes may have a narrower range of operating conditions in which the flame can be sustained.

Overall, the results presented in this study demonstrate that conduction entropy generation in flames is dependent on the mass flux of fuel and oxidizer. The addition of H_2O to the oxidizer influences the maximum conduction entropy generation and the distribution of conduction entropy along the flame axial position. The observed effects can be attributed to changes in flame temperature, heat transfer mechanisms, and fluid properties caused by the presence of water vapor.

5.3.4 Effect of Varying Pressure on Conductive Heat Transfer

The effects of pressure on maximum conduction entropy generation as a function of molar H_2O, X_{H_2O}, were investigated at various pressures (1 atm, 2 atm, 5 atm, 10 atm, and 20 atm). The results are presented in Fig. 40.

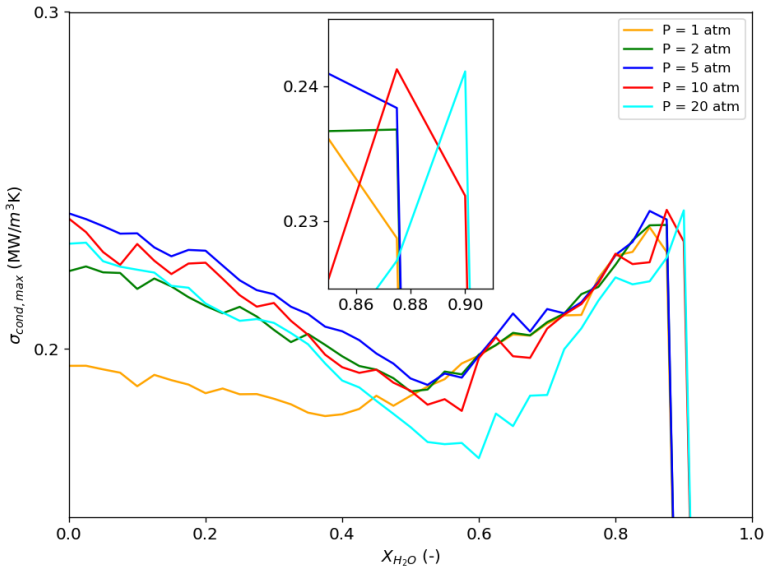

Figure 40: The maximum conduction entropy generation ($\sigma_{cond,max}$ $[\frac{MW}{m^3K}]$) as a function of molar H_2O fraction (X_{H_2O}) at p = [1, 2, 5, 10, 20] atm. $X_{CO} = 0.75$, $X_{H_2} = 0.25$, $\dot{m}_{fuel} = 1$ $\frac{kg}{m^2s}$, $\dot{m}_{oxidizer} = 2$ $\frac{kg}{m^2s}$, $T_{fuel} = T_{oxidizer}$=400 K.

At pure O_2 (corresponding to $X_{H_2O} = 0$ in the oxidizer), the maximum conduction entropy generation was smallest at 1 atm, followed by 2 atm, and then 20 atm, with the largest value at 5 atm, closely followed by 10 atm.

As H_2O was added to the oxidizer, a decrease in maximum conduction entropy generation was observed for all pressure cases. However, an eventual increase in maximum conduction entropy generation was also observed. The increase first occurred at around $X_{H_2O} \approx 0.40$ for 1 atm, followed by 2 atm and 5 atm. For 10 atm and 20 atm, the increase was observed at a higher value of molar H_2O, where the maximum conduction entropy generation reached a very low value for 20 atm at around $X_{H_2O} \approx 0.60$ before increasing again.

Eventually, all pressure cases reached near-identical maximum conduction entropy generation before going extinct. The extinction behavior was similar for 1 atm, 2 atm, and 5 atm, going extinct close to $X_{H_2O} \approx 0.88$. In contrast, 10 atm and 20 atm went extinct at a slightly higher value of molar X_{H_2O}, $X_{H_2O} \approx 0.90$, respectively.

Overall, the results indicate that pressure has an impact on the maximum conduction entropy generation. However, the pressure was primarily sensitive at lower levels of molar H_2O. The behavior of the maximum conduction entropy generation at different pressures suggests that pressure influences the flame structure and the competition between the effects of pressure and H_2O on the flame temperature.

The maximum conduction entropy generation ($\sigma_{cond,\max}$ $[\frac{MW}{m^3K}]$) as a function of molar H_2O fraction (X_{H_2O}) at pressures of 1 atm, 2 atm, 5 atm, 10 atm, and 20 atm was investigated. The results indicate that the behavior of the maximum conduction entropy generation varies with pressure. At pure O_2, the maximum conduction entropy generation was smallest at 1 atm, followed by 2 atm, and then 20 atm, with the largest value at 5 atm, closely followed by 10 atm. This behavior is consistent with previous studies that have shown an increase in the maximum flame temperature with pressure, leading to a decrease in maximum conduction entropy generation.

As molar H_2O increases, the maximum conduction entropy generation decreases for all pressure cases until a certain point, typically around $X_{H_2O} \approx 0.40$-0.60. At this point, the maximum conduction entropy generation starts to increase again. This behavior can be explained by

the quenching effect of H_2O on the flame, reducing the flame temperature and, consequently, the entropy generation. However, the reduction in temperature also reduces the combustion efficiency and heat release rate, leading to a decrease in the conduction entropy generation. Eventually, the effect of H_2O on the flame temperature overtakes its effect on combustion efficiency, resulting in an increase in the maximum conduction entropy generation.

The behavior of conduction entropy generation with pressure is dependent on the molar H_2O level. Lower pressure cases exhibit an increase in conduction entropy generation at lower levels of molar H_2O, while higher pressures show an increase at higher values of molar H_2O. These differences in behavior can be attributed to variations in heat and mass transfer rates, which are influenced by pressure.

The extinction behavior of the flame was also studied. It was found that all pressure cases reached near-identical maximum conduction entropy generation before going extinct. The extinction behavior was similar for 1 atm, 2 atm, and 5 atm, occurring around $X_{H_2O} \approx 0.88$, while 10 atm and 20 atm went extinct at slightly higher values of molar H_2O ($X_{H_2O} \approx 0.90$). The similar behavior of the maximum conduction entropy generation at the extinction point suggests that the mechanisms governing the extinction behavior are insensitive to pressure at high levels of molar H_2O.

The effects of pressure on conduction entropy generation as a function of flame position were also examined at different levels of molar H_2O ($X_{H_2O} = 0.20$, 0.40, 0.60, and 0.80). At $X_{H_2O} = 0.20$, the conduction entropy generation exhibited small differences among the pressure cases. A slightly lower fuel peak was observed at

1 atm compared to the other pressures. At the oxidizer peak, a more pronounced difference was observed for 20 atm, showing a lower oxidizer peak compared to the other pressure cases. However, as the molar level of H_2O increased, the effects of pressure became less distinct, and no significant differences were observed at X_{H_2O} = 0.80.

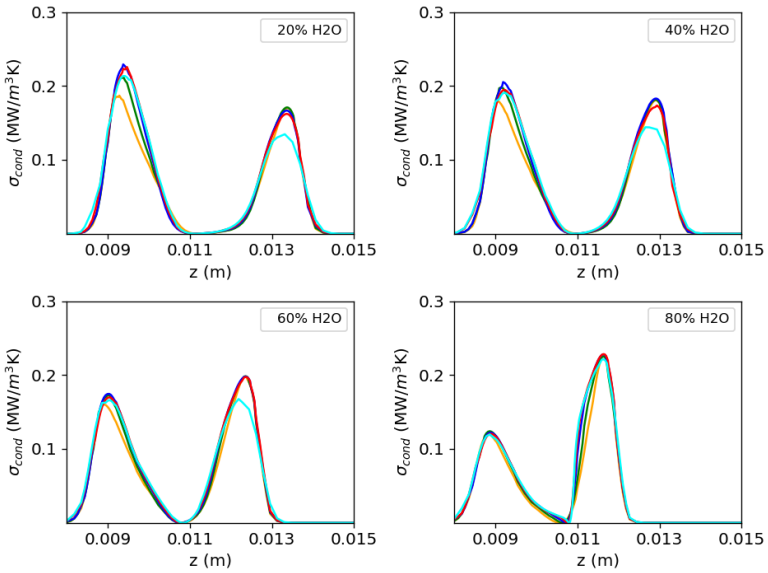

Figure 41: Conduction entropy generation (σ_{cond} $[\frac{MW}{m^3K}]$) distributions along the flame axial position (z [m]) at X_{H_2O} = [0.20, 0.40, 0.60, 0.80] at p = [1, 2, 5, 10, 20] atm. X_{CO} = 0.75, X_{H_2} = 0.25, $\dot{m}_{fuel}$ = 1 $\frac{kg}{m^2s}$, $\dot{m}_{oxidizer}$ = 2 $\frac{kg}{m^2s}$, T_{fuel} = $T_{oxidizer}$=400 K.

In conclusion, the results suggest that pressure has a limited effect on the conduction entropy generation at high levels of H_2O, but is more prominent at lower levels. The suppressive effect of pressure on conduction entropy generation at low levels of H_2O may be attributed to enhanced flame stability and a reduction in flame thickness. At high levels of H_2O, the suppressive effect is diminished, likely due to the increase in the heat capacity of the reactants and products, leading to a reduction in the heat release rate and, consequently, a decrease in entropy generation.

5.3.5 Effect of Varying Mass Fluxes on Chemical Reaction Entropy Generation

The effect of mass fluxes on maximum chemical entropy generation as a function of the molar fraction of water (X_{H_2O}) was investigated. Two sets of cases were considered: one with different mass fluxes of fuel and oxidizer, and the other with equal mass fluxes of both fuel and oxidizer.

In the cases with different mass fluxes (Fig. 43a), it was observed that increasing the mass fluxes of the fuel and oxidizer resulted in larger maximum chemical entropy generation. As the molar fraction of water (X_{H_2O}) increased, the maximum chemical entropy generation initially decreased until reaching a certain level of water in the oxidizer ($X_{H_2O} \approx 0.60$), beyond which it started to increase until flame extinction. This trend was more pronounced for higher mass fluxes, while lower mass fluxes showed a smaller decrease at lower levels of X_{H_2O} (< 0.60). Similarly, at higher levels of X_{H_2O} (< 0.60), higher mass fluxes showed a larger increase, while lower mass fluxes exhibited a smaller increase.

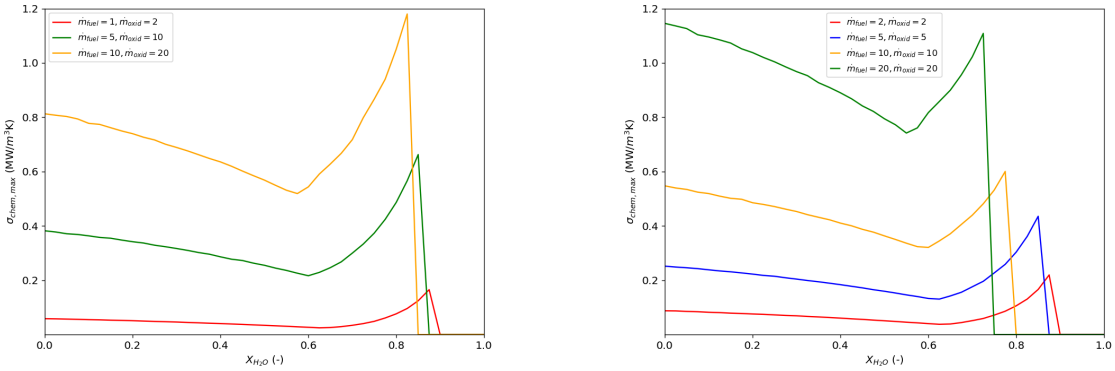

(a) Different mass fluxes ($\dot{m}_f/\dot{m}_o = 1/2$, 5/10, 10/20 kg/(m^{2}s)).

(b) Equal mass fluxes of fuel and oxidizer ($\dot{m}$ = 2, 5, 10, 20 kg/(m^{2}s)).

Figure 42: Maximum chemical entropy generation as a function of H_2O molar fraction (X_{H_2O}) for different inlet mass flux conditions. In (a), the mass fluxes of fuel and oxidizer are different, while in (b), the mass fluxes are equal. p = 1 atm, X_{CO}/X_{H_2} = 75/25, $T_{fuel} = T_{oxid}$ = 400 K.

In the cases with equal mass fluxes (Fig. 43b), increasing the mass fluxes of both fuel and oxidizer resulted in larger maximum chemical entropy generation. Similar to the cases with different mass fluxes, the addition of water to the oxidizer, as indicated by increased X_{H_2O}, initially decreased the chemical contribution at lower levels of X_{H_2O} (< 0.60), followed by an increase at higher levels of water in the oxidizer ($X_{H_2O} > 0.60$) until flame extinction.

The trends observed in the cases with equal mass fluxes appeared to be more consistent compared to the cases with different mass fluxes. This could be attributed to the higher fuel concentration in the flame, as the mass flux of the oxidizer was set to a larger value than that of the fuel in the cases with different mass fluxes.

These findings highlight the significant influence of mass fluxes and the molar fraction of water (X_{H_2O}) on chemical entropy generation. Higher mass fluxes en-

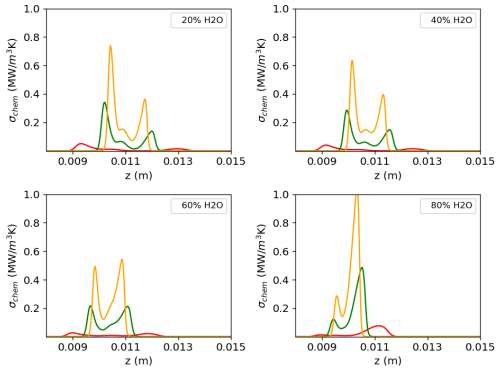

(a) Different mass fluxes ($\dot{m}_f/\dot{m}_o = 1/2$, 5/10, 10/20 kg/(m^{2}s)).

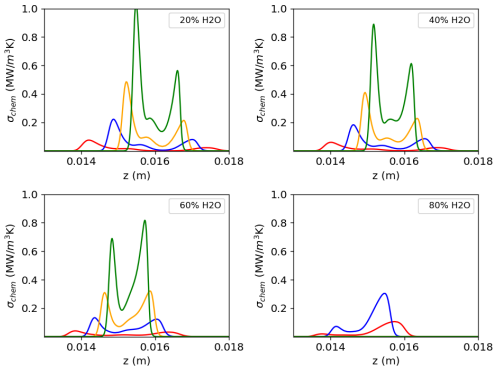

(b) Equal mass fluxes ($\dot{m}$ = 2, 5, 10, 20 kg/(m^{2}s)).

Figure 43: Chemical entropy generation (σ_{chem} [MW/(m^3 K)]) distributions along the flame axial position (z [m]) at X_{H_2O}. In (a), the mass fluxes of fuel and oxidizer are different, while in (b), the mass fluxes are equal. p = 1 atm, $X_{CO}/X_{H_2} = 75/25$, $T_{fuel} = T_{oxid} = 400$ K.

hance chemical activity and lead to larger entropy generation, particularly at higher levels of water in the oxidizer. These insights are valuable for optimizing combustion processes and improving energy conversion systems.

5.3.6 Effect of Varying Presure on Chemical Reaction Entropy Generation

The effect of pressure on chemical entropy generation was investigated by examining the maximum chemical entropy generation ($\sigma_{\text{chem, max}}$) as a function of the molar fraction of water ($X_{\text{H}_2\text{O}}$) at different pressures. The composition of the mixture was fixed with $X_{\text{CO}} = 0.75$ and $X_{\text{H}_2} = 0.25$, while the inlet mass fluxes of the fuel and oxidizer were set to 1 kg/m^{2}s and 2 kg/m^{2}s, respectively. The temperature of both the fuel and oxidizer was maintained at 400 K.

Fig. 44 illustrates the variation of $\sigma_{\text{chem, max}}$ with $X_{\text{H}_2\text{O}}$ for different pressures of 1 atm, 2 atm, 5 atm, 10 atm, and 20 atm. The results demonstrate that increasing the pressure leads to higher chemical entropy generation, particularly at higher levels of molar H_2O. This indicates that the presence of water (H_2O) in the oxidizer has a significant influence on the chemical entropy generation process. At higher

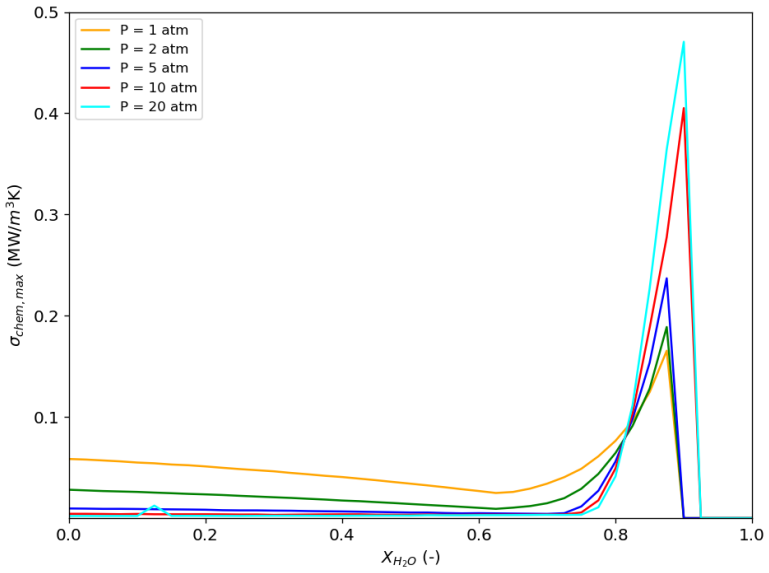

Figure 44: The maximum chemical entropy generation ($\sigma_{chem,max}$ $[\frac{MW}{m^3K}]$) as a function of molar H_2O fraction (X_{H_2O}) at p = [1, 2, 5, 10, 20] atm. X_{CO} = 0.75, X_{H_2} = 0.25, $\dot{m}_{fuel} = 1\ \frac{kg}{m^2 s}$, $\dot{m}_{oxidizer} = 2\ \frac{kg}{m^2 s}$, $T_{fuel} = T_{oxidizer}$=400 K.

pressures, the increased collision frequency between molecules promotes more reactions and enhances the overall chemical activity within the system. Consequently, a higher molar fraction of water (H_2O) in the oxidizer leads to a more pronounced effect on the chemical entropy generation.

It is important to note that the observed increase in chemical entropy generation at higher pressures is limited to a certain range of $X_{\text{H}_2\text{O}}$ values. Beyond a critical molar fraction of water (approximately $X_{\text{H}_2\text{O}} \approx 0.80$), further increase in $X_{\text{H}_2\text{O}}$ results in a decline in chemical entropy generation until flame extinction.

The results highlight the significant role of pressure and molar fraction of water (H_2O) in influencing chemical entropy generation. The findings indicate that higher pressures lead to increased chemical activity and subsequent higher entropy generation, particularly at higher levels of water in the oxidizer.

The increase in chemical entropy generation with pressure can be attributed to the enhanced collision frequency and higher chemical activity at elevated pressures. This leads to a more vigorous reaction environment and increased entropy production.

However, it is important to note that the effect of pressure on chemical entropy generation is limited within a certain range of $X_{\mathrm{H_2O}}$ values. Beyond the critical molar fraction of water, the decline in entropy generation can be attributed to the unfavorable conditions for sustained combustion and the onset of flame extinction.

Understanding these effects is crucial for optimizing combustion processes and improving energy conversion systems. The results provide valuable insights into the interplay between pressure, molar fraction of water, and chemical entropy generation, aiding in the development of efficient and sustainable combustion technologies. The results highlight the significant role of pressure and molar fraction of

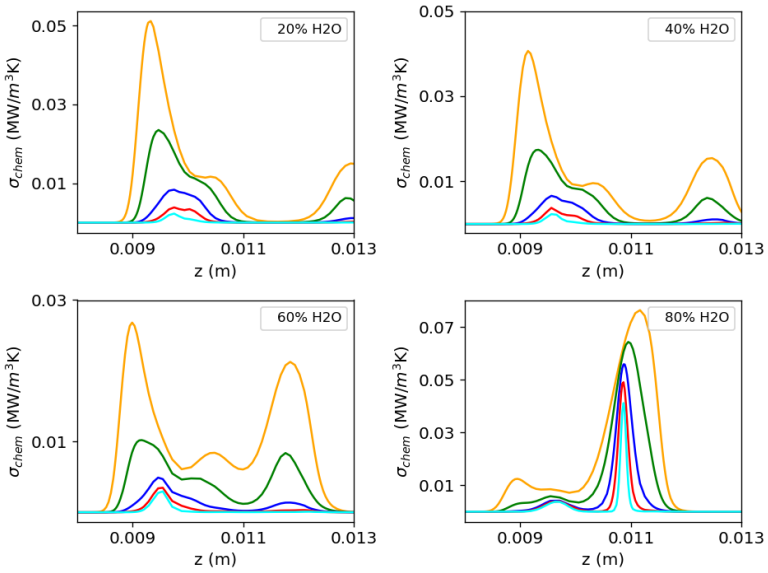

Figure 45: Chemical entropy generation (σ_{chem} [$\frac{MW}{m^3K}$]) distributions along the flame axial position (z [m]) at X_{H_2O} = [0.20, 0.40, 0.60, 0.80] at p = [1, 2, 5, 10, 20] atm. $X_{CO} = 0.75$, $X_{H_2} = 0.25$, $\dot{m}_{fuel} = 1\ \frac{kg}{m^2 s}$, $\dot{m}_{oxidizer} = 2\ \frac{kg}{m^2 s}$, $T_{fuel} = T_{oxidizer}$=400 K.

water (H_2O) in influencing chemical entropy generation. The findings indicate that higher pressures lead to increased chemical activity and subsequent higher entropy generation, particularly at higher levels of water in the oxidizer.

The increase in chemical entropy generation with pressure can be attributed to the enhanced collision frequency and higher chemical activity at elevated pressures. This leads to a more vigorous reaction environment and increased entropy production.

However, it is important to note that the effect of pressure on chemical entropy generation is limited within a certain range of $X_{\mathrm{H_2O}}$ values. Beyond the critical molar fraction of water, the decline in entropy generation can be attributed to the unfavorable conditions for sustained combustion and the onset of flame extinction.

Understanding these effects is crucial for optimizing combustion processes and improving energy conversion systems. The results provide valuable insights into the

interplay between pressure, molar fraction of water, and chemical entropy generation, aiding in the development of efficient and sustainable combustion technologies.

6 Conclusion

6.1 Temperature

In conclusion, the investigation on the effects of temperature and water addition on the combustion process yielded several important findings. The results demonstrated that higher inlet temperatures are flammable for higher concentrations of water. The presence of a three-body reaction mechanism was crucial to sustain the combustion process in the presence of water, as evidenced by the extinction observed at lower molar fractions of water when the mechanism lacked the three-body reaction. However, no significant differences were observed among the mechanisms at higher inlet temperatures.

The study also highlighted the contribution of different reactions to heat production, with three-body reactions playing a significant role. The variation in inlet temperatures had relatively insignificant effects, mainly causing a shift in the flame profile. Additionally, the study investigated conductive heat transfer within the flame and found that the maximum conductive entropy generation increased with increasing water content and was higher at lower temperatures due to increased thermal gradients and conductive heat transfer rates.

Furthermore, the distribution of conduction entropy generation along the flame length was primarily influenced by water content in the oxidizer rather than the inlet temperature. The increased heat transfer from the oxidizer to the fuel, facilitated by higher water content, resulted in a shift in entropy generation. The changes in flame structure and maximum flame temperature were relatively small with increasing water content, suggesting that other factors such as fuel composition, mass flux, and pressure may have a larger impact on overall flame behavior.

The study also investigated the interaction between water content, inlet temperature, and chemical entropy generation. It was found that lower temperatures initially led to higher chemical entropy generation, but the addition of water to the oxidizer decreased the maximum chemical entropy generation. Higher temperatures promoted more intense reactions and subsequently higher chemical entropy generation. Interestingly, the case with an inlet temperature of 600 K exhibited the highest peak of maximum chemical entropy generation, surpassing even the case with the highest inlet temperature of 800 K. This discrepancy can be attributed to the energy provided by higher temperatures, facilitating more complete combustion and less chemical entropy generation.

Overall, the findings emphasize the importance of considering three-body reactions and water content in understanding combustion processes. The study provides insights into the distribution of entropy generation within the flame and the impacts of temperature and water content on different entropy generation processes. Further research is needed to explore the interaction of water content with other flame parameters and to gain a comprehensive understanding of flame behavior.

6.2 Fuel Composition

To conclude, the effects of water on combustion processes were investigated, with a focus on flammability limits, conduction entropy generation, chemical en-

tropy generation, mass diffusion entropy generation, and total entropy generation. The results revealed important insights regarding the impact of water and fuel composition on these entropy generation processes.

Regarding flammability limits, it was found that the variations in fuel composition had a smaller impact compared to temperature. The maximum flame temperature showed small differences with increasing water content until extinction occurred at specific molar fractions of water for different fuel compositions.

The fuel composition was found to significantly influence the maximum conduction entropy generation. Fuels with lower molar carbon monoxide (CO) and higher molar hydrogen (H_2O) exhibited higher conduction entropy generation. As the levels of water increased, the maximum conduction entropy generation also increased, with the largest increase observed for fuels with higher molar hydrogen content.

The distribution of entropy generation along the flame length showed that as more water was added, the peak on the oxidizer side increased while the peak on the fuel side decreased. This effect was more pronounced for fuels with higher levels of molar hydrogen, indicating the cooling effect of water on flames.

In terms of chemical entropy generation, increasing the molar fraction of water led to a decrease in the maximum chemical entropy generation. The fuel composition played a role in this reduction, with the CO/H_2 molar ratio of 25/75 exhibiting the highest chemical entropy generation.

Mass diffusion entropy generation was influenced by both fuel composition and water content. Higher fuel compositions of hydrogen promoted mass diffusion and enhanced chemical reactions within the flame, especially at higher temperatures. The addition of water slightly decreased mass diffusion entropy generation at low concentrations, and a significant drop occurred at a molar fraction of water of 0.90 for a specific fuel composition.

The total entropy generation, which includes contributions from conduction, chemical reactions, mass diffusion, and viscous forces, was dominated by conduction. However, chemical reactions became more significant at higher molar fractions of water.

Overall, the findings demonstrate the complex interactions between water content, fuel composition, and entropy generation processes in combustion. The results provide valuable insights for optimizing combustion systems by considering factors such as fuel composition and water content to improve efficiency and performance. Further research in this field will contribute to a better understanding of combustion processes and guide the development of more efficient and sustainable energy systems.

Appendix A

Dervied Equations

The supplementary attachments in Appendix A are in accordance to Kee et al., [80] Chapter 16. Derived for Eq. (53). Starting with $\frac{dm_k}{dt} h_{fg} = \frac{dQ}{dt}$, we can rearrange it as follows:

$$\frac{dm_k}{dt} = \frac{dQ}{dt} \cdot \frac{1}{h_{fg}}$$

Now, let's express $\frac{dQ}{dt}$ in terms of the mass transfer rate $\frac{dm_k}{dt}$ using an integral:

$$\frac{dm_k}{dt} = \int \frac{dQ}{dt} \cdot \frac{1}{h_{fg}} \, dt$$

This integral represents the accumulation of mass m_k over time. It indicates that the rate of change of mass with respect to time is equal to the integral of the rate of heat transfer $\frac{dQ}{dt}$ divided by the heat of vaporization h_{fg} over the specified time period.

Please note that this derivation assumes a constant heat of vaporization h_{fg} and a single-phase system.

$$\frac{dm_k}{dt} h_{fg} = \frac{dQ}{dt}$$

$$dm_k = \frac{dQ}{h_{fg}}$$

To show how the term with h_{fg} can be used, let's consider the equation:

$$\frac{dm_k}{dt} = \dot{\omega}_k W_k V$$

where $\frac{dm_k}{dt}$ represents the rate of change of mass of species k with respect to time in kilograms per second (kg/s), $\dot{\omega}_k$ is the molar production rate of species k by chemical reaction in moles per cubic meter per second (mol/m^3/s), W_k is the molecular weight of species k in kilograms per mole (kg/mol), and V is the volume of the system in cubic meters (m^3).

Now, let's substitute the equation for $\frac{dm_k}{dt}$ into the original equation:

$$\frac{dQ}{h_{fg}} = (\dot{\omega}_k W_k V)$$

Simplifying further, we define a source term for the heat of vaporization in a closed system.

$$\dot{Q} = \dot{\omega}_k (W_k V \, h_{fg})$$

Thus, we have established how Eq. (52) $\frac{dm_k}{dt} h_{fg} = \frac{dQ}{dt}$ can be incorporated into Eq. (53) $\frac{dm_k}{dt} = \dot{\omega}_k W_k V$.

Derived for Eq. (54)

Starting with the species conservation equation. Recall the mass of species m_k is an **extensive variable** (*depended on the size or extent of the system*) and that the **intensive variable** (*not depended on the size or extent of the system.*) is the mass fraction Y_k.

$$\left(\frac{dm_k}{dt}\right)_{system} = \int_{CV} \dot{\omega}_k W_k \, dV$$

Applying the Reynolds transport theorem, defined in Kee et al., [80] book:

$$\int_{CV} \frac{\partial}{\partial t}(\rho Y_k) \, dV + \int_{CS} \rho Y_k \mathbf{V} \, \mathbf{n} dA = \int_{CV} \dot{\omega}_k W_k \, dV$$

Assuming a fixed volume within which everything is uniform (perfectly mixed), the volume integrals are evaluated quickly, where the right side volume V, is the reactor volume:

$$\int \frac{\partial(\rho Y_k)}{\partial t} \, dV = \int \dot{\omega}_k W_k \, V$$

The integral represents the convective transport through the control surface:

$$\frac{\partial(\rho Y_k)}{\partial t} \, V + \dot{m}(Y_k - Y_k^*) = \dot{\omega}_k W_k \, dV$$

Where V is the volume of the reactor. The integral representing the convective transport through the control surface is evaluated simply by considering the inlet and outlet flow.

Following, inflow velocity is recognized as the opposite direction of $\mathbf{n}$ and opposite for the exit velocity, and the overall mass continuity is set to zero, thus the final form appears as:

$$\frac{dY_k}{dt} = \frac{\dot{m}}{\rho V}(Y_k^* - Y_k) + \frac{\dot{\omega}_k W_k}{\rho}$$

Consider next the energy equation, neglecting kinetic and gravitational-potential energy. Here the extensive variable is the internal energy of the gas E and the intensive variable is the specific internal energy e. The first law of thermodynamics provides the system energy balance:

$$\left(\frac{dE}{dt}\right)_{system} = \dot{Q} - \dot{W}$$

Turning again to the Reynolds transport theorem, relating the flowing system to the control volume yields:

$$\int_{CV} \frac{\partial}{\partial t}(\rho e) \, dV + \int_{CS} \rho e \mathbf{V} \cdot \mathbf{n} d\mathbf{A} = \dot{Q} \, - \int_{CS} p \mathbf{V} \cdot \mathbf{n} d\mathbf{A}$$

The $\dot{Q}$ term represents heat transfer crossing the control surface, with a positive $\dot{Q}$ meaning heat added to the reactor. The second term on the right-hand side is

the flow-work term, which acts at the reactor inlet and exhaust areas. Recall that positive pressure is, by definition, compressive (i.e., directed inward to the control volume). Also, a positive rate-of-work term indicates that work is being done on the system. These considerations set the sign of the flow-work term. For example, at the inlet, where $\mathbf{V} \cdot \mathbf{n} < 0$, work is being done on the system. Thus the leading minus sign is needed to deliver a positive work term.

The two control-surface integrals can be combined to introduce the enthalpy through its definition $h = e + p/\rho$:

$$\int_{CV} \frac{\partial}{\partial t}(\rho e)\, dV + \int_{CS} h\rho \mathbf{V} \cdot \mathbf{n} dA = \dot{Q}$$

Following the procedure used to simplify the species-continuity equation, the energy equation emerges as:

$$\frac{de}{dt} = \frac{dh}{dt} - \frac{d(p/\rho)}{dt} = \frac{\dot{m}}{\rho V}(h^* - h) + \frac{\dot{Q}}{\rho V}$$

The enthalpy has also been introduced on the left-hand side, but for a constant-flow-rate, constant-pressure process, $\frac{d(p/\rho)}{dt} = 0$. The next step in the derivation is to replace enthalpy with temperature as the dependent variable. This replacement is usually convenient since the reaction chemistry depends directly on temperature. For a perfect gas:

$$h = \sum_{k=1}^{K} cY_k h_k \quad \text{and} \quad c_p = \sum_{k=1}^{K} cY_k c_{p,k}$$

The enthalpy derivative can be expanded as:

$$\frac{dh}{dt} = c_p \frac{dT}{dt} + \sum_{k=1}^{K} h_k \frac{dY_k}{dt} = c_p \frac{dT}{dt} + \sum_{k=1}^{K} h_k \left(\frac{\dot{m}}{\rho V}(Y_k^* - Y_k) + \frac{\dot{\omega}_k W_k}{\rho} \right)$$

With some substitutions, the final form appears as:

$$c_p \frac{dT}{dt} = \frac{m}{\rho V} \sum_{k=1}^{K} Y_k^*(h_k^* - h_k) - \sum_{k=1}^{K} \frac{h_k \dot{\omega}_k W_k}{\rho} + \frac{\dot{Q}}{\rho V}$$

Specify a residence time rather than the flow rate may be desirable, which the nominal residence time is given by:

$$\tau = \frac{\rho V}{\dot{m}}$$

Appendix B

Fuel composition X_{fuel} corresponding to $X_{H_2} = X_{CO} = 0.50$

Supplementary data for the Sun et al., [39] Mechanism

	Reaction	Integrated Value
R13	$H_2O + H_2O \rightleftharpoons H + OH + H_2O$	279630
R15	$H + O_2(+H_2O) \rightleftharpoons HO_2(+H_2O)$	147786
R3	$H_2 + OH \rightleftharpoons H + H_2O$	139137
R19	$HO_2 + OH \rightleftharpoons H_2O + O_2$	117517
R30	$CO + OH \rightleftharpoons CO_2 + H$	90141.9
R18	$HO_2 + O \rightleftharpoons O_2 + OH$	60326.4
R11	$H + O + M \rightleftharpoons OH + M$	62145.8

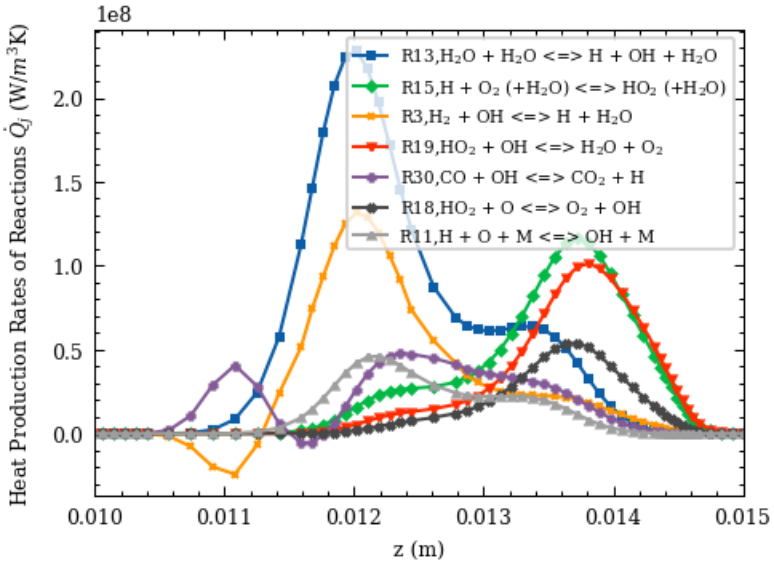

Figure 46: Heat Production Rates for Key Reactions in the System. Based on their integrated values, the plot showcases the heat production rates for the seven most significant reactions, identified as R13, R15, R3, R19, R30, R18, and R11. These reactions play a crucial role in the overall heat release, highlighting their substantial contributions to the heat generation process in the system. The oxidizer level and fuel composition are as previously mentioned.

Appendix C

Supplementary data for the Sun et al., [39] Mechanism compared to Gri-Mech 3.0

Heat production rate of the five reactions that has the largest contributors for Gri-Mech Mechanism and Sun Mechanism at Inlet Temperatures of 400 K, 600 K, and 800 K at molar fractions of water equal to: 0.20, 0.40, 0.60 and 0.80.

Appendix D

Temperature and Species Molar Composition for the General Characterized flame by Wang et al. [38]

H_2

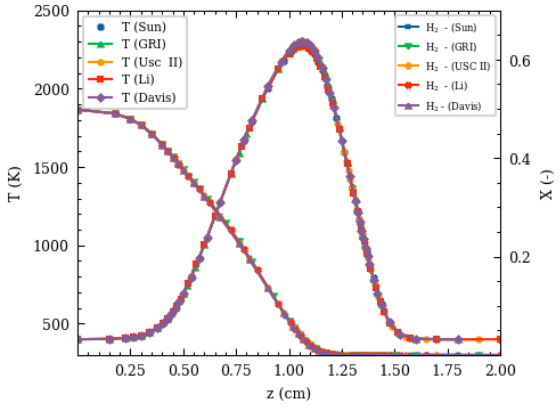

Figure 48: Temperature (T [K]) along the axial flame position (z [cm]) for X_{H_2} compared with mechanisms et al. [39, 40, 41, 43, 45].

CO

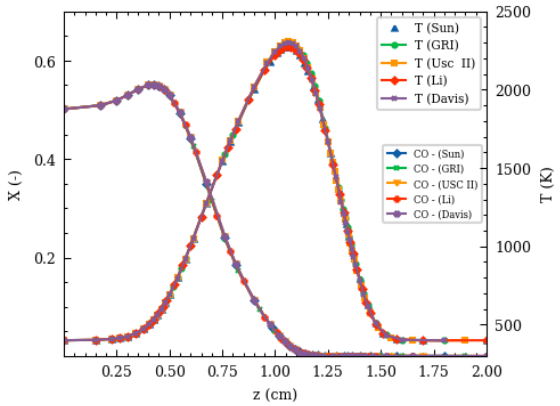

Figure 49: Temperature (T [K]) along the axial flame position (z [cm]) for X_{CO} compared with mechanisms et al. [39, 40, 41, 43, 45].

O_2

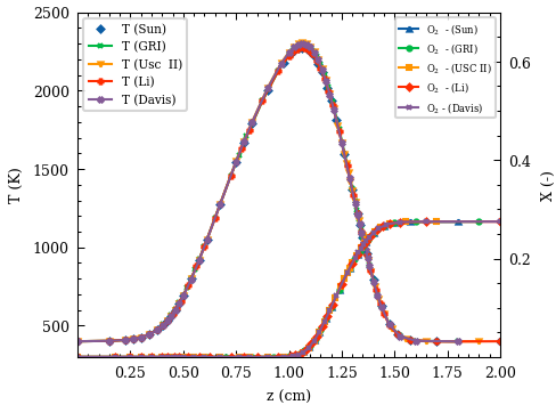

Figure 50: Temperature (T [K]) along the axial flame position (z [cm]) for X_{O_2} compared with mechanisms et al. [39, 40, 41, 43, 45].

H_2O

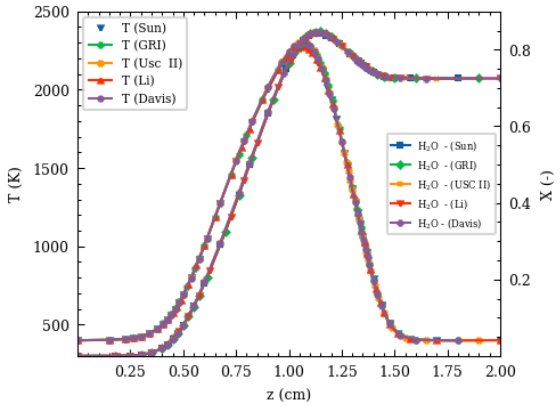

Figure 51: Temperature (T [K]) along the axial flame position (z [cm]) for X_{H_2O} compared with mechanisms et al. [39, 40, 41, 43, 45].

Appendix E

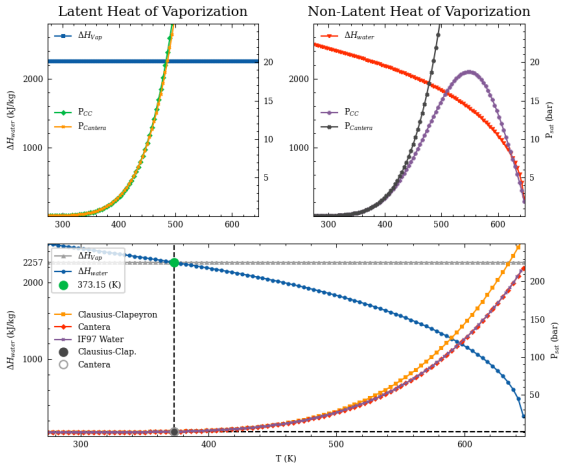
Latent Heat of Vaporization
Non-Latent Heat of Vaporization
Clausius-Clapeyron
Cantera
IF97 Water
Clausius-Clap.
373.15 (K)
T (K)

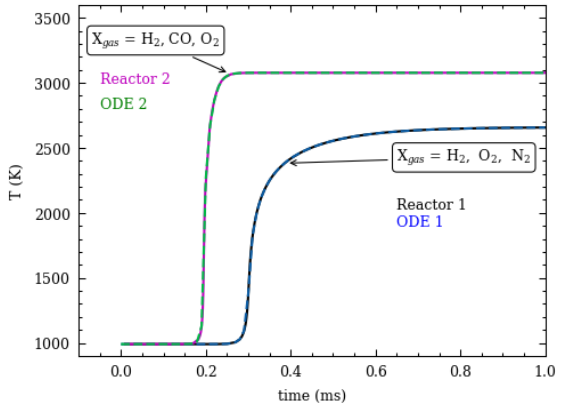
X_gas = H2, CO, O2
Reactor 2
ODE 2
X_gas = H2, O2, N2
Reactor 1
ODE 1
T (K)
time (ms)

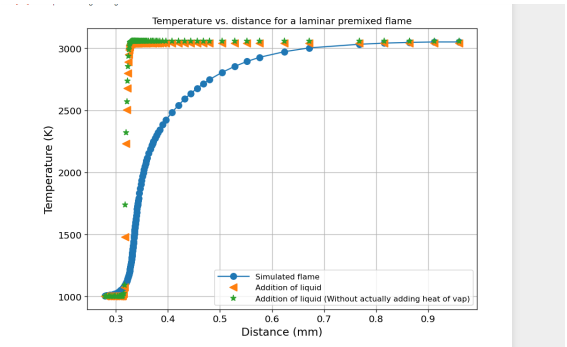
Temperature vs. distance for a laminar premixed flame
Simulated flame
Addition of liquid
Addition of liquid (Without actually adding heat of vap)
Temperature (K)
Distance (mm)

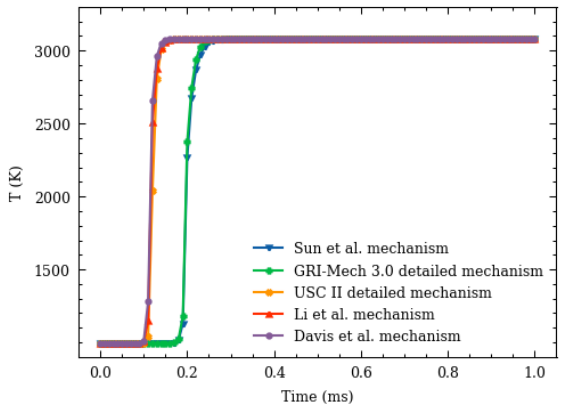
Sun et al. mechanism
GRI-Mech 3.0 detailed mechanism
USC II detailed mechanism
Li et al. mechanism
Davis et al. mechanism
T (K)
Time (ms)

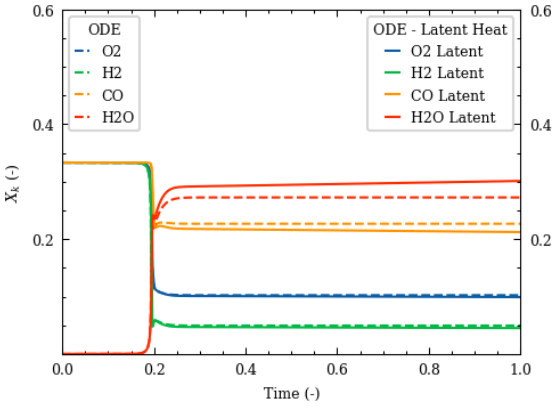
ODE
O2
H2
CO
H2O
ODE - Latent Heat
O2 Latent
H2 Latent
CO Latent
H2O Latent
X_k (-)
Time (-)

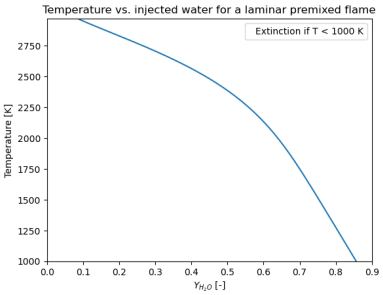
Temperature vs. injected water for a laminar premixed flame
Extinction if T < 1000 K
Temperature [K]
Y_{H_2O} [-]

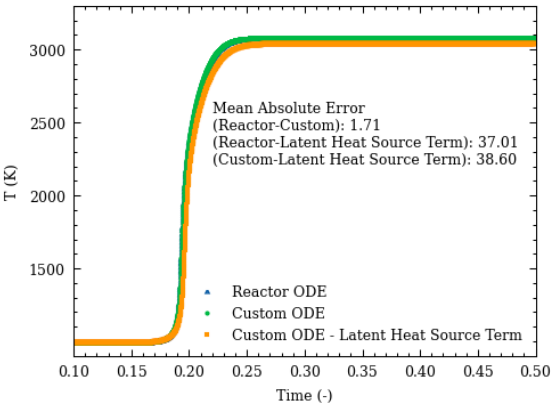
Mean Absolute Error
(Reactor-Custom): 1.71
(Reactor-Latent Heat Source Term): 37.01
(Custom-Latent Heat Source Term): 38.60
Reactor ODE
Custom ODE
Custom ODE - Latent Heat Source Term
T (K)
Time (-)

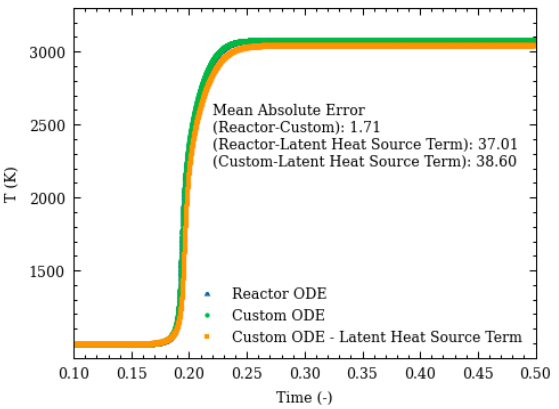
Mean Absolute Error
(Reactor-Custom): 1.71
(Reactor-Latent Heat Source Term): 37.01
(Custom-Latent Heat Source Term): 38.60
Reactor ODE
Custom ODE
Custom ODE - Latent Heat Source Term
T (K)
Time (-)

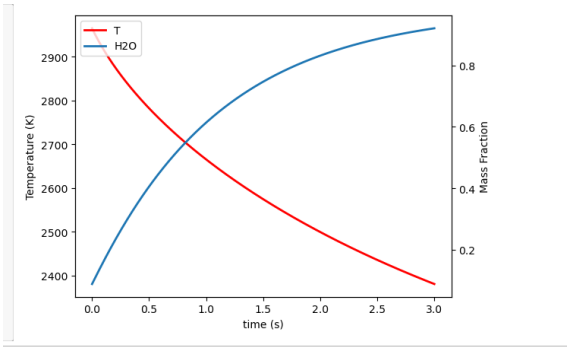
T
H2O
Temperature (K)
Mass Fraction
time (s)
2400
2500
2600
2700
2800
2900
0.2
0.4
0.6
0.8
0.0
0.5
1.0
1.5
2.0
2.5
3.0

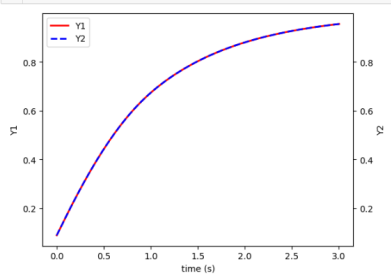
Y1
Y2
time (s)
0.2
0.4
0.6
0.8
0.0
0.5
1.0
1.5
2.0
2.5
3.0

References

[1] W. Ripple et al., "World Scientists' Warning to Humanity: A Second Notice," BioScience, vol. 67, no. 12, pp. 1026-1028, 2017, doi: 10.1093/biosci/bix125.

[2] "Fossil Fuels," Our World in Data. [Online]. Available: https://ourworldindata.org/fossil-fuels. Accessed: Jun. 10, 2023.

[3] Energy Institute, KPMG, Kearney, "Statistical Review of World Energy," [Online]. Available: https://www.bp.com/en/global/corporate/energy-economics/statistical-review-of-world-energy.html. Accessed on: May 16, 2023.

[4] "Fossil Fuels - Description," Energy and Environmental Study Institute (EESI). [Online]. Available: https://www.eesi.org/topics/fossil-fuels/description. Accessed: Jun. 10, 2023.

[5] Energy and Environmental Study Institute (EESI). [Online]. Available: https://www.eesi.org/topics/fossil-fuels. Accessed: Jun. 10, 2023.

[6] W. Ripple et al., "World Scientists' Warning of a Climate Emergency 2022," BioScience, vol. 72, no. 12, pp. 1149-1155, 2022, doi: 10.1093/biosci/biac083.

[7] SINTEF. "GrateCFD - SINTEF." [Online]. Available: https://www.sintef.no/project/gratecfd/a4pdf. Accessed: Feb. 13, 2023.

[8] A. Emadi and M. D. Emami, "Analysis of Entropy Generation in a Hydrogen-Enriched Turbulent Non-Premixed Flame," International Journal of Hydrogen Energy, vol. 38, no. 14, pp. 5961-5973, 2013. doi: 10.1016/j.ijhydene.2013.02.115.

[9] D. Moon, S. Kim, Y. Park, J. Lee, and J. Kim, "H2 Pressure Swing Adsorption for High Pressure Syngas from an Integrated Gasification Combined Cycle with a Carbon Capture Process," Applied Energy, vol. 183, pp. 760-774, 2016.

[10] A. P. Wandel and R. P. Lindstedt, "A mixture-fraction-based hybrid binomial Langevin-multiple mapping conditioning model," Proceedings of the Combustion Institute, vol. 37, no. 2, pp. 2151-2158, 2019.

[11] J. O'Brien, C. A. Towery, P. E. Hamlington, M. Ihme, A. Y. Poludnenko, and J. Urzay, "The cross-scale physical-space transfer of kinetic energy in turbulent premixed flames," Proceedings of the Combustion Institute, vol. 36, no. 2, pp. 1967-1975, 2017.

[12] J. Sosa, J. Chambers, K. A. Ahmed, A. Poludnenko, and V. N. Gamezo, "Compressible turbulent flame speeds of highly turbulent standing flames," Proceedings of the Combustion Institute, vol. 37, no. 3, pp. 3495-3502, 2019.

[13] K. Safer, A. Ouadha, and F. Tabet, "Entropy generation in turbulent syngas counter-flow diffusion flames," International Journal of Hydrogen Energy, vol. 42, no. 49, pp. 29532-29544, 2017.

[14] A. Y. Cooney and S. L. Singer, "A hybrid droplet vaporization-chemical surrogate approach for emulating vaporization, physical properties, and chemical combustion behavior of multicomponent fuels," Proceedings of the Combustion Institute, vol. 37, no. 3, pp. 3229-3236, 2019.

[15] P. S. Salimath, I. S. Ertesvåg, "Local entropy generation and entropy fluxes of a transient flame during head-on quenching towards solid and hydrogen-permeable porous walls," Int. J. Hydrogen Energy, vol. 46, no. 52, pp. 26616-26630, 2021. doi: 10.1016/j.ijhydene.2021.05.142.

[16] A. Datta, "Entropy generation in a confined laminar diffusion flame," Combust. Sci. Tech., vol. 159, pp. 39-56, 2000. doi: 10.1080/00102200008935776.

[17] A. Datta, "Effects of gravity on structure and entropy generation of confined laminar diffusion flames," Int J Therm Sci, vol. 44, pp. 429-440, 2005. doi: 10.1016/j.ijthermalsci.2004.10.003.

[18] D. Stanciu, D. Isvoranu, M. Marinescu, Y. Gogus, "Second law analysis of diffusion flames," Int. J. Thermodyn., vol. 4, no. 1, pp. 1-18, 2001. [Online]. Available: dergi-park.org.tr/en/pub/ijot/issue/5742/76599.

[19] K. Nishida, T. Takagi, S. Kinoshita, "Analysis of entropy generation and energy loss during combustion," Proc. Combust. Inst., vol. 29, no. 1, pp. 869-874, 2002. doi: 10.1016/S1540-7489(02)80111-0.

[20] S. Chen, Z. Liu, J. Liu, J. Li, L. Wang, C. Zheng, "Analysis of entropy generation in hydrogen-enriched ultra-lean counter-flow methane air non-premixed combustion," Int. J. Hydrogen Energy, vol. 35, no. 22, pp. 12491-12501, 2010. doi: 10.1016/j.ijhydene.2010.08.048.

[21] S. Chen, H. Han, Z. Liu, J. Li, C. Zheng, "Analysis of entropy generation in non-premixed hydrogen versus heated air counter-flow combustion," Int. J. Hydrogen Energy, vol. 35, pp. 4736-4746, 2010. doi: 10.1016/j.ijhydene.2010.02.113.

[22] V. Raghavan, G. Gogos, V. Babu, T. Sundararajan, "Entropy generation during the quasi-steady burning of spherical fuel particles," Int. J. Therm. Sci., vol. 46, pp. 589-604, 2007. doi: 10.1016/j.ijthermalsci.2006.07.006.

[23] D. N. Pope, V. Raghavan, G. Gogos, "Gas-phase entropy generation during transient methanol droplet combustion," Int. J. Therm. Sci., vol. 49, pp. 1288-1302, 2010. doi: 10.1016/j.ijthermalsci.2010.02.012.

[24] Z. Zhang, C. Lou, Y. Long, B. M. Kumfer, "Thermodynamics second-law analysis of hydrocarbon diffusion flames: Effects of soot and temperature," Combust. Flame, vol. 234, p. 111618, 2021. doi: 10.1016/j.combustflame.2021.111618.

[25] H. Yan, G. Tang, C. Wang, L. Li, Y. Zhou, Z. Zhang, C. Lou, "Thermodynamics irreversibilities analysis of oxy-fuel diffusion flames: The effect of oxygen concentration," Entropy, vol. 24, no. 2, doi: 10.3390/e24020205.

[26] M. Kooshkbaghi, C. E. Frouzakis, K. Boulouchos, I. V. Karlin, "Entropy production analysis for mechanism reduction," Combust. Flame, vol. 161, no. 6, pp. 1507-1515, 2014. doi: 10.1016/j.combustflame.2013.12.016.

[27] S. Pooras, Bykov V, Gol'dshtein V, Maas U. "Joint characteristic timescales and entropy production analyses for model reduction of combustion systems," Entropy, vol. 19, no. 6, p. 264, 2017. doi: 10.3390/e19060264.

[28] A. E. Ream, J. C. Slattery, P. G. Cizmas, "A method for generating reduced-order combustion mechanisms that satisfy the differential entropy inequality," Phys Fluids B, vol. 30, no. 4, p. 043601, 2018. doi: 10.1063/1.5022691.

[29] F. Bazdidi-Tehrani, Abedinejad MS, Mohammadi M. "Analysis of relationship between entropy generation and soot formation in turbulent kerosene/air jet diffusion flames," Energy Fuels, vol. 33, no. 9, pp. 9184-9195, 2019. doi: 10.1021/acs.energyfuels.9b01671.

[30] Y. Ju, R. T. Liu, and Y. Liu, "Effects of radiative emission and absorption on the propagation and extinction of premixed gas flames," in Symposium (International) on Combustion, vol. 27, no. 2, pp. 2619-2626, 1998. [Online]. Available: https://doi.org/10.1016/S0082-0784(98)80116-1.

[31] F. Liu, Y. Ju, and Y. Liu, "The chemical effect of CO2 replacement of N2 in air on the burning velocity of CH4 and H2 premixed flames," Combustion and Flame, vol. 133, no. 4, pp. 495-497, 2003. [Online]. Available: https://doi.org/10.1016/S0010-2180(03)00019-1.

[32] S. Sun, C. He, J. Zhou, and Z. Huang, "Experimental and theoretical studies of laminar flame speed of CO/H2 in O2/H2O atmosphere," International Journal of Hydrogen Energy, vol. 41, no. 4, pp. 3272-3283, 2016. [Online]. Available: https://doi.org/10.1016/j.ijhydene.2015.11.120.

[33] C.S. Yoo, S.D. Lee, and S.H. Chung, "Extinction of Strained Premixed Flames of Hydrogen/Air/Steam Mixture: Local Equilibrium Temperature and Local Equivalence Ratio," Combustion Science and Technology, vol. 155, no. 1, pp. 227-242, 2000. doi: 10.1080/00102200008947291.

[34] R. Seiser and K. Seshadri, "The Influence of Water on Extinction and Ignition of Hydrogen and Methane Flames," Proceedings of the Combustion Institute, vol. 30, no. 1, pp. 407-414, 2005. doi: 10.1016/j.proci.2004.08.220.

[35] K. Yang and H. Shih, "NO formation of opposed-jet syngas diffusion flames: Strain rate and dilution effects," International Journal of Hydrogen Energy, vol. 42, no. 38, pp. 24517-24531, 2017. [Online]. Available: https://doi.org/10.1016/j.ijhydene.2017.07.137.

[36] D. Giles, J. H. Chen, and M. J. Chen, "NOx emission characteristics of counterflow syngas diffusion flames with airstream dilution," Fuel, vol. 85, no. 12-13, pp. 1729-1742, 2006. [Online]. Available: https://doi.org/10.1016/j.fuel.2006.01.027.

[37] S. Som, A. I. Ramírez, J. Hagerdorn, A. Saveliev, and S. K. Aggarwal, "A numerical and experimental study of counterflow syngas flames at different pressures," Fuel, vol. 87, no. 3, pp. 319-334, 2008.

[38] P. Wang, T. Guo, H. Xu, Y. Zhao, S. Meng, D. Feng, and S. Sun, "Study on the effect of H2O on the formation of CO in the counterflow diffusion flame of H2/CO syngas in O2/H2O," Fuel, vol. 234, pp. 516-525, 2018.

[39] S. Sun, S. Meng, Y. Zhao, H. Xu, Y. Guo, and Y. Qin, "Experimental and theoretical studies of laminar flame speed of CO/H2 in O2/H2O atmosphere," International Journal of Hydrogen Energy, vol. 41, no. 4, pp. 3272-3283, 2016.

[40] S. G. Davis, A. V. Joshi, H. Wang, and F. Egolfopoulos, "An optimized kinetic model of H2/CO combustion," Proceedings of the Combustion Institute, vol. 30, no. 1, pp. 1283-1292, 2005.

[41] H. Wang, X. You, A. V. Joshi, S. G. Davis, A. Laskin, F. Egolfopoulos, and C. K. Law, "USC Mech Version II. High-Temperature Combustion Reaction Model of H2/CO/C1-C4 Compounds," May 2007. [Online]. Available: `http://ignis.usc.edu/USC.Mech.II.htm`.

[42] A. Kéromnès, W. K. Metcalfe, K. A. Heufer, N. Donohoe, A. K. Das, C. Sung, J. Herzler, C. Naumann, P. Griebel, O. Mathieu, M. C. Krejci, E. L. Petersen, W. J. Pitz, and H. J. Curran, "An experimental and detailed chemical kinetic modeling study of hydrogen and syngas mixture oxidation at elevated pressures," Combustion and Flame, vol. 160, no. 6, pp. 995-1011, 2013.

[43] J. Li, Z. Zhao, A. Kazakov, M. Chaos, F. L. Dryer, and J. J. Scire, "A comprehensive kinetic mechanism for CO, CH2O, and CH3OH combustion," International Journal of Chemical Kinetics, vol. 39, no. 3, pp. 109-136, 2007.

[44] H. Xu, F. Liu, S. Sun, Y. Zhao, S. Meng, L. Chen, and L. Chen, "Flame attachment and kinetics studies of laminar coflow CO/H2 diffusion flames burning in O2/H2O," Combustion and Flame, vol. 196, pp. 147-159, 2018.

[45] G. P. Smith, D. M. Golden, M. Frenklach, N. W. Moriarty, B. Eiteneer, M. Goldenberg, C. T. Bowman, R. K. Hanson, S. Song, W. C. Gardiner Jr., V. V. Lissianski, and Z. Qin, "GRI-Mech 3.0 detailed mechanism,". Available: http://combustion.berkeley.edu/gri-mech/.

[46] A. V. Joshi and H. Wang, "Master equation modeling of wide range temperature and pressure dependence of CO + OH → products," International Journal of Chemical Kinetics, vol. 38, no. 1, pp. 57-73, 2006.

[47] X. You, H. Wang, E. Goos, C. J. Sung, and S. J. Klippenstein, "The Journal of Physical Chemistry A 2007 111 (19), 4031-4042," The Journal of Physical Chemistry A, vol. 111, no. 19, pp. 4031-4042, 2007.

[48] J. Li, Z. Zhao, A. Kazakov, and F. L. Dryer, "An updated comprehensive kinetic model of hydrogen combustion," International Journal of Chemical Kinetics, vol. 36, no. 10, pp. 566-575, 2004.

[49] M. A. Mueller, R. A. Yetter, and F. L. Dryer, "Flow reactor studies and kinetic modeling of the H2/O2/NOX and CO/H2O/O2/NOX reactions," International Journal of Chemical Kinetics, vol. 31, no. 10, pp. 705-724, 1999.

[50] N. K. Srinivasan and J. V. Michael, "The thermal decomposition of water," International Journal of Chemical Kinetics, vol. 38, no. 3, pp. 211-219, 2006.

[51] M. P. Burke, M. Chaos, Y. Ju, F. L. Dryer, and S. J. Klippenstein, "Comprehensive H2/O2 kinetic model for high-pressure combustion," International Journal of Chemical Kinetics, vol. 44, no. 7, pp. 444-474, 2012.

[52] C. Luo, B. Moghtaderi, E. M. Kennedy, and B. Z. Dlugogorski, "Three-dimensional numerical study on flames," Chemical Product and Process Modeling, vol. 4, 2009.

[53] P. S. Salimath and I. S. Ertesvåg, "Local entropy generation and entropy fluxes of a transient flame during head-on quenching towards solid and hydrogen-permeable porous walls," International Journal of Hydrogen Energy, vol. 46, no. 52, pp. 26616-26630, 2021.

[54] Patki, Parth, et al. "Entropy Generation Mechanisms from Exothermic Chemical Reactions in Laminar, Premixed Flames." Proceedings of the Combustion Institute, vol. 39, no. 2, 2023, pp. 1607-1614, https://doi.org/10.1016/j.proci.2022.08.069. Accessed 11 Jun. 2023.

[55] R. W. Bates, D. M. Golden, R. K. Hanson, and C. T. Bowman, "Experimental study and modeling of the reaction H + O2 + M = HO2 + M (M = Ar, N2, H2O) at elevated pressures and temperatures between 1050 and 1250 K," Phys Chem Chem Phys, vol. 3, pp. 2337-2342, 2001.

[56] K. Nishida, T. Takagi, and S. Kinoshita, "Analysis of entropy generation and exergy loss during combustion," Proceedings of the Combustion Institute, vol. 29, no. 1, pp. 869-874, 2002.

[57] J. Zhang, D. Han, and Z. Huang, "Second-law thermodynamic analysis for premixed hydrogen flames with diluents of argon/nitrogen/carbon dioxide," International Journal of Hydrogen Energy, vol. 44, no. 10, pp. 5020-5029, 2019.

[58] L. Acampora and F. S. Marra, "Second law thermodynamic analysis of syngas premixed flames," International Journal of Hydrogen Energy, vol. 45, no. 21, pp. 12185-12202, 2020.

[59] A. E. Lutz, R. J. Kee, J. F. Grcar, and F. M. Rupley, "OPPDIF: A Fortran program for computing opposed-flow diffusion flames," United States, 2003. [Online]. Available: https://doi.org/10.2172/568983.

[60] S. J. Lorentzen and I. S. Ertesvåg, "Entropy generation in an opposed-flow laminar non-premixed flame—Effects of using reduced and global chemical mechanisms for methane–air and syngas–air combustion," Fuel, vol. 345, p. 128263, 2023.

[61] A. Bejan, "Entropy generation minimization: the method of thermodynamic optimization of finite-size systems and finite-time processes," CRC press, 1996.

[62] N. Couto, A. Rouboa, V. Silva, E. Monteiro, and K. Bouziane, "Influence of the biomass gasification processes on the final composition of syngas," Energy Procedia, vol. 36, pp. 596-606, 2013.

[63] P. E. DesJardin, "The role of water vapor in combustion processes," Progress in Energy and Combustion Science, vol. 30, pp. 1-32, 2004.

[64] J. Warnatz, U. Maas, and R. W. Dibble, "Combustion: Physical and chemical fundamentals, modeling and simulation, experiments, pollutant formation," Springer-Verlag, 2011.

[65] F. A. Williams and E. H. Stapper, "Chemical kinetics of hydrogen oxidation," Proceedings of the Combustion Institute, vol. 14, pp. 1597-1605, 1973.

[66] K. Yang, M. A. Wahid, M. S. Abdullah, and A. S. M. Abdul Ghani, "Exergy analysis of hydrogen enriched air combustion in a gas turbine combustor," Energy Conversion and Management, vol. 87, pp. 998-1007, 2014.

[67] Y. C. Lee, Y. H. Lai, and C. H. Chang, "Entropy generation and heat transfer analysis of hydrogen combustion in micro-combustors," Energy Conversion and Management, vol. 83, pp. 216-224, 2014.

[68] A. S. Khalil, S. Kumar, and M. Kundu, "Thermodynamic analysis of a gas turbine cycle using water injection," Energy Conversion and Management, vol. 176, pp. 348-355, 2018.

[69] S. L. Miller and J. Bowman, "Impact of water addition on laminar flame speed and Markstein length of lean premixed methane/air flames," Combustion and Flame, vol. 158, no. 7, pp. 1221-1233, 2011.

[70] R. G. Gilbert, K. Luther, and J. Troe, "Ber. Bunsenges. Phys. Chem., 87:169," 1983.

[71] E.S. Pedersen, "Understanding energy conversion in combustion - Detailed analysis of entropy generation (exergy degradation) in flames," Norwegian University of Science and Technology (NTNU), Trondheim, Norway, 2022.

[72] S. Lorentzen and I. Ertesvåg, "Entropy Generation in an Opposed-Flow Laminar Non-Premixed Flame—Effects of Using Reduced and Global Chemical Mechanisms for Methane–Air and Syngas–Air Combustion," in Fuel, vol. 345, p. 128263, 2023. [Online]. Available: https://doi.org/10.1016/j.fuel.2023.128263

[73] H. B. Callen, "Thermodynamics and an Introduction to Thermostatistics," John Wiley Sons, 1985.

[74] M. J. Moran and H. N. Shapiro, "Fundamentals of Engineering Thermodynamics," 5th ed., John Wiley Sons, 2006.

[75] D. V. Schroeder, "An Introduction to Thermal Physics," Addison-Wesley, 2000.

[76] M. J. Moran, H. N. Shapiro, D. D. Boettner, and M. B. Bailey, "Principles of Engineering Thermodynamics," John Wiley Sons, 2010.

[77] Y. A. Cengel and M. A. Boles, "Thermodynamics: An Engineering Approach," 8th ed., McGraw-Hill Education, 2014.

[78] S. Turns and D. C. Haworth, "An Introduction to Combustion: Concepts and Applications," 4th ed., McGraw-Hill.

[79] R. B. Bird, W. E. Stewart, and E. N. Lightfoot, "Transport phenomena," 2nd ed., John Wiley Sons, 2007.

[80] R. J. Kee, M. E. Coltrin, P. Glarborg, and H. Zhu, "Chemically Reacting Flow: Theory and Practice," 2nd ed., John Wiley Sons, 2005.

[81] J. Crank, "The mathematics of diffusion," Oxford University Press, 1975.

[82] F. M. White, "Fluid mechanics," 8th ed., McGraw Hill Education, 2016.

[83] C. K. Law, "Combustion physics," Cambridge University Press, 2006.

[84] D. G. Goodwin, H. K. Moffat, I. Schoegl, R. L. Speth, and B. W. Weber, "Cantera: An Object-oriented Software Toolkit for Chemical Kinetics, Thermodynamics, and Transport Processes (2.6.0)," Zenodo, 2022. https://doi.org/10.5281/zenodo.6387882

[85] J. D. Hunter, "Matplotlib: A 2D graphics environment," Computing in Science Engineering, vol. 9, no. 3, pp. 90–95, 2007. https://doi.org/10.1109/MCSE.2007.55

[86] S. Van Der Walt, S. C. Colbert, and G. Varoquaux, "The NumPy array: A structure for efficient numerical computation," Computing in Science Engineering, vol. 13, no. 2, pp. 22–30, 2011. https://doi.org/10.1109/MCSE.2011.37

[87] M. F. Modest, "Radiative heat transfer," Academic Press, 2013.

[88] D. R. Cullimore and J. M. Beer, "On the gray gas and other radiation models for two-dimensional furnace calculations," Combustion and Flame, vol. 85, no. 1-2, pp. 1-16, 1991.

[89] Y. Zhang and K. Maruta, "Radiation in sooting flames," Progress in Energy and Combustion Science, vol. 39, no. 6, pp. 585-608, 2013.

[90] F. Liu and B. Rogg, "Spectral line-based weighted-sum-of-gray-gases model for radiation heat transfer in nonhomogeneous gas mixtures," Journal of Heat Transfer, vol. 122, no. 2, pp. 363-371, 2000.

[91] P. Saxena and F. A. Williams, "Testing a small detailed chemical-kinetic mechanism for the combustion of hydrogen and carbon monoxide," Combustion and Flame, vol. 145, no. 1-2, pp. 316-323, 2006.

[92] I. H. Bell, J. Wronski, S. Quoilin, and V. Lemort, "Pure and Pseudo-pure Fluid Thermophysical Property Evaluation and the Open-Source Thermophysical Property Library CoolProp," Industrial Engineering Chemistry Research, vol. 53, no. 6, pp. 2498-2508, 2014.